Position Correction in Ptychography and Its Applications

Dwivedi, Priya

DOI
10.4233/uuid:aef89098-da7a-4465-bfaa-31103d47de85

Publication date
2019

Document Version
Final published version

Citation (APA)
Dwivedi, P. (2019). *Position Correction in Ptychography and Its Applications*. [Dissertation (TU Delft), Delft University of Technology]. https://doi.org/10.4233/uuid:aef89098-da7a-4465-bfaa-31103d47de85

Position Correction in Ptychography and Its Applications

Position Correction in Ptychography and Its Applications

Proefschrift

ter verkrijging van de graad van doctor
aan de Technische Universiteit Delft,
op gezag van de Rector Magnificus prof.dr.ir. T.H.J.J. van der Hagen;
voorzitter van het College voor Promoties,
in het openbaar te verdedigen op
Donderdag 11 juli 2019 om 12:30 uur

door

Priya DWIVEDI

Master of Science in Applied Physics,
Indian Institute of Technology (ISM), Dhanbad, India
geboren te Kanpur, India.

This dissertation has been approved by the

promotor: Prof.dr. H.P. Urbach
promotor: Dr.ir. S.F. Pereira

Composition of the doctoral committee:

Rector Magnificus	chairperson
Prof.dr. H.P. Urbach	Delft University of Technology, promotor
Dr.ir. S.F. Pereira	Delft University of Technology, promotor
Independent members:	
Prof.dr. W.M.J.M. Coene	Technische Universiteit Delft and ASML, Netherlands
Prof.dr. J.V.K. Saarinen	University of Eastern Finland, Finland
Prof.dr.ir. A.J. den Boef	Vrije Universiteit Amsterdam and ASML, Netherlands
Prof.dr. J.L. Saez	Universitat Jaume I, Spain
Dr. O. El Gawhary	VSL Dutch Metrology Institute, Netherlands
Prof.dr. S. Stallinga	Technische Universiteit Delft, Netherlands, reserve member

The research leading to these results has received funding from the people Programme (Marie Curie Actions) of the European Union's Seventh Framework Programme (FP7/2007-2013) under REA Grant Agreement no. PITN-GA-2013-608082.

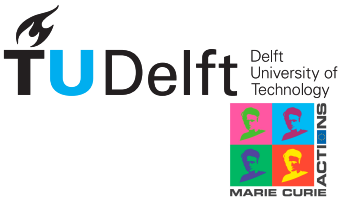

Keywords: Lensless imaging, coherent diffractive imaging, phase retrieval technique, ptychography.

Printed by: Ipskamp Printing.

Front & Back: Abstract representation of lensless imaging that captures the entire content of this thesis in a single illustration.

ISBN 000-00-0000-000-0

An electronic version of this dissertation is available at
http://repository.tudelft.nl/.

To my parents

Contents

Summary

Lenses are indispensable tool to perform imaging and see the small details of an object which was otherwise not possible. The smallest feature of an object that one can see using a lens depends on the numerical aperture (NA) of the lens and the used wavelength of light. For a fixed NA, the shorter the wavelength is, the smaller the features of an object can be seen. Therefore, for high-resolution imaging, short wavelengths such as x-rays and e-beams are used. For these wavelengths, the refractive index of the most of the materials is close to 1. Therefore, rays passing through these lenses do not deviate and get absorbed within the materials eventually. To circumvent this problem, different types of diffractive lenses were introduced. Imaging can be performed using these lenses, however, it cannot achieve diffraction limited resolution. The reason for this is the present aberrations in the imaging systems. To this end, computational imaging methods start to play a major role.

Lensless imaging is a type of computational imaging which replaces a lens by algorithms. Hence, lensless imaging is not limited by the present aberrations of the lens or imaging system. Besides, with this technique not only amplitude but also phase information can be retrieved. Phase information is important especially for low contrast objects. Since these algorithms solve the phase of the object iteratively, they are also called as phase retrieval techniques.

In the past, several phase retrieval techniques were proposed. Some techniques are successful and some techniques have achieved limited success. For the last few decades, ptychography has been evolving dramatically. Ptychography has been found to be more robust than other existing phase retrieval method, and it has shown potential to be implemented for x-rays and e-beams wavelengths. Ptychographic data is so rich in information that not only it retrieves the object function but also it can retrieve the probe function, 3D information of the object, coherent modes of the light, etc.

Ptychography is a phase retrieval technique which uses several far-field diffraction patterns of an object. These patterns are created by scanning the object sequentially using an illuminated probe. The probe position should be in a way that neighboring probes overlap with each other. Due to this overlap area, the ptychographic data contains redundancy and this helps the algorithm to converge fast.

When ptychography was implemented using e-beam, the reconstructions suffered from the required accuracy of initial parameters. For instance, 50 pm of accuracy is required in probe positions which is difficult to achieve. This high demand in accuracy undermined its applicability to short wavelengths. Therefore, several attempts were made to correct probe positions in ptychography.

In this thesis, we have devised two novel techniques which solve the probe position problem in ptychography. The first technique is intensity gradient (IG) method. As the name suggests, this method is based on the gradient of simulated intensity patterns. The gradient is taken along the X and Y directions and the equation is solved for position errors along the X and Y directions. This method has shown a few advantages over the state-of-the-art correction method which is based on cross-correlation. IG method is a straightforward extension of ptychographic iterative engine (PIE). Moreover, it is less computationally expensive than the cross-correlation method while achieving comparable accuracy. In IG method, sub-pixel accuracy has been achieved while in cross-correlation method, an additional method called matrix multiplication method has been used to achieve this high accuracy. Furthermore, we have validated our method with visible light experimental data.

The second technique is based on the well-known techniques the hybrid input-output (HIO) and cross-correlation. HIO is one of the classical phase retrieval methods which uses single intensity pattern. Whereas, cross-correlation calculates the shift between two identical images. These two techniques are combined in a way that it solves the probe position problem. Unlike the previous method, this method can only correct probe positions with integer pixel accuracy. In order to achieve sub-pixel accuracy, matrix multiplication method can be used as it is used in cross-correlation method. A comparison with IG method is also shown in this thesis. We have not found a case where this method outperforms the existing method. Furthermore, there is one limitation on the probe function since it should be zero outside the well- defined area. Due to this limitation, its applications are limited.

Besides the above mentioned two probe position correction methods, we have implemented ptychography for two applications. First application is for high-NA EUV lithography wavefront sensor where other techniques show limitation. We have implemented ptychography to retrieve the wavefront and eventually the present aberrations in the imaging system. The results are shown using simulated intensity patterns which have close resemblance to expected EUVL experiment.

Second application is for coherent Fourier scatterometry (CFS). CFS is a newly developed technique to retrieve the grating parameters and is applicable for semiconductor industries. Phase information of scattered field provides higher accuracy in determining the grating parameters. Therefore, we retrieved the amplitude and phase of the scattered field using ptychography. The results are comparable with the one retrieved from interferometry. Hence, we have proposed here to replace interferometer—an cumbersome set up to implement—with ptychography.

We anticipate that the work presented in this thesis can be used to replace current computationally expensive and complex algorithms in ptychography. Electron ptychography and x-rays ptychography can be implemented using this method which can achieve high-resolution images of biological samples and nano-materials. Besides, the probe position method based on HIO and cross-correlation method gives a new insight to understand the probe positions problem. Although, position correction methods are devised for real space ptychography, however they are not limited to real space ptychography and further, it can be implemented for Fourier ptychography as well. Moreover, two new applications of ptychography are

explored here which were untouched by the ptychography community. Ptychography has shown significant improvement for these applications. We hope that we have motivated the reader enough to continue with the following chapters for more details.

Samenvatting

Lenzen zijn onmisbare hulpmiddelen voor beeldvorming om zo de kleine details van een voorwerp te zien, wat anders niet mogelijk was. De kleinste details van een object die men met een lens kan zien, zijn afhankelijk van de numerieke apertuur (NA) van de lens en van de gebruikte golflengte van het licht. Voor een vaste NA geldt: hoe korter de golflengte, hoe kleiner de details die van een object nog kunnen worden gezien. Daarom worden voor hoge-resolutie beeldvorming korte golflengten zoals die van röntgenstralen en e-bundels gebruikt. Voor deze golflengten ligt de brekingsindex van de meeste materialen dichtbij 1. Hierdoor worden de stralen die door deze lenzen gaan niet afgebogen en worden ze uiteindelijk door de materialen geabsorbeerd. Om dit probleem te omzeilen, zijn verschillende soorten lenzen, diffractieve optische elementen, geïntroduceerd. Met deze lenzen is beeldvorming mogelijk, maar diffractie-beperkte resolutie kan niet worden bereikt. De redenen hiervoor zijn de aberraties die in de beeldvormende systemen aanwezig zijn. Hierdoor zijn computationele beeldvormingsmethoden een grote rol gaan spelen.

Lensloze-beeldvorming is een vorm van computationele beeldvorming waarbij een lens wordt vervangen door een algoritme. Vandaar dat lensloze beeldvorming niet wordt beperkt door de aanwezige aberraties van de lens of het beeldvormende systeem. Bovendien kan met deze techniek niet alleen de amplitude maar ook de fase-informatie worden teruggevonden. Fase-informatie is belangrijk, vooral voor objecten met een laag contrast. Omdat deze algoritmen de fase van het object iteratief oplossen, worden ze ook wel fase-ophaaltechnieken genoemd.

In het verleden zijn verschillende technieken voorgesteld voor het oplossen van de fase. Sommige technieken zijn succesvol en sommige technieken hebben beperkt succes geboekt. De laatste paar decennia is ptychografie dramatisch geëvolueerd . Er is vastgesteld dat ptychografie robuuster is dan andere bestaande methoden voor fasebepaling en het heeft potentieel getoond voor implementatie voor röntgenstralen en golflengten van e-bundels. Ptychografische gegevens zijn zo rijk aan informatie dat niet alleen de objectfunctie wordt teruggehaald, maar ook de sondefunctie, 3D-informatie van het object, coherente modi van het licht, etc.

Ptychografie is een fase-ontsluitingstechniek waarbij verschillende verre-veld diffractiepatronen van een object worden gebruikt. Deze patronen worden gemaakt door het object sequentieel te scannen met behulp van een verlichte sonde. De positie van de sonde moet zodanig zijn dat naburige sondes elkaar overlappen. Vanwege dit overlappingsgebied bevatten de ptychografische gegevens redundantie; dit helpt het algoritme om snel te convergeren.

Toen ptychografie werd geïmplementeerd voor een e-beam, hadden reconstructies te lijden onder de vereiste nauwkeurigheid van de initiële parameters. Er is bijvoorbeeld 50 pm nauwkeurigheid vereist voor probeposities, hetgeen moeilijk te bereiken is. Deze hoge nauwkeurigheidseis ondermijnde de toepasbaarheid ervan

voor korte golflengten. Daarom zijn er verschillende pogingen ondernomen om probeposities in ptychografie te corrigeren.

In dit proefschrift hebben we twee nieuwe technieken bedacht waarmee het probleem van de sondepositie in ptychografie wordt opgelost. De eerste techniek is de intensiteitsgradiënt (IG) methode. Zoals de naam suggereert, is deze methode gebaseerd op de gradiënt van gesimuleerde intensiteitspatronen. De gradiënt wordt langs de X- en Y-richtingen genomen en de vergelijking wordt opgelost voor positiefouten langs de X- en Y-richtingen. Deze methode heeft enkele voordelen opgeleverd ten opzichte van de modernste correctiemethode die is gebaseerd op kruiscorrelatie. De IG-methode is een eenvoudige uitbreiding van de ptychographic iterative engine (PIE). Bovendien is deze tijdens de realisatie rekenkundig minder duur dan de kruiscorrelatiemethode terwijl er een vergelijkbare nauwkeurigheid verkregen wordt. Bij de IG-methode is sub-pixel nauwkeurigheid bereikt, terwijl bij de kruiscorrelatiemethode een extra methode genaamd matrixvermenigvuldigingsmethode wordt gebruikt om deze hoge nauwkeurigheid te bereiken. Verder hebben we onze methode gevalideerd met experimentele data in het zichtbare licht domein.

De tweede techniek is gebaseerd op de welbekende technieken, hybride input-output (HIO) en kruiscorrelatie. HIO is een van de klassieke faseherwinningsmethoden waarbij gebruik wordt gemaakt van één intensiteitspatroon, terwijl bij kruiscorrelatie de verschuiving tussen twee identieke afbeeldingen wordt berekend. Deze twee technieken worden zodanig gecombineerd dat het probleem met de sondepositie wordt opgelost. In tegenstelling tot de vorige methode, kan deze methode de sondeposities alleen op pixelniveau corrigeren. Om sub-pixel nauwkeurigheid te bereiken, kan de matrixvermenigvuldigingsmethode worden gebruikt zoals deze wordt toegepast bij de kruiscorrelatiemethode. Ook wordt in dit proefschrift een vergelijking met de IG-methode getoond. We hebben geen enkel geval gevonden waarin deze methode beter presteert dan de bestaande methode. Verder is er een beperking aan de sondefunctie, aangezien deze buiten het goed gedefinieerde gebied nul zou moeten zijn. Vanwege deze beperking zijn de toepassingen beperkt.

Naast de bovengenoemden correctiemethoden voor de sondepositie, hebben we ptychografie voor twee toepassingen geïmplementeerd. De eerste toepassing is voor een hoog-NA EUV-lithografie wavefront-sensor waar andere technieken beperkingen tonen. We hebben ptychografie geïmplementeerd om het golffront en uiteindelijk de aberraties, die aanwezig zijn in het beeldvormende systeem, terug te vinden. De resultaten worden getoond met behulp van gesimuleerde intensiteitspatronen die een grote gelijkenis vertonen met het verwachte EUVL-experiment.

De tweede toepassing is voor coherente Fourier-scatterometrie (CFS). CFS is een nieuw ontwikkelde techniek om de roosterparameters te verkrijgen en is toepasbaar voor halfgeleiderindustrieën. De fase-informatie van het verstrooide veld biedt een hogere nauwkeurigheid bij het bepalen van de roosterparameters. Daarom hebben we de amplitude en de fase van het verstrooide veld bepaald met behulp van ptychografie. De resultaten zijn vergelijkbaar met die verkregen uit interferometrie. Daarom hebben we hier voorgesteld om de interferometer—een moeilijk hanteerbare opstelling om te implementeren—te vervangen door ptychografie.

We verwachten dat het werk gepresenteerd in dit proefschrift kan worden ge-

bruikt om huidige computationeel dure en complexe algoritmen in ptychografie te vervangen. Elektron ptychografie en x-ray ptychografie kunnen geïmplementeerd worden met behulp van deze methode om afbeeldingen met een hoge resolutie te verkrijgen van biologische monsters en nanomaterialen. Daarnaast geeft de methode voor sondeposities op basis van HIO en de methode voor kruiscorrelatie nieuwe inzichten om het sonde positie-probleem te begrijpen. Hoewel methoden voor positiecorrectie zijn bedacht voor real space ptychografie, zijn deze niet beperkt tot real space ptychografie; ze kunnen ze ook geïmplementeerd worden voor Fourier ptychografie. Bovendien worden hier twee nieuwe toepassingen van ptychografie verkend die onaangeroerd waren door de ptychografie-gemeenschap. Ptychografie heeft een significante verbetering laten zien voor deze applicaties. We hopen dat we de lezer voldoende hebben gemotiveerd om door te gaan met de volgende hoofdstukken voor meer details.

1

Introduction

1.1. Motivation

Being able to see the smallest feature of a biological sample or an integrated chip (IC) is vital to inspect diseases or to find the faulty chips for the semiconductor industry. Imaging plays a crucial role in resolving small features which can not be seen from our naked eyes. The smallest feature one can resolve through an imaging system depends upon the wavelength of the used light and numerical aperture (NA) of the imaging system. The shorter the wavelength is, the smaller the feature that can be seen. In other words, for fixed NA, the resolution of an image increases as we use short wavelengths.

Short wavelengths—X-rays and e-beams—are used to achieve high-resolution imaging. However, conventional lenses can not be used for short wavelengths, and unconventional focusing optics do not have enough efficiency to achieve diffraction limited resolution. Furthermore, the experimental set-up should be highly stable. Hence, to circumvent these problems, lensless imaging was proposed: replacing lenses with algorithms. Another motivation of lensless imaging was the phase information, since it gives better image contrast, especially for low absorbing objects [1].

Coherent diffraction imaging (CDI) is a type of lensless imaging technique. In CDI, the diffracted light from an object is recorded in the camera, and the measured intensity is used to reconstruct the image of the object computationally. While capturing the intensity pattern, the phase is lost as the camera is not fast enough to capture the phase information. This problem is also known as the phase problem. CDI is an iterative method which minimizes the difference between the measured and estimated intensity at each iteration. In the end, it solves for the amplitude and phase of the object.

Based on how many intensity patterns are recorded, CDI is divided into two parts: single intensity method and multiple intensity method. Ptychography is a type of CDI which uses several far-field intensity patterns corresponding to parts of

1

the object. Ptychography is found to be superior to other single intensity methods.

1.2. Background

With the advent of computers, the computational power became cheaper, whereas the optical components remained comparatively expensive. Consequently, computer algorithms started to replace some of the optical components in imaging. This development helped in reducing the cost and simplifying the imaging systems. Moreover, 3D imaging and phase information can also be retrieved with computational imaging, unlike conventional imaging. In computational imaging, measurements are taken in a way that algorithms can be applied to retrieve the image [2]. These measurements can be taken with or without optical components. As the computational power became ubiquitously available, the algorithm became sophisticated.

Coherent Diffractive Imaging (CDI)—a type of computational imaging—reconstructs the object from the far-field measurements of the object. If the far-field of the object is

$$\Psi(\mathbf{u}) = A(\mathbf{u})e^{i\phi(\mathbf{u})}, \tag{1.1}$$

then the measured intensity pattern will be

$$I(\mathbf{u}) = \Psi(\mathbf{u})\Psi^*(\mathbf{u}) = |A|^2, \tag{1.2}$$

and the phase is lost. Here, $A(\mathbf{u})$ and $\phi(\mathbf{u})$ are the amplitude and phase of the object, and $\mathbf{u}$ is the co-ordinate in reciprocal space. Retrieving the object from only amplitude information is difficult. CDI techniques are iterative methods which retrieve the phase of the far-field, and by taking inverse Fourier transform of the far-field, the object is reconstructed eventually.

Several attempts were made in the last few decades to come up with a robust CDI technique. These are also called phase retrieval methods. Some examples of CDI are the error-reduction (ER) [3], the hybrid input-output (HIO) [4], the averaged successive reflections (ASR) [5], the hybrid projection reflection (HPR) [6], and relaxed averaged alternating reflectors (RAAR) [7]. These techniques are based on a single intensity of the object. Some of these methods suffer from the twin image problem, noise, or convergence to local minima. Due to these problems, the lensless imaging achieved limited success.

Ptychography iterative engine (PIE) has solved all these problems. In PIE, an object is partially illuminated either by placing an aperture in the front of the object or by using a localized illuminating probe on the object. Subsequently, the object is scanned by the probe, and the corresponding intensity patterns are measured in the far-field. These intensity patterns are used to reconstruct the object. Hence, unlike previously explained techniques, PIE is based on multiple intensity patterns. The most critical factor for the success of PIE is the overlap between the neighboring aperture/probe positions. The redundancy due to this overlap makes the algorithm robust.

The reconstruction quality of the object in PIE is dependent on accurately known initial parameters: probe function, probe position, coherence of the light, and object

thickness. Several variants of the ptychography are developed to incorporate the uncertainties in these parameters. For example, ePIE reconstructs the object as well as probe function [8]. Ptychography with positions correction can reconstruct the object and the probe positions [9–13]. Furthermore, partial coherence can also be recovered from the measurements [14]. Another remarkable extension to PIE is called 3PIE that allows reconstruction of a 3D object [15]. These variants can also be combined to solve for more than two unknown parameters. For instance, if we combine ePIE with positions correction, the solution of this combined algorithm will be the object, probe, and probe positions.

Due to its ability to solve for the object as well as other unknown parameters, ptychography has become very popular and it has been demonstrated in various wavelength ranges—visible, X-ray, e-beam, and EUV [16–19]. Because of its widespread applicability, ptychography has been used for various applications, for example, imaging 3D structure of a grating with EUV [20], imaging 3D structure of bone [17], imaging structural information of materials with atomic resolution [21]. Moreover, microscopy without lenses with visible light was implemented [22] and later on, with a crucial modification in ptychography, it was used for wide-field and high-resolution imaging in microscopy, which has revolutionized the field of microscopy [23].

1.3. Problem description

As previously explained, accurate information of initial parameters is essential for the better reconstruction of an object in ptychography. The results with visible light due to a small error in probe positions were not that much affected as in the case with X-rays or e-beams. For electron ptychography, the probe positions should be known as accurate as 50 pm, which is difficult to achieve. Because even a small thermal shift can lead to 50 pm of a shift in the probe positions. Hence, this problem needs to be addressed. Previously, several attempts were made to solve this problem. Few of them were successful to correct the probe positions with sub-pixel accuracy and few have achieved limited success.

We would pose the following research questions in this thesis:

- What are the current existing techniques to correct probe positions in ptychography?
- How to improve or come up with new techniques which are easy to implement?
- Is there any direct technique?
- Can we apply these techniques for short wavelengths such as EUV Lithography and other non-imaging methods such as coherent Fourier scatterometry?

1.4. Outline

This thesis consists of the following chapters:

- **Chapter 2:** Fundamentals of lensless imaging. This chapter sheds light on the historical overview of lensless imaging and the phase problem. Furthermore, we discuss few existing phase retrieval algorithms which are based on single intensity and multiple intensities. Ptychography—a method based on multiple intensities—is explained in detail. Then, we discuss the problems faced while implementing ptychography and detail its extension to solve the corresponding problem.
- **Chapter 3:** Probe position correction in ptychography using intensity gradient method. Here, we introduce our novel technique to correct the probe position in ptychography which uses the gradient of intensity pattern in the far-field. Then, we analyze the performance of this technique in the presence of noise, varying overlaps, and different initial probe position errors. We have also shown a comparison of this method with the state-of-the-art technique to correct the probe positions and present concrete conclusions. This proposed method has also been tested with visible light experimental data.
- **Chapter 4:** Probe position correction in ptychography using hybrid input-output (HIO) and cross-correlation. In this chapter, we propose another technique to correct the probe position which is based on hybrid input-output and cross-correlation. HIO and cross-correlation are well-known techniques to solve for the phase and to find the shift between two images. Here, we have combined them in a way that it can also correct the probe positions in pytchography. Several simulation results are shown to analyze its performance and robustness with varying parameters and in the presence of noise. Furthermore, a comparison between the proposed method in this chapter and the previous chapter is performed. Finally, we conclude this chapter by presenting its pros and cons with respect to other existing methods.
- **Chapter 5:** Application I: Wavefront sensor for EUV Lithography. We show an application where we have implemented extended ptychography iterative engine (ePIE) with probe positions correction. This chapter presents how ptychography with probe position correction method work for EUV wavefront correction. This can be used as a wavefront sensor for high-NA EUV Lithography where other techniques have limitations.
- **Chapter 6:** Application II: Phase retrieval for coherent Fourier scatterometry. In this chapter, we have implemented ptychography for coherent Fourier scatterometry (CFS). CFS is an optical metrology technique which reconstructs the grating structure from its far-field information. It is known that in addition to amplitude information of the scattered field of a grating, phase information helps in retrieving the grating parameters with increased accuracy [24]. Therefore, we suggest using ptychography to retrieve the phase of the scattered field for enhanced grating parameters.
- **Chapter 7:** Discussion and conclusions. Here, we summarize the thesis and discuss the possible future work.

References

[1] A. Momose. Recent advances in x-ray phase imaging. *Japanese Journal of Applied Physics*, 44(9A):6355–6367, 2005.

[2] J. N. Mait, G. W. Euliss, and R. A. Athale. Computational imaging. *Advances in Optics and Photonics*, 10(2):409–483, 2018.

[3] R. W. Gerchberg and W. O. Saxton. *Optik*, 35(237), 1972.

[4] J. R. Fienup. Phase retrieval algorithms: a comparison. *Applied optics*, 21(15):2758–2769, 1982.

[5] H. H. Bauschke, P. L. Combettes, and D. R. Luke. Phase retrieval, error reduction algorithm, and Fienup variants: a view from convex optimization. *Journal of the Optical Society of America A*, 19(7):1334–1345, 2002.

[6] H. H. Bauschke, P. L. Combettes, and D. R. Luke. Hybrid projection–reflection method for phase retrieval. *Journal of the Optical Society of America A*, 20(6):1025–1034, 2003.

[7] D. R. Luke. Relaxed averaged alternating reflections for diffraction imaging. *Inverse Problems*, 21(1):37–50, 2004.

[8] A. M. Maiden and J. M. Rodenburg. An improved ptychographical phase retrieval algorithm for diffractive imaging. *Ultramicroscopy*, 109(10):1256–1262, 2009.

[9] M. Guizar-Sicairos and J. R. Fienup. Phase retrieval with transverse translation diversity: a nonlinear optimization approach. *Optics Express*, 16(10):7264–7278, 2008.

[10] A. M. Maiden, M. J. Humphry, M. C. Sarahan, B. Kraus, and J. M. Rodenburg. An annealing algorithm to correct positioning errors in ptychography. *Ultramicroscopy*, 120:64–72, 2012.

[11] M. Beckers, T. Senkbeil, T. Gorniak, K. Giewekemeyer, T. Salditt, and A. Rosenhahn. Drift correction in ptychographic diffractive imaging. *Ultramicroscopy*, 126:44–47, 2013.

[12] F. Zhang, I. Peterson, J. Vila-Comamala, A. Diaz, F. Berenguer, R. Bean, B. Chen, A. Menzel, I. K. Robinson, and J. M. Rodenburg. Translation position determination in ptychographic coherent diffraction imaging. *Optics Express*, 21(11):13592–13606, 2013.

[13] A. Tripathi, I. McNulty, and O. G. Shpyrko. Ptychographic overlap constraint errors and the limits of their numerical recovery using conjugate gradient descent methods. *Optics Express*, 22(2):1452–1466, 2014.

[14] D. J. Bateya, D. Clausa, and J. M. Rodenburg. Information multiplexing in ptychography. *Ultramicroscopy*, 138:13–21, 2014.

[15] A. M. Maiden, M. J. Humphry, and J. M. Rodenburg. Ptychographic transmission microscopy in three dimensions using a multi-slice approach. *J. Opt. Soc. Am. A*, 29(8):1606–1614, 2012.

[16] A. M. Maiden, M. J. Humphry, F. Zhang, and J. M. Rodenburg. Superresolution imaging via ptychography. *Journal of the Optical Society of America A*, 28(4):604–612, 2011.

[17] M. Dierolf, A. T. P. Menzel, P. Schneider, C. M. Kewish, R. Wepf, O. Bunk, and F. Pfeiffer. Ptychographic x-ray computed tomography at the nanoscale. *Nature*, 467:436–439, 2010.

[18] C. T. Putkunz, A. J. D'Alfonso, A. J. Morgan, M. Weyland, C. Dwyer, L. Bourgeois, J. Etheridge, A. Roberts, R. E. Scholten, K. A. Nugent, and L. J. Allen. Atom-scale ptychographic electron diffractive imaging of boron nitride cones. *Physical Review Letters*, 108, 2012.

[19] D. F. Gardner, M. Tanksalvala, E. R. Shanblatt, X. Zhang, B. R. Galloway, C. L. Porter, R. K. Jr, C. Bevis, D. E. Adams, H. C. Kapteyn, M. M. Murnane, and G. F. Mancini. Subwavelength coherent imaging of periodic samples using a 13.5 nm tabletop high-harmonic light source. *Nature Photonics*, 11:259–263, 2017.

[20] M. Holler, M. Guizar-Sicairos, E. H. R. Tsai, R. Dinapoli, E. Müller, O. Bunk, J. Raabe, and G. Aeppli. High-resolution non-destructive three-dimensional imaging of integrated circuits. *Nature*, 543:402–406, 2017.

[21] P. Wang, F. Zhang, S. Gao, M. Zhang, and A. I. Kirkland. Electron ptychographic diffractive imaging of boron atoms in LaB_6 crystals. *Scientific Reports*, 7(2857), 2017.

[22] J. M. Rodenburg, A. C. Hurst, and A. G. Cullis. Transmission microscopy without lenses for objects of unlimited size. *Ultramicroscopy*, 107:227–231, 2007.

[23] G. Zheng, R. Horstmeyer, and C. Yang. Wide-field, high-resolution fourier ptychographic microscopy. *Nature Photonics*, 7:739–745, 2013.

[24] S. Roy, N. Kumar, S. F. Pereira, and H. P. Urbach. Interferometric coherent fourier scatterometry: a method for obtaining high sensitivity in the optical inverse-grating problem. *Journal of Optics*, 15(7), 2013.

2

Fundamentals of lensless imaging

In the previous chapter, we have given an overview of the problem that we are trying to solve with a brief background. The research problem of this thesis is concentrated on how to correct probe positions efficiently in Ptychography. In this chapter, we focus our attention on the detailed background and historical overview. Furthermore, we explain the principal technique of this thesis: ptychography. The chapter also develops around it with the explanation about the similar existing techniques and further developments in ptychography.

2.1. Limitations of lenses in imaging

Transmission electron microscopes (TEM) and X-ray microscopes are indispensable tool for material science research, nanostructure characterization, and inspection of biological samples [1–5]. These microscopes are used for different applications because of the different wavelength used and their characteristics. Due to small penetration depth, e-beams cannot be used to image a thick sample; X-rays are used to image a 3D sample to exploit its higher penetration depth. Furthermore, e-beams cannot be used to image a wet biological sample as it is absorbed by the present water, while this is not the case for X-rays. On the other hand, e-beams have better-focusing optics than for X-rays. Thus, each microscope has its own advantages and drawbacks. In summary, therefore, X-ray microscopes are favorable tools for imaging biological samples, and electron microscopes are used for inspecting material structures.

Short wavelengths—X-rays and e-beams—are considered for high-resolution imaging. However, the focusing optics for these wavelengths are not conventional lenses. Since the refractive index of most of the materials for these wavelengths is close to 1, the light passes through the material without deviation and gets absorbed eventually [6]. Therefore, different approaches were opted to image using

these wavelengths.

Electromagnetic lenses are used to focus e-beams due to its charged particle nature. However, one can not exploit its short wavelength completely to achieve diffraction limited resolution. In other words, the diffraction limited resolution can not be achieved in TEM. One of the limitations is the present aberrations in the lenses.

The focusing optics for X-rays were still a puzzle while the electromagnetic lenses were used for e-beam. Later on, by the introduction of laue lenses, grazing mirror, and Fresnel zone plate (FZP), the imaging could be performed with X-rays as well. There is progress in Fresnel zone plates, Laue lenses in the direction of tight focusing of x rays, but the fabrication, efficiency, and maximum obtained numerical apertures are the main challenges [7–10]. Therefore, for X-ray microscope, the aforementioned reasons are the limitations to achieve diffraction limited resolution.

2.2. Lensless imaging

The cradle of lensless imaging dates back to 1948. Dennis Gabor, motivated by correcting the aberrations of the electron microscopes, came up with an ingenious idea at that time, and he called holography [11]. The electron lenses of electron microscopes were suffering from spherical aberrations and were impossible to correct. Gabor suggested recording the amplitude and phase of the wavefield in a way that it can be reproduced at optical wavelengths where the conventional techniques can be used to correct the aberrations. Although this technique was not completely successful for this application, holography got popularity for optical wavelengths.

Gabor proposed to record the interference pattern created by a primary wave (i.e., reference wave) and secondary wave (scatter wave by an object) on a photographic plate. This interference recording is called hologram, and it will have maxima where the primary wave and secondary wave have the same phase. Therefore, on illuminating the hologram by the primary wave, the transmission wave should have the same phase as the secondary wave, and the amplitude variation of the transmission wave will be similar to the amplitude of the secondary wave. Hence, the original wave field is reconstructed. In Fig. 2.1, the principle of holography is explained.

Optical holography was implemented using a high-pressure arc mercury lamp. Since the used source did not have enough coherence length, Gabor used a small pinhole in front of the source. To create a clear hologram, long exposure time (of the order of minutes) was required [12]. Due to the stringent experimental conditions, holography had an eclipse period for a decade until the invention of the laser in 1963 which brought long coherence length and high power.

At the same time, X-rays optics was also suffering from aberrations and inadequate focusing optics. However, due to the lack of powerful and coherent X-ray source, the holography was not proposed for X-rays. Baez, El-Sum, and Kirkpatrick implemented holography anyway with X-rays [13–15]. The first reconstructed visible image was a thin wire from an X-ray hologram recorded by Kellström two decades ago [16]. Soon it was realized that the produced interference pattern was not enough for reconstruction. The reason was that X-rays sources did not have

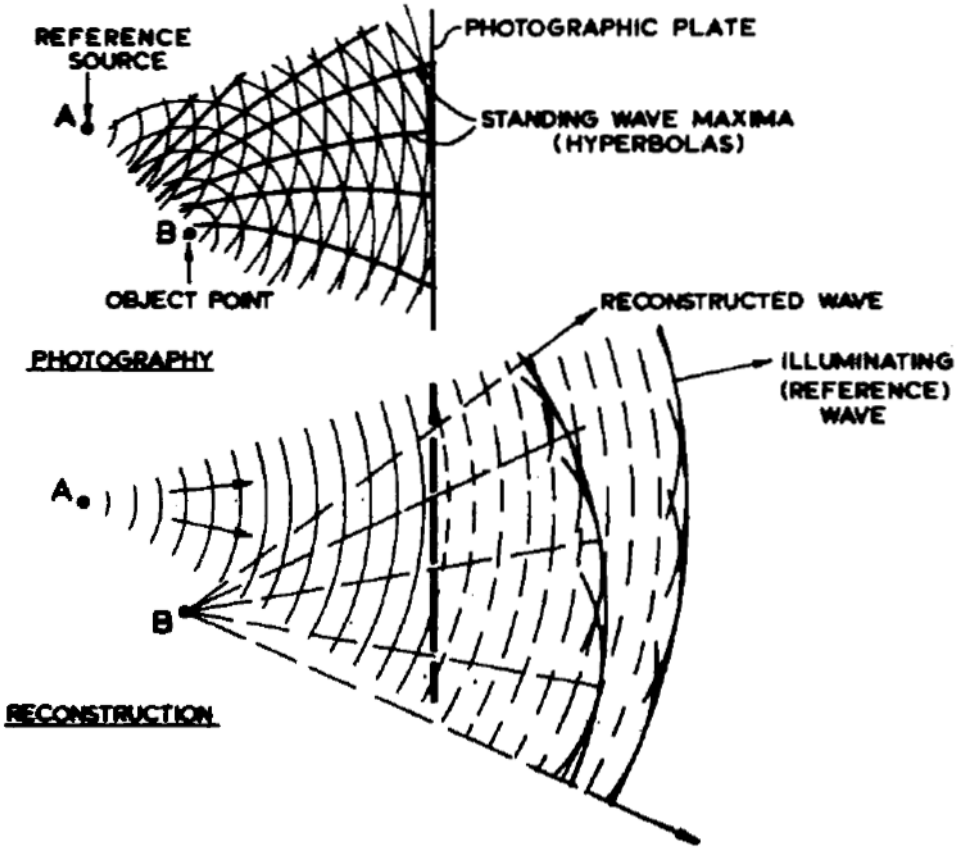

Figure 2.1: Principle of holography. This figure is taken from [12]

enough spatial and temporal coherence. These severe conditions made holography for X-ray impractical.

On the other hand, Gabor holography was motivated by X-rays crystallography: replace the lenses with image processing techniques. X-ray crystallography is used for determining the atomic distribution of crystalline structure. X-ray diffracts from the crystalline structure due to its short wavelength and produces a diffraction pattern containing Bragg's peak. With a priori information of the crystal, crystallographer reconstructs the 3D image of electron density of atoms in the crystal. This technique is only applicable to crystalline or periodic structures.

D. Sayre was the first to propose the extension of crystallography technique for non-crystalline structures, and this idea gradually developed [17–21]. Hayes and Bates proposed oversampling of the diffraction pattern to retrieve the complex object which later on found to share the roots with Fienup's hybrid input-output algorithm [22, 23]. Then, oversampling in a combination of iterative schemes was

implemented [24]. After two decades, Miao successfully imaged a non-crystalline specimen with a resolution of ~75 nm using soft X-rays and later on, it retrieved the 3D information as well [25, 26]. All these methods, in principle, were solving for the lost phase which had been the long-standing problem. In the next section, we will discuss the phase problem in detail.

In Fig. 2.2, the schematic of conventional imaging and lensless imaging are shown. In conventional imaging, the resolution of an image is given by

$$r = \frac{\lambda}{NA}. \tag{2.1}$$

Here λ is the wavelength of the light and *NA* is the numerical aperture of a lens. Hence, in conventional imaging, resolution of an image depends on the *NA* of the lens whereas, in lensless imaging, it depends on the *NA* of the detector. One might think to increase the *NA* of the lens to have higher resolution, but this causes to increase of aberrations. On the other hand, the increase of *NA* of the detector does not contribute to aberrations. Furthermore, conventional imaging is direct while lensless imaging is an iterative process—an indirect imaging technique.

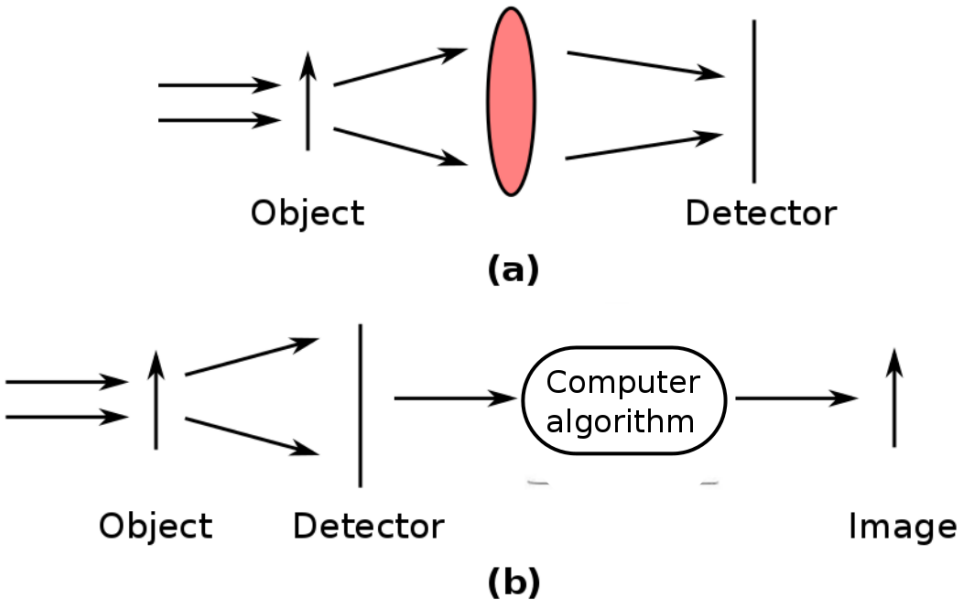

Figure 2.2: Conventional imaging and lensless imaging.

2.3. Phase problem

Light detectors can detect only the intensity of the light while the phase is lost during the measurements. It is due to the fact that the light has higher frequency than a camera can actually detect. In order to look at this problem theoretically,

let us suppose the unknown object $\psi(\mathbf{r})$ is propagated to the far-field, where the detector is placed. The object at the detector will be

$$\Psi(\mathbf{u}) = \mathfrak{F}\{\psi(\mathbf{r})\}, \tag{2.2}$$

and the intensity captured by camera will be

$$I(\mathbf{u}) = |\Psi(\mathbf{u})|^2. \tag{2.3}$$

Here, $\mathbf{r}$ and $\mathbf{u}$ are the coordinate vectors in the real and reciprocal space respectively. $\mathfrak{F}$ is the Fourier transform operation.

To retrieve the amplitude and phase information of $\Psi(\mathbf{u})$ from the measured intensity $I(\mathbf{u})$, is called the phase problem. In Fig. 2.3, the importance of phase is shown. Fig. 2.3(a) and (b) are two amplitude images. If we take the Fourier transform of the two and exchange the phase of the Fourier transform, subsequently take the inverse Fourier transform. The resulting images can be confused with each other. Moreover, phase information also provides better contrast.

2.4. Phase retrieval algorithms

To circumvent the phase problem, several phase retrieval techniques have been developed which we will discuss in this section. Please note that this section is not intended to give the complete overview. We present a few classic phase retrieval techniques and the ones which are used in this thesis. Phase retrieval algorithms, in general, are divided into two parts based on their process: direct method and indirect method. Direct methods are a non-iterative method which can retrieve the object directly; whereas, indirect methods are based on iterative schemes. We, in particular, emphasize on indirect methods in this section. Indirect methods are further divided into two parts: single intensity method, and multiple intensity method.

2.4.1. Single intensity method

In the single intensity method, one diffraction pattern of an object is used to reconstruct the object. Constraints in the real space and in the Fourier space are applied iteratively. Here, we have detailed the most used single intensity phase retrieval algorithms.

Error-reduction algorithm

Fienup modified the Gerchberg-Saxton (GS) algorithm to fit the phase retrieval problem. In the GS algorithm, partial information in two domains is used to retrieve the complex wave-field [27]. It can also be generalized for any two domains which are related to each other by a Fourier transform. Error-reduction (ER) is a form of GS algorithm where these domains are the object (or image) and the Fourier domain. The constraint in the Fourier domain is the same as in GS, whereas constraint in the object domain is modified. As its name suggests, the error in each iteration of error-reduction algorithm reduces [28].

If the wave function (the object) at the object plane is $\psi(\mathbf{r})$, the measured intensity at the Fourier plane will be

$$I(\mathbf{u}) = |\mathfrak{F}\{\psi(\mathbf{r})\}|^2. \tag{2.4}$$

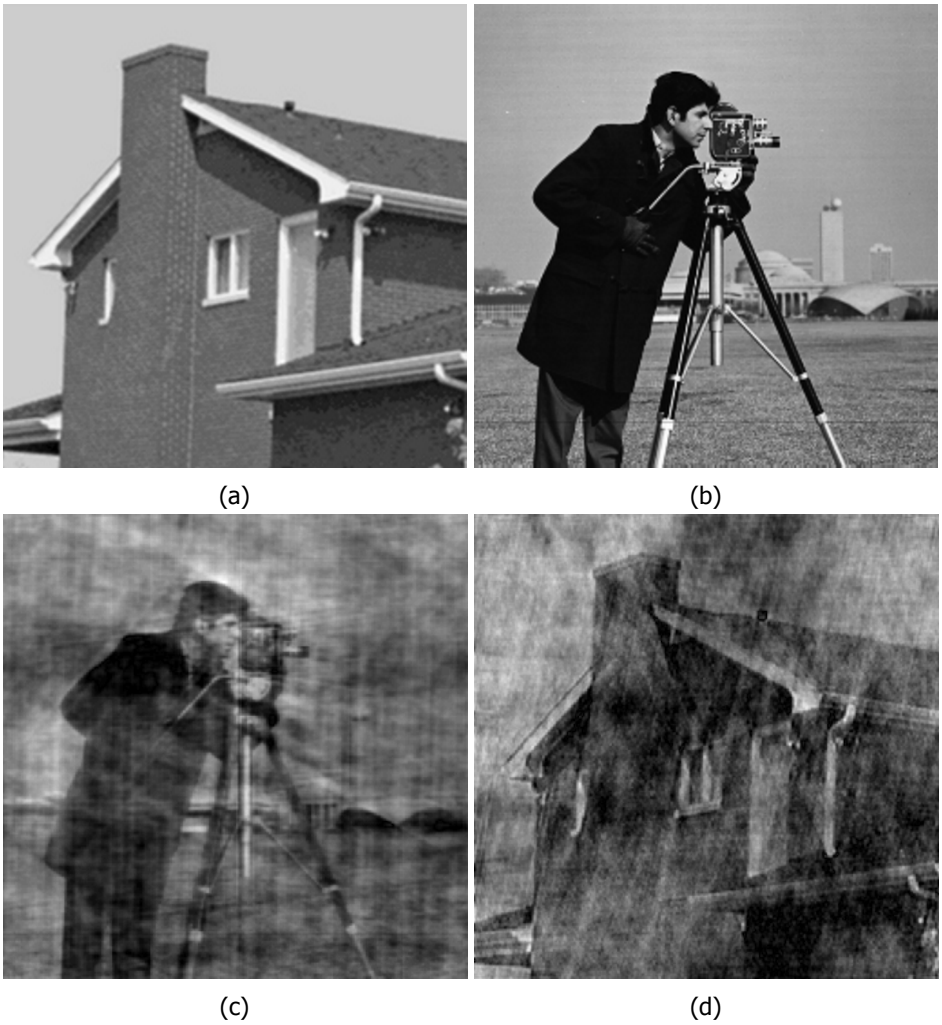

Figure 2.3: Importance of the phase measurement. (a) and (b) are two amplitude images on which the Fourier transform was performed. (c) and (d) are the resulting images when the phase of the Fourier transforms of (a) and (b) was exchanged and subsequently, the inverse Fourier transform of the new field was performed. The resulting images can be easily confused with the one another.

Let us assume, for k^{th} iteration, the estimated wave field at the object plane is $\psi_k(\mathbf{r})$. Then, the steps for the error-reduction algorithms are as follows:

1. Take the Fourier transform of the estimated wave field.

$$\Psi_k(\mathbf{u}) = \mathfrak{F}\{\psi_k(\mathbf{r})\}. \tag{2.5}$$

2. Apply amplitude constraint, i.e. replace the amplitude of the estimated far-field with the square root of the measured intensity $I(\mathbf{u})$ and keep the phase as it is.

$$\Psi'_k(\mathbf{u}) = \sqrt{I(\mathbf{u})}\frac{\Psi_k(\mathbf{u})}{|\Psi_k(\mathbf{u})|}. \tag{2.6}$$

3. Perform inverse Fourier transform on the updated far-field to obtain the wave field at the object plane.

$$\psi'_k(\mathbf{r}) = \mathfrak{F}^{-1}\{\Psi'_k(\mathbf{u})\}. \tag{2.7}$$

4. Apply support constraint. Support constraint is a set of points which violates the object domain constraint, i.e. these set of points exceeds the boundary of the object. Here, support constraint is denoted as S.

$$\psi_{k+1}(\mathbf{r}) = \begin{cases} \psi'_k(\mathbf{r}), & \mathbf{r} \notin S, \\ 0, & \mathbf{r} \in S. \end{cases} \tag{2.8}$$

These steps are repeated until it converges to the correct solution.

Input-output algorithm

ER requires an impractically high number of iterations to converge. To speed up the convergence rate, Fienup introduced an input-output approach [28]. He suggested to consider the steps from 1 to 3 of ER algorithm as a non-linear response function which has one input $\psi_{k+1}(\mathbf{r})$ and one output $\psi'_k(\mathbf{r})$. The important property of the output is that it will always satisfy the amplitude constraint in the Fourier domain. The next input $\psi_{k+1}(\mathbf{r})$ should not be thought as the best estimate of the output as is the case with ER, instead, it should act as a driving function for its next output $\psi'_{k+1}(\mathbf{r})$. This idea gave enough space to experiment.

Due to the non-linear response function (from step 1–3), a change in input will cause a change in output. Therefore, to have a desired change in the output of $\Delta\psi'_k(\mathbf{r})$, one should change the input by $\beta\Delta\psi_k(\mathbf{r})$. Here, β is constant. For the phase retrieval problem, one does not want to change the part of the object which satisfies the support constraint; whereas a change should be made to the part of the object which does not satisfy the support constraint in a way that it satisfies. Hence, the desired change in output is

$$\Delta\psi_k(\mathbf{r}) = \begin{cases} 0, & \mathbf{r} \notin S, \\ -\psi'_k(\mathbf{r}), & \mathbf{r} \in S. \end{cases} \tag{2.9}$$

Therefore, the next input will be

$$\psi_{k+1}(\mathbf{r}) = \psi_k(\mathbf{r}) + \beta\Delta\psi_k(\mathbf{r}), \tag{2.10}$$

$$= \begin{cases} \psi_k(\mathbf{r}), & \mathbf{r} \notin S, \\ \psi_k(\mathbf{r}) - \beta\psi'_k(\mathbf{r}), & \mathbf{r} \in S. \end{cases} \tag{2.11}$$

If the Eq. (2.11) is used instead of step 4 of the ER algorithm; the resultant algorithm is called input-input algorithm.

In yet another case, let us consider $\psi'_k(\mathbf{r})$ as input. Since $\psi'_k(\mathbf{r})$ already satisfies the support constraint in the Fourier domain, the output will be the same as input. Now, we consider the other way around case: if the output is $\psi'_k(\mathbf{r})$, the input can be considered the same irrespective of what input was. With this logic, we can write next input as

$$\psi_{k+1}(\mathbf{r}) = \psi'_k(\mathbf{r}) + \beta\Delta\psi_k(\mathbf{r}), \tag{2.12}$$

$$= \begin{cases} \psi'_k(\mathbf{r}), & \mathbf{r} \notin S, \\ \psi'_k(\mathbf{r}) - \beta\psi'_k(\mathbf{r}), & \mathbf{r} \in S. \end{cases} \tag{2.13}$$

This algorithm is named as output-output algorithm. This algorithm was found to stagnate, therefore hybrid input-output was derived from it.

If we combine the second line of the input-input algorithm and first line of the output-output algorithm, then we get a hybrid of the two which is called hybrid input-output (HIO) algorithm. Therefore, for HIO, the next input will be

$$\psi_{k+1}(\mathbf{r}) = \begin{cases} \psi'_k(\mathbf{r}), & \mathbf{r} \notin S, \\ \psi_k(\mathbf{r}) - \beta\psi'_k(\mathbf{r}), & \mathbf{r} \in S. \end{cases} \tag{2.14}$$

One important property of HIO is that it finds the neighbourhood of the solution faster than ER algorithm. On further iterating the algorithm, it starts to wander from the solution. Therefore, it is suggested to used ER after HIO for improved reconstruction [29].

Hybrid projection-reflection algorithm (HPR)

This algorithm proposed by H. H. Bauschke et al. is a projection-based method [30]. The update scheme is similar to HIO except non-negative constraint applied in the object domain in HPR. Hence, the next

$$\psi_{k+1}(\mathbf{r}) = \begin{cases} \psi'_k(\mathbf{r}), & \mathbf{r} \notin S \text{ and } \psi_k(\mathbf{r}) \geq 0, \\ \psi_k(\mathbf{r}) - \beta\psi'_k(\mathbf{r}), & \mathbf{r} \in S. \end{cases} \tag{2.15}$$

Once HPR finds the neighborhood of the solution, it also wanders from the solution on further performing the iterations which is similar to HIO. This is due to the non-convex nature of the constraint. On comparing with HIO, HPR gives superior reconstructions. However, HPR takes longer to find the neighborhood of the solution than HIO.

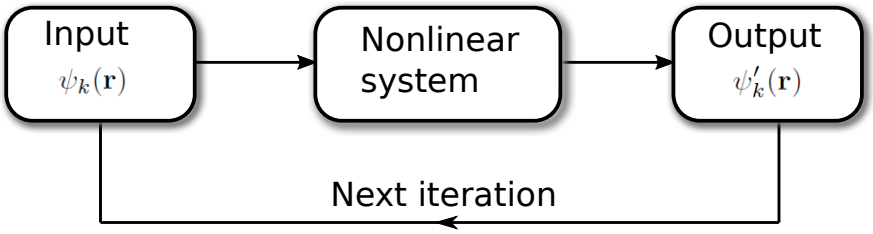

Figure 2.4: Input-output approach.

Relaxed averaged alternating reflector (RAAR)

The work for RAAR [31] algorithm was motivated from author's previous work hybrid projection reflection (HPR). RAAR was found to be superior than HIO and HPR. The step 4 of this algorithm is as :

$$\psi_{k+1}(\mathbf{r}) = \begin{cases} \psi'_k(\mathbf{r}), & \mathbf{r} \notin S, \\ \beta\psi_k(\mathbf{r}) + (1-2\beta)\psi'_k(\mathbf{r}), & \mathbf{r} \in S. \end{cases} \tag{2.16}$$

Here, the value of β depends on the used object. Nevertheless, it is recommended to use small β in the begining to relax the algorithm to find the neighbourhood of the solution, then increase the β to avoid any stagnation. It has also been successfully applied [32, 33]. One important observation is that HIO, HPR and RAAR will have the same update scheme if $\beta = 1$.

2.4.2. Multiple intensity method

Previously, we have described the phase retrieval methods which are based on the single intensity method. Motivated to invent a method which is fast to converge, robust and does not stagnate easily, multiple intensity method was proposed. The single intensity method can also stagnate at their twin image if the support constraint is centro-symmetric. Capturing multiple intensity patterns give additional redundant data which avoids this stagnation. There are several phase retrieval methods based on capturing multiple intensities, e.g., in Ref. [34, 35]; however, given the focus of this thesis, we will discuss ptychography in the following sections.

2.5. Ptychography

In 20th century, crystallographers exploited X-rays to image atomic resolution structures; however, it was limited for periodic objects. If the phase of the captured diffraction pattern could be retrieved in some way, then the image can also be retrieved by taking inverse Fourier transform of the diffraction pattern. Hoppe was certain that the phase problem can be solved using one diffraction pattern, but it would be challenging with the available computational power at that time [36]. However, the ambiguities that arise in the single diffraction pattern can be solved by recording at least two diffraction patterns either by shifting the illuminating probe on the object or by changing the probe [37]. Later on, in 1972, he changed the illumination function and called the technique ptychography [38].

The Greek word ptychography is made from "ptycho" and "graphy". "Ptycho" means "fold" which expresses one of the crucial property of ptychography: folding the diffraction orders with each other via the convolution of an aperture in the object plane. "Graphy" means "process of writing or recording". Ptychography was developed for a periodic object, and it was based on capturing multiple diffraction patterns by shifting the illumination on the object in a way that only the neighbouring diffraction orders should overlap with each other. Therefore, it was only applicable for a periodic or crystalline object and in 1995, it was applied to image a crystalline silicon [39]. For a non-periodic object, multiple diffraction orders overlap with each other which makes it unsuitable for ptychography. The benefits of ptychography were vague and unexplored compared with the existing diffraction and holographic methods at that time. Additionally, the unavailability of strong computational power was also one of the reason for other researchers to not pursue this idea.

Rodenburg and his team continued to work in the same direction to solve the phase problem and developed the inversion method, for example, the Wigner distribution deconvolution (WDD) method [40]. In 2004, Rodenburg's team came up with an outstanding iterative approach to solve the phase problem which was more robust and faster convergence rate than other exisiting methods [41, 42]. This iterative method was called Ptychography Iterative Engine (PIE). After the first successful implementation of PIE for X-rays experiment, it has received significant attention from the scientific community [43], and it was, furthermore, proposed for lensless microscopy [44].

2.5.1. Ptychography iterative engine (PIE)

Let us suppose that an object $O(\mathbf{r})$ is scanned by an illuminating probe $P(\mathbf{r} - \mathbf{R}^j)$, where $\mathbf{R}^j$ is the probe position vector. The intensity patterns corresponding to each probe positions are measured in the far-field as shown in the Fig. 2.5. Note that, mathematically, moving the probe or moving the object are same. One of the crucial factors for the success of ptychography in comparison to other iterative methods is the overlap between the neighbouring probe positions. This overlap provides the redundant information for the reconstruction. The optimum overlap should be arround 60% [45]. The captured intensity pattern in the far-field for j^{th}

probe position can be written as

$$I^j(\mathbf{u}) = \mathfrak{F}\{O(\mathbf{r})P(\mathbf{r} - \mathbf{R}^j)\}. \tag{2.17}$$

Here, **r** and **u** are the coordinate vectors in the real space and reciprocal space respectively. If J is the number of scanned probe positions, $j = 1, 2, 3, ...J$.

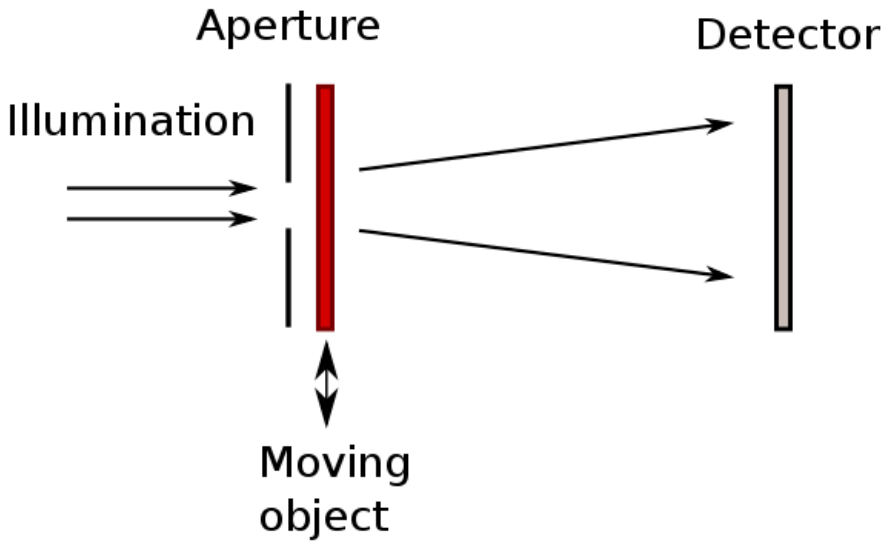

Figure 2.5: Ptychographic setup. A coherent light incident on an aperture which limit the light passing through the object. In this set-up, the object moves to several positions and diffraction patterns are recorded in the camera corresponding to each position.

With ptychography iterative engine (PIE), we are trying to solve for the object function $O(\mathbf{r})$ using the probe function $P(\mathbf{r})$ and the intensity patterns $I^j(\mathbf{r})$ for corresponding probe position j. If, for k^{th} iteration, the estimated object is denoted as $O_k(\mathbf{r})$, then the steps of the algorithm are as follows:

1. Calculate the exit wave-field $\psi_k^j(\mathbf{r})$ as

$$\psi_k^j(\mathbf{r}) = O_k(\mathbf{r})P(\mathbf{r} - \mathbf{R}^j). \tag{2.18}$$

2. Take the Fourier transform of $\psi_k^j(\mathbf{r})$ to calculate the far-field diffraction pattern $\Psi_k^j(\mathbf{u})$.

$$\Psi_k^j(\mathbf{u}) = \mathfrak{F}\{\psi_k^j(\mathbf{r})\}. \tag{2.19}$$

3. Apply the amplitude constraint, i.e., replace the amplitude of the far-field with the square root of measured intensity and keep the phase as it is.

$$\Psi_{c,k}^j(\mathbf{u}) = \sqrt{I^j(\mathbf{u})}\frac{\Psi_k^j(\mathbf{u})}{|\Psi_k^j(\mathbf{u})|}. \tag{2.20}$$

4. Take the inverse Fourier transform of the updated far-field.

$$\psi^j_{c,k}(\mathbf{r}) = \mathfrak{F}^{-1}\{\Psi^j_{c,k}(\mathbf{u})\}. \tag{2.21}$$

5. Apply the support constraint, i.e., modify the part of the object which was illuminated by the probe and keep the rest of the object unchanged.

$$O_{k+1}(\mathbf{r}) = O_k(\mathbf{r}) + \alpha \frac{P^*(\mathbf{r}-\mathbf{R}^j)}{|P^*(\mathbf{r}-\mathbf{R}^j)|^2_{\max}}(\psi^j_{c,k}(\mathbf{r}) - \psi^j_k(\mathbf{r})). \tag{2.22}$$

   α is a constant that define the update step, although we have used $\alpha = 1$ for the results shown in this thesis.

6. Move to the next probe position.

These steps are repeated until it converges. PIE is the first wide-field lensless imaging method that combines ptychography and iterative scheme. PIE was applied for visible and X-ray imaging [43, 44].

2.5.2. Extended ptychography iterative engine (ePIE)

PIE is found to be successful in solving the ambiguities which are not possible with single intensity methods. Furthermore, PIE is fairly robust to Poisson noise and initial parameters of the probe [46]. However, while implementing PIE for X-ray imaging, the reconstructions suffered due to the inaccurately known probe function [43]. To obtain accurate knowledge of probe can be time-consuming, and to measure the phase of the probe accurately is almost impossible for some cases. Therefore, several efforts were being made in this direction [47–49]. A straightforward extension of PIE—extended ptychography iterative engine (ePIE)—was developed by Rodenburg and his team, where they showed that the probe could also be reconstructed from the far-field successfully [50].

The update function for probe is analogous to object update function in PIE. If $P_k(\mathbf{r})$ is the estimated probe function for k^{th} iteration, the probe update function will be

$$P_{k+1}(\mathbf{r}) = P_k(\mathbf{r}) + \beta \frac{O^*_k(\mathbf{r}+\mathbf{R}^j)}{|O_k(\mathbf{r}+\mathbf{R}^j)|^2_{\max}}(\psi^j_{c,k}(\mathbf{r}) - \psi^j_k(\mathbf{r})). \tag{2.23}$$

ePIE was found to be more robust to noise than other existing probe retrieval techniques and has been intensively used for X-ray [51–57] visible [58–60] and e-beam [61–64] wavelengths.

2.5.3. Position correction in ptychography iterative engine

After ePIE, the requirement for accurately known probe function was relaxed. On implementing ePIE for short wavelengths (e.g., X-rays and e-beams), it was found that one of the factors for limited resolution was the accurate knowledge of the probe positions. In other words, the reconstruction suffered due to inaccurate probe positions [65–67]. For electron ptychography, the probe positions should

be as accurate as 50 pm [63]. This high accuracy was impossible to achieve as this could even be lead by thermal shift. Consequently, several techniques were proposed to solve this problem. Proposed methods that are based on drift model and genetic algorithm [68, 69], achieved limited success, while other successful methods are explained below.

- **Nonlinear optimization (NL) approach** [48]

  In 2008, a non-linear approach was proposed to solve for the object function, the probe function, and the translational positions [48]. In this approach, the author proposed to calculate the error metric and take the gradient w.r.t. unknown parameter. The error metric was defined as

$$\varepsilon = \sum_{j=1}^{J} \sum_{\mathbf{u},\mathbf{v}} W^j(\mathbf{u},\mathbf{v}) \left\{ \left(|\Psi_k^j(\mathbf{u},\mathbf{v})|^2 + \delta \right)^{\gamma} - \left(I^j(\mathbf{u},\mathbf{v}) + \delta \right)^{\gamma} \right\}^2. \tag{2.24}$$

  Here, $W^j(\mathbf{u},\mathbf{v})$ is the weighting parameter that has higher value for high signal to noise ration (SNR) region and low value for low SNR region. This can also be used for excluding the not-working-pixel in the camera by setting weighting parameter to zero. To avoid problem in calculating the gradient of error metric where intensity is close to zero, a small constant δ is added in the expression. The value of γ is 0.5.

  To solve for the object function, the derivative $\frac{\partial \varepsilon}{\partial O_k}$ is calculated, and the object is updated in the same direction. Analogously, to solve for the probe function and the probe positions, the derivatives $\frac{\partial \varepsilon}{\partial P_k}$ and $\frac{\partial \varepsilon}{\partial R_k^j}$ are calculated and updated along the same direction respectively. Note that, if the object is a complex function then the derivatives will be calculated for real and imaginary parts separately. This method was found to be superior to PIE. For example, in PIE, the reconstruction suffers from inaccurately known parameters; whereas, NL can incorporate the inaccurately known parameters given that the derivatives can be calculated easily.

- **Annealing method** [70]

  In this method, the estimated wavefront is calculated as

$$\psi_k^j(\mathbf{r}) = O_k(\mathbf{r}) P_k(\mathbf{r} - (\mathbf{R}_k^j + \mathbf{C}_k^j)). \tag{2.25}$$

  Here, $\mathbf{C}_k^j = (C_{k,x}^j, C_{k,y}^j)$ is the correcting vector. A set of $m = 1, 2, 3...M$ wavefronts are calculated by adding an offset $c\Delta_m$ to $\mathbf{C}_k^j$. Here, c is a constant whose value reduces as the iteration proceeds, and $\Delta_m = [\delta_{x,m}, \delta_{y,m}]$ where $\delta_{x,m}$ and $\delta_{y,m}$ are two random numbers between -1 to 1. Therefore, the estimated wavefronts for $m = 1, 2, ...M$ are computed as:

$$\psi_{k,m}^j(\mathbf{r}) = O_k(\mathbf{r}) P_k(\mathbf{r} - (\mathbf{R}_k^j + \mathbf{C}_k^j + c\Delta_m)). \tag{2.26}$$

Including $\psi_k^j(\mathbf{r})$ and $\{\psi_{k,m}^j(\mathbf{r})\}_{m=1}^M$, there are $M+1$ estimated exit wavefronts which are propagated to the far-field.

$$\{\Psi_{k,m}^j(\mathbf{u})\}_{m=0}^M = \{\Im\{\psi_{k,m}^j(\mathbf{r})\}\}_{m=0}^M. \tag{2.27}$$

The error between the measure far-field amplitude and the estimated far-field amplitude are computed:

$$E^j(m) = \sum_u \{\sqrt{I^j(\mathbf{u})} - |\Psi_{m,k}^j|\}^2. \tag{2.28}$$

If n is the index which corresponds to minimum error, in other words, if

$$n = min(arg(E^j(m))), \tag{2.29}$$

then

$$C_{k+1}^j = C_k^j + c\Delta_n. \tag{2.30}$$

This method was successful in correcting the probe positions; however, it is computationally expensive.

- **Cross-correlation method** [71]

  As the name suggests, this method is based on cross-correlation. The author suggested that cross-correlation between the part of the object illuminated by the probe for consecutive iterations will lead to the correct probe positions. The cross-correlation is

$$C_k^j(\boldsymbol{\rho}) = \sum_r O_{k+1}(\mathbf{r})P_k(\mathbf{r} - \mathbf{R}_k^j)O_k^*(\mathbf{r} - \boldsymbol{\rho})P_k^*(\mathbf{r} - \mathbf{R}_k^j - \boldsymbol{\rho}). \tag{2.31}$$

  Location of the maxima of the $C_k^j(\boldsymbol{\rho})$ gives the shift error $\mathbf{e}_k^j$. Subsequently, the probe positions are updated as

$$\mathbf{R}_{k+1}^j = \mathbf{R}_k^j + \beta\mathbf{e}_k^j \tag{2.32}$$

  Here, β is a constant and its range can be from 50 to 300. Large value of β leads to high convergence rate; whereas small value of β leads to the finer correction of probe positions. Therefore, in the beginning of the simulations, large value of β is recommended, and small value of β is used after performing few iterations. This method is the most successful method than previously existing methods. It can correct higher error in the probe positions even in the presence of substantially high shot noise.

- **Non-linear using conjugate gradient method** [72]

  In 2014, there was another method devised by A. Tripathi et al. which is based on non-linear optimization analogous to Fienup's method [48]. In Ref. [48], to correct probe positions, it could easily be trapped in the local minima

because several parameters are updated simultaneously. To improve upon this method, Ref. [72] suggested combining non-linear optimization with ePIE or difference map algorithm. It has found significant improvement. In the previous method [48], the probe positions can be corrected less than one pixel whereas, in this method [72], the higher error can be corrected even in the presence of noise. One drawback of A. Tripathi's method is that it can not correct with sub-pixel accuracy. For sub-pixel accuracy, one is required to use the cross-correlation method.

2.5.4. Variants

- **Fourier ptychography** [73]: The fundamental limitation of imaging is defined by space-bandwidth product (SBP) [74]. For an optical system, high SBP is required; however, in practice, it is not possible due to inherent optical aberrations. Therefore, one has to compromise between high-resolution imaging and wide-field imaging. On other hand, W. Lukosz defined N as the product of object area, optical bandwidth, number of temporal degree of freedom, and a factor 2 which is the number of independent state of polarization [75, 76]. This N is invariant for any optical system. Therefore, in order to increase the spatial bandwidth, one has to decrease one of the previously mentioned parameters. For instance, by decreasing the temporal bandwidth, transfer of spatial frequency will be incrased. This can be achieved by using multiple coehrent beams with different temporal coherency at varying angle. The same is applied in Fourier Ptychography to increase the spatial resolution of the object. Fourier ptychography (FP) revolutionized the field of microscopy by providing high-resolution and wide field of view at the same time with additional measurements and computation [73]. For FP set-up, the light source of a microscope is replaced by an array of LED light. Each LED is switched on sequentially and the corresponding low-resolution image is captured in the camera. Using these images, FP stitches in the Fourier plane using the iterative process to achieve high-resolution, wide-field and complex image.

- **Floating ptychography** [77]: Floating ptychography is useful for undersampled diffraction intensity patterns. For example, it can be used when the central part of the beam is blocked or when the detector size significantly limits the diffraction pattern [60]. In the forward propagated wave field, the amplitude constraints are applied only for the measured points (measured intensity), the rest points are kept as it is.

- **Ptychography for partially coherent light** [78, 79]: Ptychography, being a coherent diffractive imaging technique, requires the illumination to be coherent. To incorporate the partial coherent illumination, one of the techniques is based on decomposing the illumination as an incoherent sum of coherent modes.

- **3PIE** [80]: In ptychography, we multiply the complex transmission function of the object with probe function to calculate the exit wave. However, this

approximation does not hold for thick objects or objects with multiple scattering effects. 3PIE uses multi-slice approach to divide the 3D objects into several layers that hold the simple multiplication of incident probe and the transmission function of that layer. Therefore, in the forward model, 3PIE considers several thin layers in contrast to one single layer.

- **Vectorial ptychography** [81]: Ptychography assumes the illumination to be scalar; hence it is being implemented for a scalar field. To investigate the anisotropic properties of an object, vectorial ptychography was proposed.
- **Single-shot ptychography** [82]: Ptychographic data is recorded by moving the object or the probe to several translational positions. This process can require a long acquisition time. Therefore, single-shot ptychography was introduced to record the ptychographic data in single-shot. In this technique, the object is illuminated by several overlapping illuminations coming from different angles and the diffraction pattern is recorded in the camera. Due to different incidence angles, the diffraction pattern corresponding to each illumination is separated from each other in the camera. That is how the ptychographic data are recorded in one shot, and PIE is used to reconstruct the object.
- **Bragg ptychography** [83–86]: The diffraction pattern of an ideal crystalline structure contains identical copies at each Bragg peak. However, it will no longer be identical in the presence of strains or defects. Therefore, CDI is used to image a strain field or defects of a crystalline material.
- **Fresnel Ptychography** [87, 88]: It is a combination of Fresnel coherent diffractive imaging (FCDI) and ptychography. It exploits the benefits of FCDI in ptychography. The main benefit of Fresnel ptychography compared to conventional ptychography is its faster convergence rate, small overlap requirement, and improved reconstruction.
- **Through focus ptychography** [89]: It is a further extension of near-field ptychography with additional diversity in the diffraction pattern by translating the object in a longitudinal direction.

References

[1] V. Lučić, F. Förster, and W. Baumeister. Structural studies by electron tomography: From cells to molecules. *Annual Review of Biochemistry*, 74(1):833–865, 2005. PMID: 15952904.

[2] O. L. Krivanek, M. F. Chisholm, V. Nicolosi, T. J. Pennycook, G. J. Corbin, N. Dellby, M. F. Murfitt, C. S. Own, Z. S. Szilagyi, M. P. Oxley, S. T. Pantelides, and S. J. Pennycook. Atom-by-atom structural and chemical analysis by annular dark-field electron microscopy. *Nature*, 464(7288):571–574, 2010.

[3] J. Miao, P. Ercius, and S. J. L. Billinge. Atomic electron tomography: 3d structures without crystals. *Science*, 353(6306), 2016.

[4] C. A. Larabell and M. A. Le Gros. X-ray tomography generates 3-d reconstructions of the yeast, saccharomyces cerevisiae, at 60-nm resolution. *Molecular biology of the cell*, 15(3):957–962, 2004.

[5] H. Stoll, A. Puzic, B. Van Waeyenberge, P. Fischer, J. Raabe, M. Buess, T. Haug, R. Höllinger, C. Back, D. Weiss, and G. Denbeaux. High-resolution imaging of fast magnetization dynamics in magnetic nanostructures. *Applied Physics Letters*, 84(17):3328–3330, 2004.

[6] E. Spiller. *Encyclopedia of Optical Engineering*, volume 3. CRC Press Taylor & Francis Group, 2003.

[7] S. Bajt, M. Prasciolu, H. Fleckenstein, M. Domaracký, H. N. Chapman, A. J. Morgan, O. Yefanov, M. Messerschmidt, Y. Du, K. T. Murray, V. Mariani, M. Kuhn, S. Aplin, K. Pande, P. Villanueva-Perez, K. Stachnik, J. P. J. Chen, A. Andrejczuk, A. Meents, A. Burkhardt, D. Pennicard, X. Huang, H. Yan, E. Nazaretski, Y. S. Chu, and C. E. Hamm. X-ray focusing with efficient high-na multilayer laue lenses. *Light: Science & Applications*, 7:17162, March 2018.

[8] F. Döring, A. L. Robisch, C. Eberl, M. Osterhoff, A. Ruhlandt, T. Liese, F. Schlenkrich, S. Hoffmann, M. Bartels, T. Salditt, and H. U. Krebs. Sub-5 nm hard x-ray point focusing by a combined kirkpatrick-baez mirror and multilayer zone plate. *Optics Express*, 21(16):19311–19323, 2013.

[9] X. Huang, R. Conley, N. Bouet, J. Zhou, A. Macrander, J. Maser, H. Yan, E. Nazaretski, K. Lauer, R. Harder, I. K. Robinson, S. Kalbfleisch, and Y. S. Chu. Achieving hard x-ray nanofocusing using a wedged multilayer laue lens. *Optics Express*, 23(10):12496–12507, 2015.

[10] W. Chao, B. D. Harteneck, J. A. Liddle, E. H. Anderson, and D. T. Attwood. Soft x-ray microscopy at a spatial resolution better than 15 nm. *Nature*, 435:1210–1213, 2005.

[11] D. Gabor. A new microscopic principle. *Nature*, 161(4098):777–778, 1948.

[12] D. Gabor. Holography 1948–1971. *Proceedings of the IEEE*, 60(6):655–668, 1972.

[13] H. M. A. El-Sum. *Reconstructed wavefront microscopy*. PhD thesis, Stanford University, 1952.

[14] H. M. A. El-Sum and P. Kirkpatrick. Microscopy by reconstructed wavefronts. *Physical Review*, 85(763), 1952.

[15] A. V. Baez. A study in diffraction microscopy with special reference to x-rays. *Journal of the Optical Society of America*, 42(10):756–762, 1952.

[16] G. Kellström. Experimentelle untersuchungen über interferenz-und beugungserscheinungen bei langwelligen röntgenstrahlen. *Nova Acta Regiae Societatis Scientiarum Upsaliensis*, 8:1–66, 1932.

[17] D. Sayre. *Imaging processes and coherence in physics*. Springer, Berlin, 1980.

[18] D. Sayre, R.P. Haelbich, J. Kirz, and W.B. Yun. *X-ray Microscopy*, volume 43. Springer, 1984.

[19] W. B. Yun, J. Kirz, and D. Sayre. Observation of the soft x□ray diffraction pattern of a single diatom. *Acta Crystallographica Section A*, 43(1):131–133, 1987.

[20] D. Sayre and H. N. Chapman. X-ray microscopy. *Acta Crystallographica Section A*, 51(3):237–252, 1995.

[21] D. Sayre, H. N. Chapman, and J. Miao. On the extendibility of x-ray crystallography to noncrystals. *Acta Crystallographica Section A*, A54:232–239, 1998.

[22] R. H. T. Bates. Fourier phase problems are uniquely solvable in mute than one dimension. i: Underlying theory. *Optik*, 61(3):247–262, 1982.

[23] M. Hayes. The reconstruction of a multidimensional sequence from the phase or magnitude of its fourier transform. *IEEE Transaction on acoustics, speech and signal processing*, 30(2):140–154, 1982.

[24] J. Miao, D. Sayre, and H. N. Chapman. Phase retrieval from the magnitude of the fourier transforms of nonperiodic objects. *Journal of the Optical Society of America A*, 15(6):1662–1669, 1998.

[25] J. Miao, P. Charalambous, J. Kirz, and D. Sayre. Extending the methodology of x-ray crystallography to allow imaging of micrometre-sized non-crystalline specimens. *Nature*, 400:342–344, 1999.

[26] J. Miao, T. Ishikawa, B. Johnson, E. H. Anderson, B. Lai, and K. O. Hodgson. High resolution 3d x-ray diffraction microscopy. *Physical Review Letters*, 89(8), 2002.

[27] R. W. Gerchberg and W. O. Saxton. *Optik*, 35(237), 1972.

[28] J. R. Fienup. Phase retrieval algorithms: a comparison. *Applied optics*, 21(15):2758–2769, 1982.

[29] J. C. Dainty and J. R. Fienup. *Image Recovery: Theory and Application*, chapter Phase retrieval and image reconstruction for astronomy, pages 231–275. Academic Press, 1987.

[30] H. H. Bauschke, P. L. Combettes, and D. R. Luke. Hybrid projection–reflection method for phase retrieval. *Journal of the Optical Society of America A*, 20(6):1025–1034, 2003.

[31] D. R. Luke. Relaxed averaged alternating reflections for diffraction imaging. *Inverse Problems*, 21(1):37–50, 2004.

[32] H. N. Chapman, A. Barty, M. J. Bogan, S. Boutet, M. Frank, S. P. Hau-Riege, S. Marchesini, B. W. Woods, S. Bajt, W. H. Benner, R. A. London, E. Plönjes, M. Kuhlmann, R. Treusch, S. Düsterer, T. Tschentscher, J. R. Schneider, E. Spiller, T. Möller, C. Bostedt, M. Hoener, D. A. Shapiro, K. O. Hodgson, D. van der Spoel, F. Burmeister, M. Bergh, C. Caleman, G. Huldt, M. M. Seibert, F. R. N. C. Maia, R. W. Lee, A. Szöke, N. Timneanu, and J. Hajdu. Femtosecond diffractive imaging with a soft-x-ray free-electron laser. *Nature Physics*, 2:839–843, 2006.

[33] M. M. Seibert, T. Ekeberg, F. R. N. C. Maia, M. Svenda, J. Andreasson, O. Jönsson, D. Odić, B. Iwan, A. Rocker, D. Westphal, M. Hantke, D. P. DePonte, A. Barty, J. Schulz, L. Gumprecht, N. Coppola, A. Aquila, M. Liang, T. A. White, A. Martin, C. Caleman, S. Stern, C. Abergel, V. Seltzer, J.-M. Claverie, C. Bostedt, J. D. Bozek, S. Boutet, A. A. Miahnahri, M. Messerschmidt, J. Krzywinski, G. Williams, K. O. Hodgson, M. J. Bogan, C. Y. Hampton, R. G. Sierra, D. Starodub, I. Andersson, S. Bajt, M. Barthelmess, J. C. H. Spence, P. Fromme, U. Weierstall, R. Kirian, M. Hunter, R. B. Doak, S. Marchesini, S. P. Hau-Riege, M. Frank, R. L. Shoeman, L. Lomb, S. W. Epp, R. Hartmann, D. Rolles, A. Rudenko, C. Schmidt, L. Foucar, N. Kimmel, P. Holl, B. Rudek, B. Erk, A. Hömke, C. Reich, D. Pietschner, G. Weidenspointner, L. Strüder, G. Hauser, H. Gorke, J. Ullrich, I. Schlichting, S. Herrmann, G. Schaller, F. Schopper, H. Soltau, K.-U. Kühnel, R. Andritschke, C.-D. Schröter, F. Krasniqi, M. Bott, S. Schorb, D. Rupp, M. Adolph, T. Gorkhover, H. Hirsemann, G. Potdevin, H. Graafsma, B. Nilsson, H. N. Chapman, and J. Hajdu. Single mimivirus particles intercepted and imaged with an x-ray laser. *Nature*, 470:78–81, 2011.

[34] S. Witte, V. T. Tenner, D. W. Noom, and K. S. Eikema. Lensless diffractive imaging with ultra-broadband table-top sources: from infrared to extreme-ultraviolet wavelengths. *Light: Science and Applications*, 3, 2014.

[35] P. Almoro, G. Pedrini, and W. Osten. Complete wavefront reconstruction using sequential intensity measurements of a volume speckle field. *Applied Optics*, 45(34):8596–8605, 2006.

[36] J. M. Rodenburg. Ptychography and related diffractive imaging methods. *Advances in Imaging and Electron Physics*, 150:87–184, 2008.

[37] W. Hoppe. Beugung im inhomogenen primärstrahlwellenfeld. i. prinzip einer phasenmessung von elektronenbeugungsinterferenzen. *Acta Crystallographica Section A*, 25:495–501, 1969.

[38] R. Hegerl and W. Hoppe. Dynamische theorie der kristallstrukturanalyse durch elektronenbeugung im inhomogenen primärstrahlwellenfeld. *Berichte der Bunsengesellschaft für Physikalische Chemie*, 74(11), 1970.

[39] P. D. Nellist, B. C. McCallum, and J. M. Rodenburg. Resolution beyond the'information limit'in transmission electron microscopy. *Nature*, 374:630–632, 1995.

[40] J. M. Rodenburg and R. H. T. Bates. The theory of super-resolution electron microscopy via wigner-distribution deconvolution. *Philosophical Transactions of the Royal Society of London A: Mathematical, Physical and Engineering Sciences*, 339(1655):521–553, 1992.

[41] H. M. L. Faulkner and J. M. Rodenburg. Movable aperture lensless transmission microscopy: A novel phase retrieval algorithm. *Phys. Rev. Lett.*, 93(2), 2004.

[42] J. M. Rodenburg and H. M. L. Faulkner. A phase retrieval algorithm for shifting illumination. *Appl. Phys. Lett.*, 85(20), 2004.

[43] J. M. Rodenburg, A. C. Hurst, A. G. Cullis, B. R. Dobson, F. Pfeiffer, O. Bunk, C. David, K. Jefimovs, and I. Johnson. Hard-x-ray lensless imaging of extended objects. *Phys. Rev. Lett.*, 98(3):034801, 2007.

[44] J. M. Rodenburg, A. C. Hurst, and A. G. Cullis. Transmission microscopy without lenses for objects of unlimited size. *Ultramicroscopy*, 107:227–231, 2007.

[45] O. Bunk, M. Dierolf, S. Kynde, I. Johnson, O. Marti, and F. Pfeiffer. Influence of the overlap parameter on the convergence of the ptychographical iterative engine. *Ultramicroscopy*, 108:481–487, 2008.

[46] H. M. L. Faulkner and J. M. Rodenburg. Error tolerance of an iterative phase retrieval algorithm for moveable illumination microscopy. *Ultramicroscopy*, 103:153–164, 2005.

[47] P. Thibault, M. Dierolf, A. Menzel, O. Bunk, C. David, and F. Pfeiffer. High-resolution scanning x-ray diffraction microscopy. *Science*, 321:379–382, 2008.

[48] M. Guizar-Sicairos and J. R. Fienup. Phase retrieval with transverse translation diversity: a nonlinear optimization approach. *Optics Express*, 16(10):7264–7278, 2008.

[49] P. Thibault, M. Dierolf, O. Bunk, A. Menzel, and F. Pfeiffer. Probe retrieval in ptychographic coherent diffractive imaging. *Ultramicroscopy*, 109(4):338–343, 2009.

[50] A. M. Maiden and J. M. Rodenburg. An improved ptychographical phase retrieval algorithm for diffractive imaging. *Ultramicroscopy*, 109(10):1256–1262, 2009.

[51] K. Giewekemeyer, P. Thibault, S. Kalbfleisch, A. Beerlink, C. M. Kewish, M. Dierolf, F. Pfeiffer, and T. Salditt. Quantitative biological imaging by ptychographic x-ray diffraction microscopy. *Proceedings of the National Academy of Sciences*, 107(2):529–534, 2010.

[52] A. Schropp, P. Boye, J. M. Feldkamp, R. Hoppe, J. Patommel, D. Samberg, S. Stephan, K. Giewekemeyer, R. N. Wilke, T. Salditt, J. Gulden, A. P. Mancuso, I. A. Vartanyants, E. Weckert, S. Schöder, M. Burghammer, and C. G. Schroer. Hard x-ray nanobeam characterization by coherent diffraction microscopy. *Applied Physics Letters*, 96, 2010.

[53] C. M. Kewish, P. Thibault, M. Dierolf, O. Bunk, A. Menzel, J. Vila-Comamala, K. Jefimovs, and F. Pfeiffer. Ptychographic characterization of the wavefield in the focus of reflective hard x-ray optics. *Ultramicroscopy*, 110(4):325–329, 2010.

[54] M. Dierolf, A. T. P. Menzel, P. Schneider, C. M. Kewish, R. Wepf, O. Bunk, and F. Pfeiffer. Ptychographic x-ray computed tomography at the nanoscale. *Nature*, 467:436–439, 2010.

[55] K. Giewekemeyer, M. Beckers, T. Gorniak, M. Grunze, T. Salditt, and A. Rosenhahn. Ptychographic coherent x-ray diffractive imaging in the water window. *Optics Express*, 19(2):1037–1050, 2011.

[56] M. Beckers, T. Senkbeil, T. Gorniak, M. Reese, K. Giewekemeyer, S. Gleber, T. Salditt, and A. Rosenhahn. Chemical contrast in soft x-ray ptychography. *Physical Review Letters*, 107, 2011.

[57] M. Guizar-Sicairos, A. Diaz, M. Holler, M. S. Lucas, A. Menzel, R. A. Wepf, and O. Bunk. Phase tomography from x-ray coherent diffractive imaging projections. *Optics Express*, 19:21345–21357, 2011.

[58] G. R. Brady, M. Guizar-Sicairos, and J. R. Fienup. Optical wavefront measurement using phase retrieval with transverse translation diversity. *Optics Express*, 17(2):624–639, 2009.

[59] A. M. Maiden, J. M. Rodenburg, and M. J. Humphry. Optical ptychography: a practical implementation with useful resolution. *Optics Letters*, 35(15):2585–2587, 2010.

[60] A. M. Maiden, M. J. Humphry, F. Zhang, and J. M. Rodenburg. Superresolution imaging via ptychography. *Journal of the Optical Society of America A*, 28(4):604–612, 2011.

[61] F. Hüe, J. M. Rodenburg, A. M. Maiden, F. Sweeney, and P. A. Midgley. Wavefront phase retrieval in transmission electron microscopy via ptychography. *Physical Review B*, 82(12), 2010.

[62] C. T. Putkunz, A. J. D'Alfonso, A. J. Morgan, M. Weyland, C. Dwyer, L. Bourgeois, J. Etheridge, A. Roberts, R. E. Scholten, K. A. Nugent, and L. J. Allen. Atom-scale ptychographic electron diffractive imaging of boron nitride cones. *Physical Review Letters*, 108, 2012.

[63] M. J. Humphry, B. Kraus, A. C. Hurst, A. M. Maiden, and J. M. Rodenburg. Ptychographic electron microscopy using high-angle dark-field scattering for sub-nanometre resolution imaging. *Nature Communications*, 3, 2012.

[64] P. Wang, F. Zhang, S. Gao, M. Zhang, and A. I. Kirkland. Electron ptychographic diffractive imaging of boron atoms in lab_6 crystals. *Scientific Reports*, 7(2857), 2017.

[65] A. Schropp, P. Boye, A. Goldschmidt, S. Hönig, R. Hoppe, J. Patommel, C. Rakete, D. Samberg, S. Stephan, S. Schöder, M. Burghammer, and C. G. Schroer. Non-destructive and quantitative imaging of a nano-structured microchip by ptychographic hard x-ray scanning microscopy. *Journal of Microscopy*, 241(1):9–13, 2010.

[66] Y. Takahashi, A. Suzuki, N. Zettsu, Y. Kohmura, Y. Senba, H. Ohashi, K. Yamauchi, and T. Ishikawa. Towards high-resolution ptychographic x-ray diffraction microscopy. *Physical Review B*, 83, 2011.

[67] F. Hüe, J. M. Rodenburg, A. M. Maiden, and P. A. Midgley. Extended ptychography in the transmission electron microscope: possibilities and limitations. *Ultramicroscopy*, 111(8):1117–1123, 2011.

[68] M. Beckers, T. Senkbeil, T. Gorniak, K. Giewekemeyer, T. Salditt, and A. Rosenhahn. Drift correction in ptychographic diffractive imaging. *Ultramicroscopy*, 126:44–47, 2013.

[69] A. Shenfield and J. M. Rodenburg. Evolutionary determination of experimental parameters for ptychographical imaging. *Journal of Applied Physics*, 109, 2011.

[70] A. M. Maiden, M. J. Humphry, M. C. Sarahan, B. Kraus, and J. M. Rodenburg. An annealing algorithm to correct positioning errors in ptychography. *Ultramicroscopy*, 120:64–72, 2012.

[71] F. Zhang, I. Peterson, J. Vila-Comamala, A. Diaz, F. Berenguer, R. Bean, B. Chen, A. Menzel, I. K. Robinson, and J. M. Rodenburg. Translation position determination in ptychographic coherent diffraction imaging. *Optics Express*, 21(11):13592–13606, 2013.

[72] A. Tripathi, I. McNulty, and O. G. Shpyrko. Ptychographic overlap constraint errors and the limits of their numerical recovery using conjugate gradient descent methods. *Optics Express*, 22(2):1452–1466, 2014.

[73] G. Zheng, R. Horstmeyer, and C. Yang. Wide-field, high-resolution fourier ptychographic microscopy. *Nature Photonics*, 7:739–745, 2013.

[74] A. W. Lohmann, R. G. Dorsch, D. Mendlovic, Z. Zalevsky, and C. Ferreira. Space–bandwidth product of optical signals and systems. *Journal of the Optical Society of America A*, 13(3):470–473, 1996.

[75] W. Lukosz. Optical systems with resolving powers exceeding the classical limit. *Journal of the Optical Society of America*, 56(11):1463–1471, 1966.

[76] W. Lukosz. Optical systems with resolving powers exceeding the classical limit. ii. *Journal of the Optical Society of America*, 57(7):932–941, 1967.

[77] T. B. Edo, D. J. Batey, A. M. Maiden, C. Rau, U. Wagner, Z. D. Pešić, T. A. Waigh, and J. M. Rodenburg. Sampling in x-ray ptychography. *Phys. Rev. A*, 87, 2013.

[78] L. W. Whitehead, G. J. Williams, H. M. Quiney, D. J. Vine, R. A. Dilanian, S. Flewett, K. A. Nugent, A. G. Peele, E. Balaur, and I. McNulty. Diffractive imaging using partially coherent x rays. *Phys. Rev. Lett.*, 103(24):243902, 2009.

[79] P. Thibault and A. Menzel. Reconstructing state mixtures from diffraction measurements. *Nature*, 494(7435):68–71, 2013.

[80] A. M. Maiden, M. J. Humphry, and J. M. Rodenburg. Ptychographic transmission microscopy in three dimensions using a multi-slice approach. *J. Opt. Soc. Am. A*, 29(8):1606–1614, 2012.

[81] P. Ferrand, M. Allain, and V. Chamard. Ptychography in anisotropic media. *Optics Letters*, 40(22):5144–5147, 2015.

[82] P. Sidorenko and O. Cohen. Single-shot ptychography. *Optica*, 3(1):9–14, 2016.

[83] M. A. Pfeifer, G. J. Williams, I. A. Vartanyants, R. Harder, and I. K. Robinson. Three-dimensional mapping of a deformation field inside a nanocrystal. *Nature*, 442:63–66, 2006.

[84] P. Godard, G. Carbone, M. Allain, F. Mastropietro, G. Chen, L. Capello, A. Diaz, T. H. Metzger, J. Stangl, and V. Chamard. Three-dimensional high-resolution quantitative microscopy of extended crystals. *Nature Communications*, 2(568), 2011.

[85] V. Chamard, M. Allain, P. Godard, A. Talneau, G. Patriarche, and M. Burghammer. Strain in a silicon-on-insulator nanostructure revealed by 3d x-ray bragg ptychography. *Scientific Reports*, 5(9827), 2015.

[86] S. O. Hruszkewycz, M. Allain, M. V. Holt, C. E. Murray, J. R. Holt, P. H. Fuoss, and V. Chamard. High-resolution three-dimensional structural microscopy by single-angle bragg ptychography. *Nature Materials*, 16:244–251, 2017.

[87] D. J. Vine, G. J. Williams, B. Abbey, M. A. Pfeifer, J. N. Clark, M. D. de Jonge, I. McNulty, A. G. Peele, and K. A. Nugent. Ptychographic fresnel coherent diffractive imaging. *Phys. Rev. A*, 80(6), 2009.

[88] M. Stockmar, P. Cloetens, I. Zanette, B. Enders, M. Dierolf, F. Pfeiffer, and P. Thibault. Near-field ptychography: phase retrieval for inline holography using a structured illumination. *Scientific Reports*, 3, 2013.

[89] A.-L. Robisch, K. Kröger, A. Rack, and T. Salditt. Near-field ptychography using lateral and longitudinal shifts. *New J. Phys.*, 17, 2015.

3

Lateral position correction using intensity gradient method

Ptychography, a form of Coherent Diffractive Imaging, is used with short wavelengths (e.g. X-rays, electron beams) to achieve high-resolution image reconstructions. One of the limiting factors for the reconstruction quality is the accurate knowledge of the illumination probe positions. Recently, many advances have been made to relax the requirement for the probe positions accuracy. Here, we analyze and demonstrate a straightforward approach that can be used to correct the probe positions with sub-pixel accuracy. Simulations and experimental results with visible light are presented in this work.

Part of this chapter is published in Ultramicroscopy, **192**, pp. 29–36 (2018) [1].

3.1. Introduction

Coherent Diffractive Imaging (CDI) is a lensless imaging technique which uses far-field diffraction intensity patterns to reconstruct the image of an object. Ptychography is a form of CDI, where multiple far-field diffraction patterns corresponding to overlapping illuminated regions of the object are collected, and the object is reconstructed [2]. For the reconstruction of the object, the Ptychographical Iterative Engine (PIE) [3] is used of which many different variants have been developed [4–7]. PIE is robust if the a priori information such as the illumination probe function and the lateral probe positions are accurately known [8]. Several methods exist which can overcome the requirement for the accuracy of the a priori information. For example, Extended PIE (ePIE) can reconstruct the object as well as a poorly defined probe function [4]. However, ePIE is sensitive to the probe positioning errors, especially in applications involving short wavelengths such as X-rays and electron beams [9]. For these short wavelengths, the required accuracy in the probe positions should be in some cases of the order of 50 pm [10]. Since this is difficult to achieve experimentally, some new developments in the probe position corrections have been made.

The non-linear (NL) optimization approach was the first method that has been used to correct the probe positions [11]. However, this approach can easily lead to local minima which can be far from the required global minimum since several parameters (update of the object, the probe function and the probe positions) are used in the NL optimization routine. Improvements have been made in the NL optimization approach by combining it with ePIE and difference map (DM) [12]. In this reference, the authors have used the ePIE and DM to update the object and the probe function, whereas the probe positions have been corrected using the NL optimization. One drawback of this method is that the probe positions cannot be corrected to sub-pixel accuracy. Other methods based on the genetic algorithm and a drift-based model were also explored [13, 14]. In yet another study, the "annealing approach" "based on trial and error" was used, but at the cost of being computationally expensive [15]. Finally, there is a successful method that uses the cross-correlation between two consecutive object estimates for each probe position [10]. This approach has corrected the probe positions to sub-pixel accuracy using the additional sub-pixel registration method [16].

Here, we analyse and demonstrate an alternative algorithm to correct the probe positions with sub-pixel accuracy that is quite straightforward to implement [17]. This chapter is organized as follows: In Section 3.2 we describe our method for the probe position correction. In Section 3.3 we present results of simulations without and with noise. In Section 3.4, we show the experimental results. Finally, in Section 3.5, we present the conclusions.

3.2. The algorithm

In ptychography, the diffraction intensities $I^j(\mathbf{u})$ for different probe positions j = 1,2,...,J with respect to the object are recorded in the camera. Here, J is the number of diffraction patterns. If the object and illumination probe functions are repre-

sented as $O(\mathbf{r})$ and $P(\mathbf{r})$, then

$$I^j(\mathbf{u}) = |\mathfrak{F}\{O(\mathbf{r})P(\mathbf{r}-\mathbf{R}^j)\}(\mathbf{u})|^2, \tag{3.1}$$

where $\mathbf{R}^j = (X^j, Y^j)$ is the probe position vector, $\mathbf{r}$ and $\mathbf{u}$ represent the coordinate vector in the real and reciprocal space respectively, and $\mathfrak{F}$ denotes the Fourier transform. We combine the well-known phase reconstruction method ePIE with our position correction method. That means, for the k^{th} iteration and the j^{th} probe position, we update the object $O_k(\mathbf{r})$ to $O_{k+1}(\mathbf{r})$ and the probe function $P_k(\mathbf{r})$ to $P_{k+1}(\mathbf{r})$ using the ePIE after which the probe position $\mathbf{R}_k^j$ is updated using our probe position correction method. We describe the probe position correction method below. Note that in this probe position correction method, we use the previous estimates $O_k(\mathbf{r})$ and $P_k(\mathbf{r})$ instead of $O_{k+1}(\mathbf{r})$ and $P_{k+1}(\mathbf{r})$ as this saves one extra Fourier transform to perform. The reason will be clear soon.

For the k^{th} iteration, the diffracted far field for the probe position $\mathbf{R}_k^j$ can be written as

$$\Psi_k^j(\mathbf{u}) = \mathfrak{F}\{O_k(\mathbf{r})P_k(\mathbf{r}-\mathbf{R}_k^j)\}, \tag{3.2}$$

and the estimated intensity is

$$I_k^j(\mathbf{u}) = |\Psi_k^j(\mathbf{u})|^2. \tag{3.3}$$

For the object estimate $O_k(\mathbf{r})$ and probe estimate $P_k(\mathbf{r})$, the inaccuracy in the measurement intensity due to the error $(\Delta X_k^j, \Delta Y_k^j)$ in the probe position is given by:

$$\Delta I_k^j \approx \frac{\partial I_k^j}{\partial X_k^j}\Delta X_k^j + \frac{\partial I_k^j}{\partial Y_k^j}\Delta Y_k^j. \tag{3.4}$$

Here, $\frac{\partial I_k^j}{\partial X_k^j}$ and $\frac{\partial I_k^j}{\partial Y_k^j}$ are the derivatives of the estimated intensity with respect to the probe position along the x and y directions. We solve Eq. (3.4) for ΔX_k^j and ΔY_k^j where ΔI_k^j is assigned to $I^j - I_k^j$. To calculate $\frac{\partial I_k^j}{\partial X_k^j}$ and $\frac{\partial I_k^j}{\partial Y_k^j}$, we have

$$\frac{\partial I_k^j}{\partial X_k^j} = 2Re\left\{\frac{\partial \Psi_k^j}{\partial X_k^j}\Psi_k^{j*}\right\}, \tag{3.5a}$$

$$\frac{\partial I_k^j}{\partial Y_k^j} = 2Re\left\{\frac{\partial \Psi_k^j}{\partial Y_k^j}\Psi_k^{j*}\right\}, \tag{3.5b}$$

and

$$\frac{\partial \Psi_k^j(\mathbf{u})}{\partial X_k^j} = \mathfrak{F}\left\{O_k(\mathbf{r})\frac{\partial P_k(\mathbf{r}-\mathbf{R}_k^j)}{\partial X_k^j}\right\}(\mathbf{u}), \tag{3.6a}$$

$$\frac{\partial \Psi_k^j(\mathbf{u})}{\partial Y_k^j} = \mathfrak{F}\left\{O_k(\mathbf{r})\frac{\partial P_k(\mathbf{r}-\mathbf{R}_k^j)}{\partial Y_k^j}\right\}(\mathbf{u}). \tag{3.6b}$$

We approximate the right hand side of the Eq. (3.6) as

$$\frac{\partial \Psi_k^j}{\partial X_k^j} = \frac{\Psi_k^j - \mathfrak{F}\{O_k(\mathbf{r})P_k(\mathbf{r} - (\mathbf{R}_k^j + \mathbf{1}_x))\}}{|\mathbf{1}_x|}, \tag{3.7a}$$

$$\frac{\partial \Psi_k^j}{\partial Y_k^j} = \frac{\Psi_k^j - \mathfrak{F}\{O_k(\mathbf{r})P_k(\mathbf{r} - (\mathbf{R}_k^j + \mathbf{1}_y))\}}{|\mathbf{1}_y|}, \tag{3.7b}$$

where $\mathbf{1}_x$ and $\mathbf{1}_y$ are the vectors along the x and y directions and the magnitudes are the lengths of a pixel along the x and y directions, respectively. The following steps are performed to calculate the error and update the probe positions.

1. Calculate the difference ΔI_k^j between the measured intensity I^j and the estimated intensity I_k^j given by $\Delta I_k^j = I^j - I_k^j$.
2. Calculate $\frac{\partial \Psi_k^j}{\partial X_k^j}$ and $\frac{\partial \Psi_k^j}{\partial Y_k^j}$ using Eq. (3.7).
3. Calculate $\frac{\partial I_k^j}{\partial X_k^j}$ and $\frac{\partial I_k^j}{\partial Y_k^j}$ using Eq. (3.5).

Note that in Eq. (3.4), ΔI_k^j, $\frac{\partial I_k^j}{\partial X_k^j}$, and $\frac{\partial I_k^j}{\partial Y_k^j}$ are vectors whose components correspond to the values at the pixels. Given an intensity measurement consisting of N pixels, we can thus rewrite Eq. (3.4) as a matrix equation

$$\begin{bmatrix} \Delta I_k^j(1) \\ \Delta I_k^j(2) \\ \vdots \\ \Delta I_k^j(N) \end{bmatrix} = \begin{bmatrix} \frac{\partial I_k^j}{\partial X_k^j}(1) & \frac{\partial I_k^j}{\partial Y_k^j}(1) \\ \frac{\partial I_k^j}{\partial X_k^j}(2) & \frac{\partial I_k^j}{\partial Y_k^j}(2) \\ \vdots & \\ \frac{\partial I_k^j}{\partial X_k^j}(N) & \frac{\partial I_k^j}{\partial Y_k^j}(N) \end{bmatrix} \begin{bmatrix} \Delta X_k^j \\ \Delta Y_k^j \end{bmatrix}. \tag{3.8}$$

From this equation, we want to find $(\Delta X_k^j, \Delta Y_k^j)$. Because there are more equations than variables, there may be no solution $(\Delta X_k^j, \Delta Y_k^j)$ to this equation. Therefore, we calculate the least-squares solution which is given by

$$\begin{bmatrix} \Delta X_k^j \\ \Delta Y_k^j \end{bmatrix} = (A_k^{jT} A_k^j)^{-1} A_k^{jT} \begin{bmatrix} \Delta I_k^j(1) \\ \Delta I_k^j(2) \\ \vdots \\ \Delta I_k^j(N) \end{bmatrix}, \tag{3.9}$$

where

$$A_k^j = \begin{bmatrix} \frac{\partial I_k^j}{\partial x_k^j}(1) & \frac{\partial I_k^j}{\partial Y_k^j}(1) \\ \frac{\partial I_k^j}{\partial x_k^j}(2) & \frac{\partial I_k^j}{\partial Y_k^j}(2) \\ \vdots & \\ \frac{\partial I_k^j}{\partial x_k^j}(N) & \frac{\partial I_k^j}{\partial Y_k^j}(N) \end{bmatrix}, \tag{3.10}$$

and A_k^{jT} is the transpose of A_k^j. Note that $A_k^{jT} A_k^j$ is a 2×2 matrix, so that the computation of its inversion is computationally inexpensive. Finally, the update equation for the probe position (X_k^j, Y_k^j) is given by

$$X_{k+1}^j = X_k^j - \beta \Delta X_k^j, \tag{3.11}$$

$$Y_{k+1}^j = Y_k^j - \beta \Delta Y_k^j. \tag{3.12}$$

Here, β is a feedback parameter which defines the step size of the update in the probe positions. The feedback parameter β depends upon the retrieved shift error in the probe position. For this algorithm, the shift errors are in the order of a pixel, therefore we choose the β as 1, 0.5, 0.1. Choosing smaller β in general leads to accurate correction but the computation time will be longer.

On comparing the computational time of our approach with the cross-correlation (CC) method [10], we have found that each iteration of our method is less computationally expensive than the CC method. Here, in the probe position correction part, we are using two Fourier transforms whereas the CC method uses three Fourier transforms. Additionally, the CC method requires optimization in each iteration to find the cross-correlation peak. Furthermore, in Section 3.3.4, we have carried out an actual comparison between the CC method and the proposed method.

3.3. Simulations

3.3.1. Simulations on the general performance of the algorithm

We denote the wavelength of the light by λ, the detector pixel size by $\Delta x_d = \Delta y_d$, the distance between the object and the detector by z. The detector has N pixels and the number of pixels in the x and y directions are the same, i.e. both are $\sqrt{N}$. If the detector pixel size is Δx_d, the pixel size in the Fourier space is $\Delta f = \frac{k \Delta x_d}{z}$. The pixel size in the real space (i.e. the object space) Δx_o can be found by using the relation $\Delta x_o \Delta f = \frac{2\pi}{\sqrt{N}}$. Thus, $\Delta x_o = \frac{\lambda z}{\sqrt{N} \Delta x_d}$.

We used a circular illumination probe which was formed by propagating a uniformly illuminated circular pinhole function with a diameter of $89.6 \Delta x_o$. We have used a gray probe which means that a pixel can have a non-integer value between 0 and 1; consequently, the diameter of the probe is represented with sub-pixel accuracy. The propagation distance z' is chosen such that $\lambda z' = 5 \times 10^{-4} \text{mm}^2$. The size of the scanned object is $224 \Delta x_o \times 224 \Delta x_o$. The probe positions were formed using a grid of 8×8. The grid interval was $19.2 \Delta x_o$, and the overlap between the adjacent probes was 73%. Random offsets with a maximum value of $10 \Delta x_o$, were

added to each probe position in both x and y directions. These generated probe positions were used to form the far-field intensity patterns. The feedback parameter β was chosen to be 0.5.

'Cameraman' was used as the amplitude of the test object which varies between $[0, 1]$. 'Lenna' was used as the phase of the test object with values between $[-0.7\pi, 0.7\pi]$. In our simulation, the probe position update starts at 15^{th} iterations and probe function update starts at 45^{th} iterations. The reasoning for these numbers comes from the observation in Ref. [10] that probe positions are less affected by the inaccurate probe function. While, the probe function is severely affected by inaccurate probe positions. Therefore, we started the probe function update when the probe positions were close to the correct value. Therefore, we chose these numbers where the error starts to stagnate. The simulation ran for 300 iterations. Figs. 3.1(a-d) show the object and probe functions which were used to generate the simulated diffraction patterns. Figs. 3.1(e-h) show the reconstruction of the object and probe functions using the ePIE when the error in the probe positions was present. Figs. 3.1(i-l) show the reconstruction of the object and probe when our approach to correct the probe positions together with the ePIE was used. Note that the contours of the object amplitude are visible in the reference phase (Fig. 3.1(c)) and reconstructed phase (Fig. 3.1(k)). These are due to the presence of zero amplitude in the object.

In Fig. 3.2, we map the updates of the probe positions as they converge from the initial guessed positions to the actual probe positions. The green dots represent the actual probe positions which were used to generate the intensity patterns in the far-field, the red dots are the initial guesses for the probe positions, and the blue dots indicate the trajectory of the convergence. Note that almost all initially guessed positions converge to the actual positions. In Fig. 3.3, the plot for diffraction error versus iteration is shown. The error metric for each iteration is defined as

$$\mathcal{E}^j = \sum_{\mathbf{u}} \left\{ |\Psi_k^j(\mathbf{u})| - \sqrt{I^j(\mathbf{u})} \right\}^2 . \tag{3.13}$$

Fig. 3.3 shows the mean of $\mathcal{E}^j$ over all the probe positions for each iteration.

3.3.2. Simulations in the presence of noise

The algorithm was also tested in the presence of Poisson noise. We performed simulations with different numbers of photons per diffraction pattern. The simulation for each noise level was run for ten times with different random initial offsets taken from [-10,10] pixels along the x and y directions. The other parameters of the object and probe functions were the same as in Section 3.3.1. In Fig. 3.4, the solid lines represent the mean value whereas the patches show the standard deviation. If $\sigma(Z)$ is a 2-D standard deviation of a 2-D matrix Z, then the mean error is calculated as follows:

$$E_k = \sqrt{\left\{\sigma(X^j - X_k^j)\right\}^2 + \left\{\sigma(Y^j - Y_k^j)\right\}^2}. \tag{3.14}$$

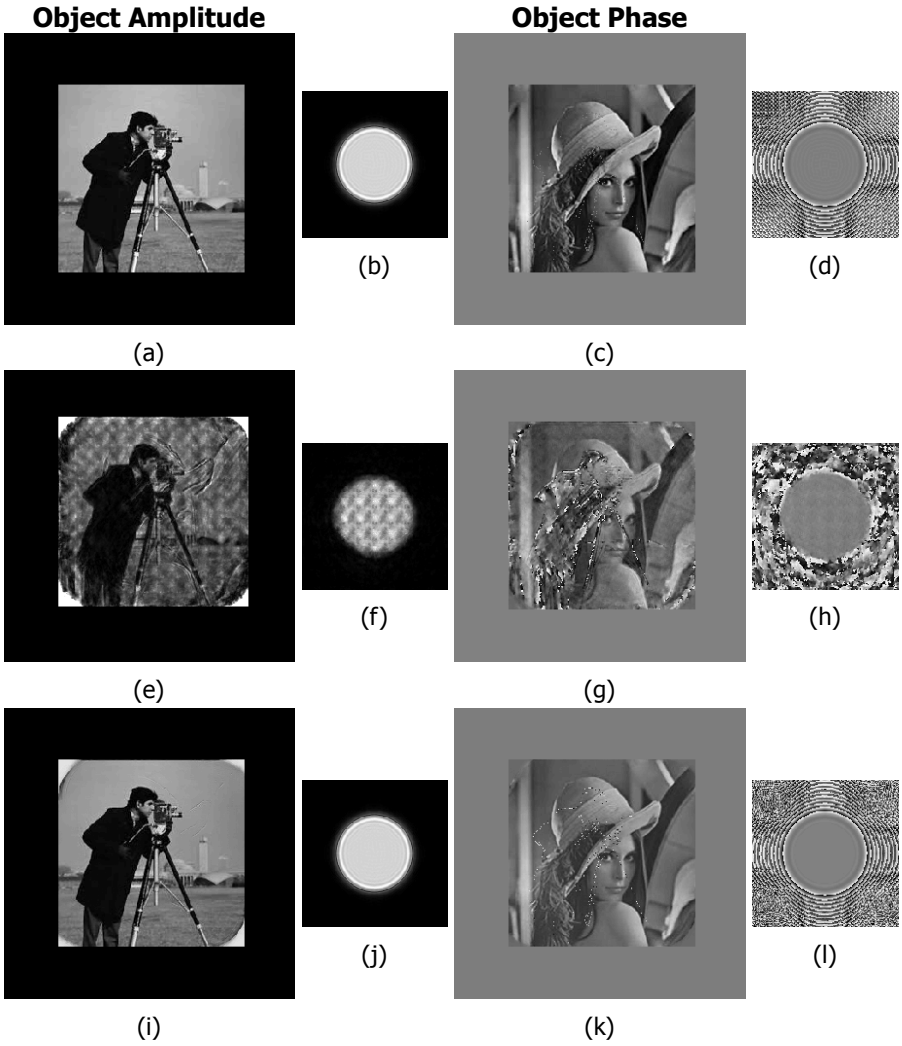

Figure 3.1: Reconstruction of the object and probe after 300 iterations. (a)-(d) are the test object and probe functions (Figs. (b) and (d)), which were used to generate the diffraction intensity patterns. The object amplitude varies between [0,1], and the object phase ranges from [-0.7π,0.7π]. (e)-(h) are the reconstructed images using the ePIE. (i)-(l) are the reconstructed images using the ePIE together with the probe positions correction. For these simulations, 8×8 probe positions with an overlap of 73% have been used.

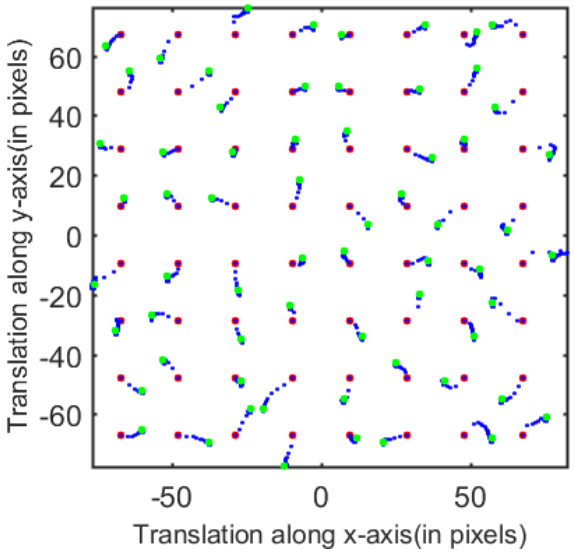

Figure 3.2: Probe position correction map. Here, the maximum random added offset to each probe position is $10\Delta x_o$. The red dots are the initial guess for the probe positions, the green dots are the actual probe positions, and the blue dots show how the estimated probe positions change over iterations.

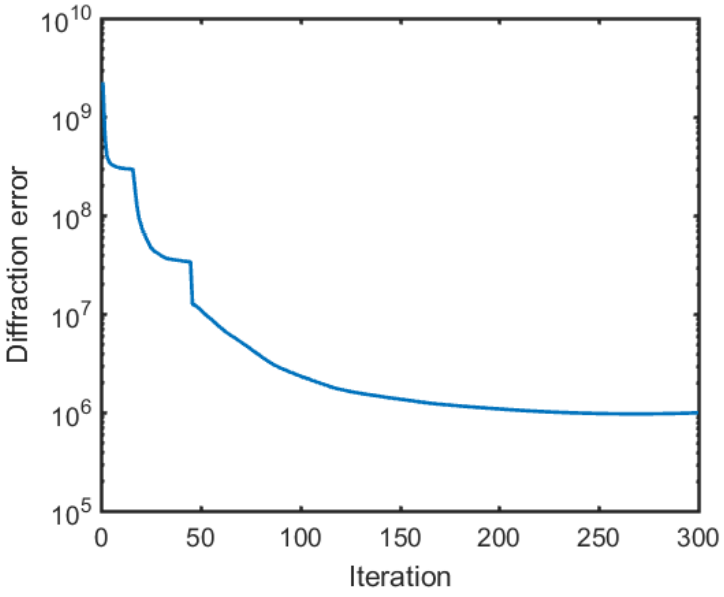

Figure 3.3: Plot for diffraction error versus iteration. The diffraction errors for each probe position is calculated using Eq. (3.13). The plot is mean of diffraction error for all the probe positions versus iteration.

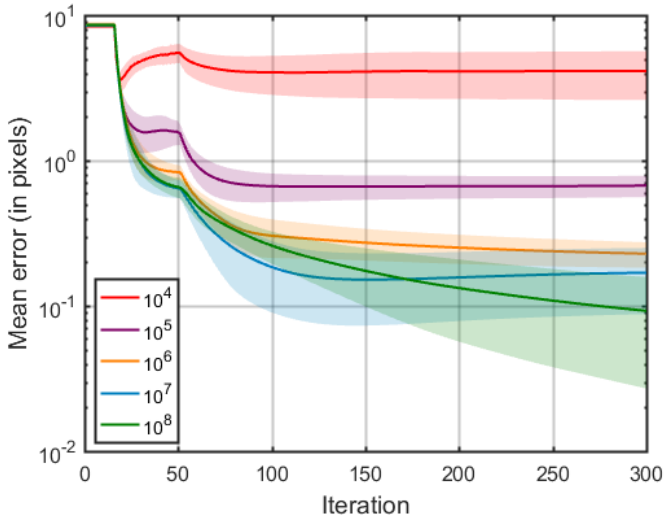

Figure 3.4: Mean error in the probe position in the presence of Poisson noise. The solid lines represent the mean value, whereas the patches show the standard deviation. For each noise level (varying from 10^8 to 10^4 photons per diffraction pattern), ten simulations were made where different random initial offsets are used to generate the actual probe positions.

Even with approximately 10^5 photons per diffraction pattern, the mean error in the retrieved probe positions was less than one pixel, and the mean error for the case of 10^8 photons was the order of 10^{-2} pixel.

3.3.3. Effect of overlap and initial position error

In Fig.3.5, the performance of the algorithm for different overlaps and different introduced initial position errors have been shown. For each overlap and maximum introduced initial position error, ten simulations were performed with different random initial offsets. The solid lines represent the mean value whereas the patches show the standard deviation. 6×6 probe positions have been used for the results shown here. Since the final error is gradually increasing as the initially introduced maximum error is increasing, it is difficult to comment on the maximum initial error this method can correct for this case. There is also no specific point where a sharp increase in the error can be seen. Similar behaviour is also observed in the Ref. [12]. From Fig. 3.5, the correction of the probe positions is not strongly dependent on the overlap. However, 75% overlap may be considered as an optimum overlap for this case.

3.3.4. Comparison with cross-correlation method

It was previously noted that an iteration of the proposed method is less computationally expensive than an iteration of the cross-correlation (CC) method. However, this does not necessarily mean that the proposed method is less computationally

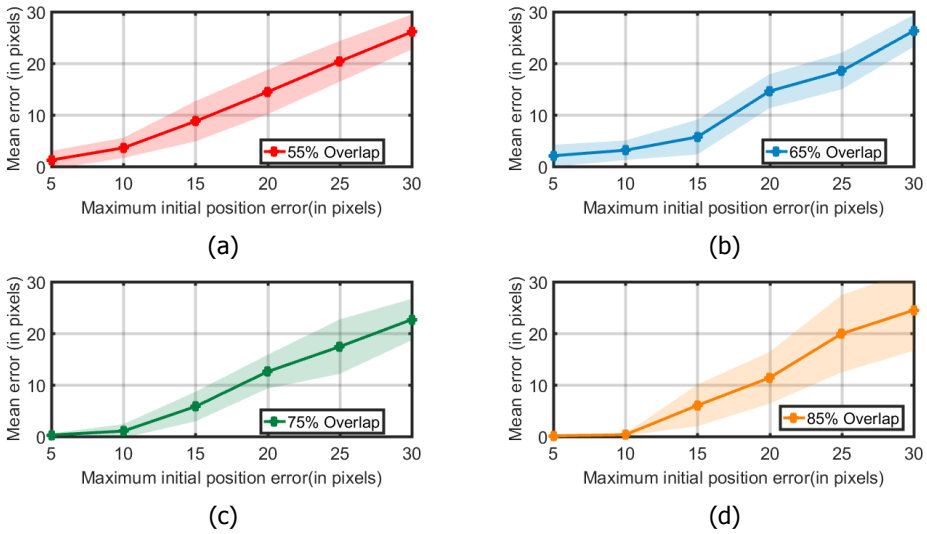

Figure 3.5: Results for varying overlaps and initial position errors versus mean error in the probe position. For each overlap and introduced maximum initial position error, ten simulations were performed with different random initial offsets. Here, the solid lines represent the mean value of the final position error of the ten simulations, whereas the patches show the standard deviation.

expensive on the overall because in principle it could require more iterations to obtain the same reconstruction error. Therefore, we compare the two methods to see if indeed the proposed method is less computationally expensive than the CC method. Here, we have performed ten simulations for each method where the parameters are the same as given in the simulation section, and the random initial offsets for probe positions were taken from $[-10, 10]$ pixels. In Fig. 3.6(a), we have encountered the small bumps in the simulation which are due to the implementation of automatic adapting feedback parameter as explained in the Ref. [10]. Here, threshold parameters for the automatic feedback parameters are -0.2 and 0.45. In Fig. 3.6(b), simulations for the proposed method is shown where the feedback parameter is 1. The final mean error of these ten simulations after 300 iterations for the CC method and the proposed method are 0.013 and 0.023 pixels respectively. From here, we conclude that even though, initially, the CC method converges faster than the proposed method, both methods achieve comparable accuracy once they converge.

3.4. Experiment

To demonstrate the algorithm to correct the probe positions, we built an experimental setup as shown in Fig. 3.7. The beam of a HeNe laser (633 nm wavelength) is first expanded and collimated by two lenses and used to illuminate the phase-only Spatial light modulator (Holoeye Pluto, 1920 $\times$ 1080 pixels, 8.0 μm pixel pitch). In the SLM, a phase pattern is created (Lenna, with the phase varying from 0 to

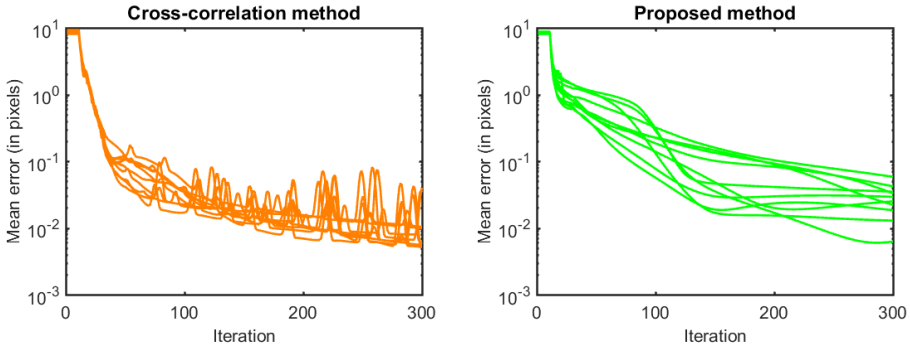

Figure 3.6: Comparison between the cross-correlation method and proposed method. For each method, ten simulations were performed where the random initial offsets were used to generate the actual probe positions. (a) Mean error in the probe position versus iteration for the cross-correlation method. (b) Mean error in the probe position versus iteration for the proposed method.

1.8 π) together with an added phase ramp to shift the non-modulated from the modulated signals at the diffraction plane [18]. The created phase pattern on the SLM is the assigned image that we want to reconstruct. The illumination probe was created by adding a rapidly phase changing pattern (Fig. 3.8(c)) with SLM on top of the object. The far-field was obtained by using a 15 cm focal length lens placed at 15 cm from the SLM. The CCD camera (8 bit, pixel size 4.65 μm^2) was placed at the back focal plane of the lens to collect the ptychographic data set. On the SLM, the object had 800 $\times$ 800 pixels, and it was illuminated by a circle of radius of 250 pixels. The object was shifted to 7 $\times$7 positions with an interval of 50 pixels which is equivalent to shift the probe in reverse order. Due to magnification, the added random offset in the simulation of $5\Delta x_o$ is equivalent to 20.83 pixels on SLM.

In Figs. 3.8–3.9, a comparison has been shown between the ePIE and ePIE with our probe position correction method for different added random offsets to the probe positions. Maximum random offsets added to the probe positions in the simulation were $2\Delta x_o$ and $10\Delta x_o$ respectively. In Fig. 3.10, the scatter plot is shown when the maximum initial random offset was $2\Delta x_o$. Fig. 3.10(a) shows the actual probe positions (green) and initial guessed probe positions (red) whereas Fig. 3.10(b) shows the actual probe positions (green) and the final reconstructed probe positions (red). Note that the final reconstructed probe positions shown here are translated by a constant. In Fig. 3.11(a), the plot for diffraction error versus introduced maximum initial position error is shown. The diffraction error is calculated using Eq. (3.13). To show what it means to have a diffraction error of 10^6, in Fig. 3.11(b), the estimated amplitude, measured amplitude, and its difference is shown for the probe position (1,1).

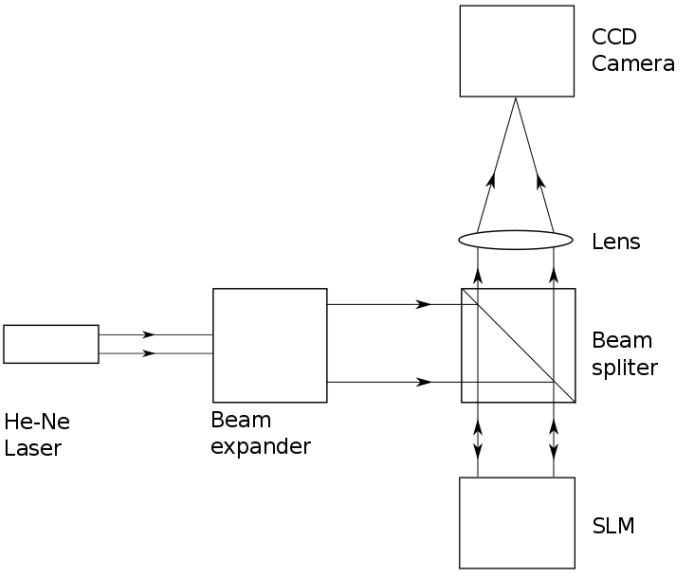

Figure 3.7: Experimental set-up. The set-up consists of He-Ne Laser (633 nm wavelength), beam expander, beam splitter, lens (f = 15cm), SLM (Holoeye Pluto, 1920×1080 pixels, 8.0 μm pixel pitch), and CCD Camera (8 bit, pixel size 4.65 μm^2).

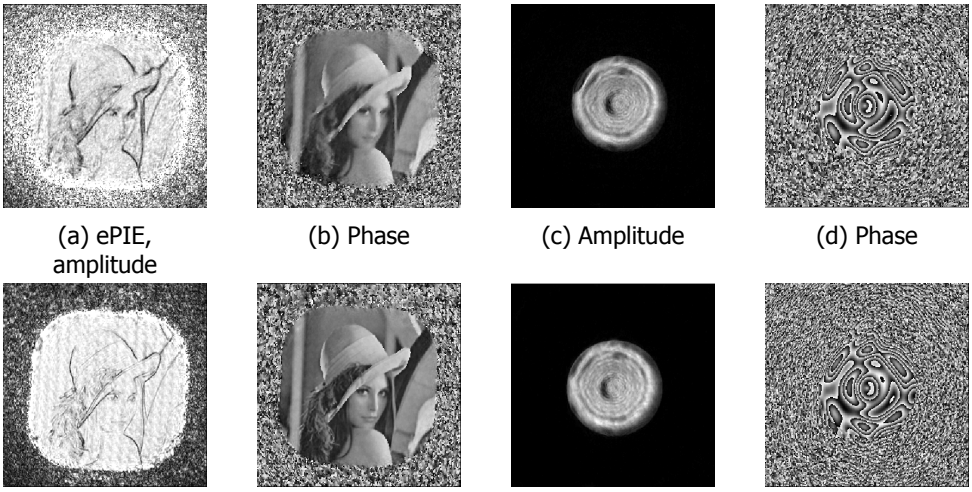

(a) ePIE, amplitude | (b) Phase | (c) Amplitude | (d) Phase

(e) ePIE with positions correction, amplitude | (f) Phase | (g) Amplitude | (h) Phase

Figure 3.8: Maximum random added offset to each probe position = $2\Delta x_o$. We have truncated the color scale for the object amplitude to make certain features more visible.

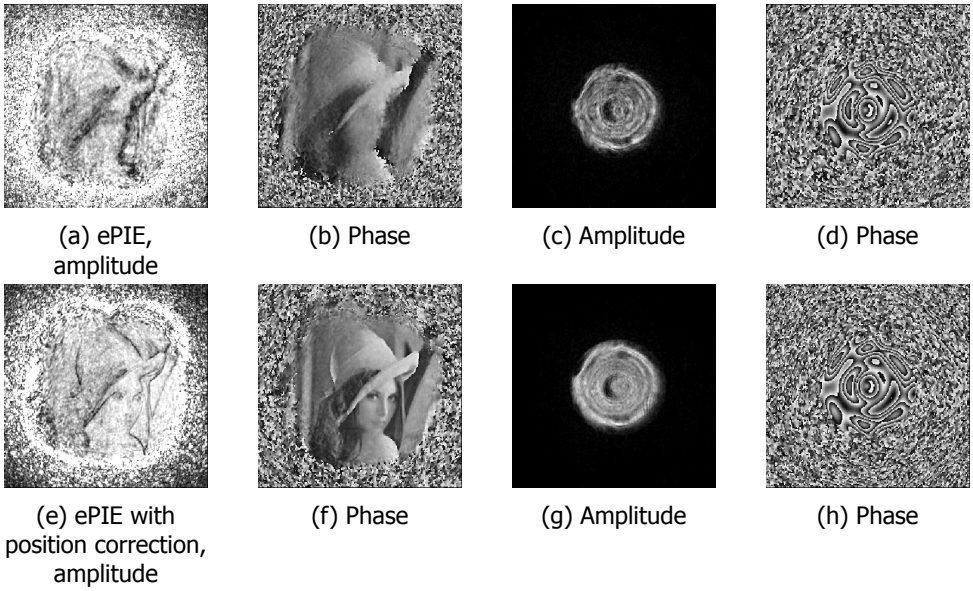

(a) ePIE, amplitude (b) Phase (c) Amplitude (d) Phase

(e) ePIE with position correction, amplitude (f) Phase (g) Amplitude (h) Phase

Figure 3.9: Maximum random added offset to each probe position = $10\Delta x_o$. We have truncated the color scale for the object amplitude to make certain features more visible.

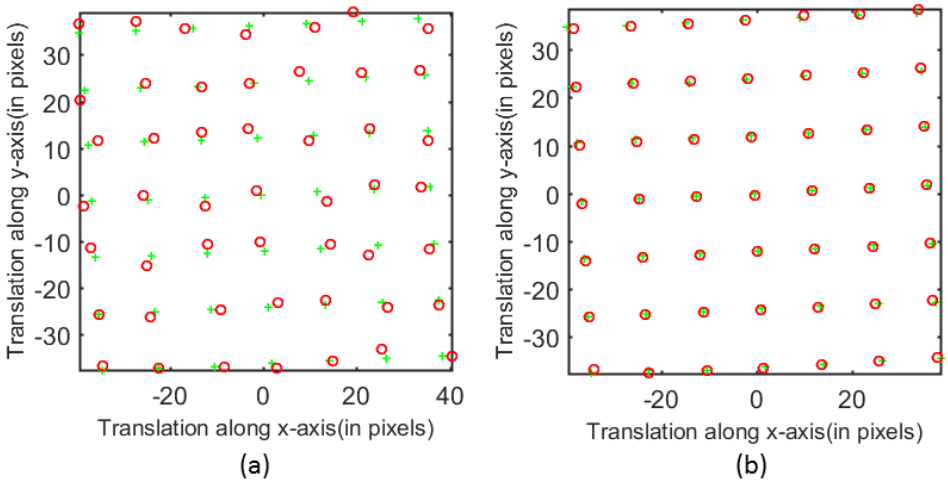

Figure 3.10: Scatter plot of the probe positions are shown for the case when the maximum initial random offset added to each probe position was $2\Delta x_o$. The green marks are the actual probe positions. (a) The red circles represent the initial guessed probe positions. (b) The red circles represent the final reconstructed probe positions.

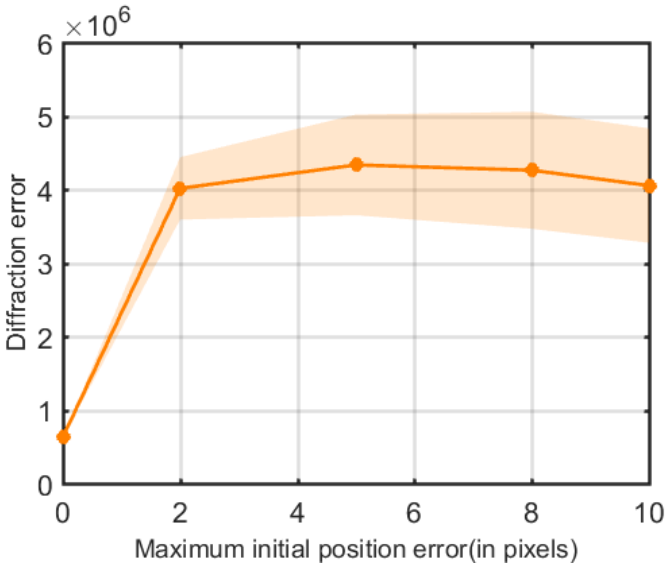

(a)

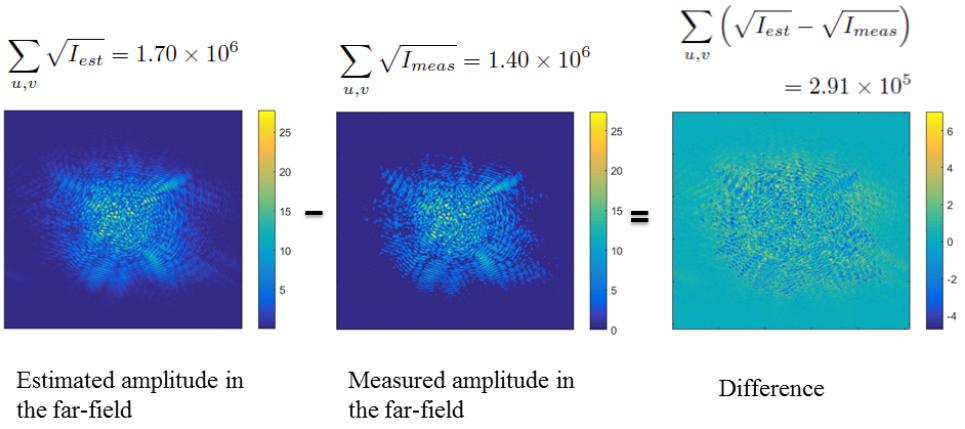

(b)

Figure 3.11: Diffraction error in the far-field. (a) Here, for each maximum initial position error, ten simulations were performed with different random initial offsets. The solid line represents the mean value of the final diffraction error of the ten simulations, whereas the patch shows the standard deviation. The diffraction error is calculated using Eq. (3.13).(b) To show what it means to have diffraction error of the order of 10^5, estimated, the measured amplitude in the far-field and its difference are shown here for the probe position $(1, 1)$ and when there is no error in the probe position.

3.5. Conclusion

We have tested a novel technique to correct the lateral probe positions in ptychography. It is a straightforward extension to the ePIE, and with simulations, we showed that it could correct the probe positions to sub-pixel accuracy even in the presence of noise. Each iteration of this method is less computationally inexpensive than the cross-correlation method, and it achieves comparable accuracy once it is converged. Visible light experimental data was used to analyze this technique. Experimental results show significant improvements in the reconstruction. We anticipate that these results can be employed in realizing the full potential of ptychographic coherent diffractive imaging for high-resolution imaging.

References

[1] P. Dwivedi, A. P. Konijnenberg, S. F. Pereira, and H. P. Urbach. Lateral position correction in ptychography using the gradient of intensity patterns. *Ultramicroscopy*, 192:29–36, 2018.

[2] J. M. Rodenburg. *Ptychography and related diffractive imaging methods*, volume 150 of *Advances in Imaging and Electron Physics*. Elsevier, 2008.

[3] H. M. L. Faulkner and J. M. Rodenburg. Movable aperture lensless transmission microscopy: A novel phase retrieval algorithm. *Physical Review Letters*, 93(2):023903–1, 2004.

[4] A. M. Maiden and J. M. Rodenburg. An improved ptychographical phase retrieval algorithm. *Ultramicroscopy*, 109(10):1256–1262, 2009.

[5] T. B. Edo, D. J. Batey, A. M. Maiden, C. Rau, U. Wagner, Z. D. Pesic, T. A. Waigh, and J. M. Rodenburg. Sampling in x-ray ptychography. *Physical Review A*, 87(5), 2013.

[6] P. Thibault, M. Dierolf, O. Bunk, A. Menzel, and F. Pfeiffer. Probe retrieval in ptychographic coherent diffractive imaging. *Ultramicroscopy*, 109(4):338–343, 2009.

[7] A. P. Konijnenberg, W. M. J. Coene, S. F. Pereira, and H. P. Urbach. Combining ptychographical algorithms with the hybrid input-output (hio) algorithm. *Ultramicroscopy*, 171:43–54, 2016.

[8] H. M. L. Faulkner and J. M. Rodenburg. Error tolerance of an iterative phase retrieval algorithm for movable illumination microscopy. *Ultramicroscopy*, 103(2):153–164, 2005.

[9] F. Hue, J. M. Rodenburg, A. M. Maiden, and P. A. Midgley. Error tolerance of an iterative phase retrieval algorithm for movable illumination microscopy. *Ultramicroscopy*, 111(8):1117–1123, 2011.

[10] F. Zhang, I. Peterson, J. Vila-Comamala, F. Berenguer A. Diaz, R. Bean, B. Chen, A. Menzel, I. K. Robinson, and J. M. Rodenburg. Translation position determination in ptychographic coherent diffraction imaging. *Optics Express*, 21(11):13592–13606, 2013.

[11] M. Guizar-Sicairos and J. R. Fienup. Phase retrieval with transverse translation diversity: a nonlinear optimization approach. *Optics Express*, 16(10):7264–7278, 2008.

[12] A. Tripathi, I. McNulty, and O. G. Shpyrko. Ptychographic overlap constraint errors and the limits of their numerical recovery using conjugate gradient descent methods. *Optics Express*, 22(2):1452–1466, 2014.

[13] A. Shenfield and J. M. Rodenburg. Evolutionary determination of experimental parameters for ptychographical imaging. *Journal of Applied Physics*, 109(12), 2011.

[14] M. Beckers, T. Senkbeil, T. Gorniak, K. Giewekemeyer, T. Salditt, and A. Rosenhahn. Drift correction in ptychographic diffractive imaging. *Ultramicroscopy*, 126:44–47, 2013.

[15] A. M. Maiden, M. J. Humphry, M. C. Sarahan, B. Kraus, and J. M. Rodenburg. An annealing algorithm to correct positioning errors in ptychography. *Ultramicroscopy*, 120:64–72, 2012.

[16] M. Guizar-Sicairos, S. T. Thurman, and J. R. Fienup. Efficient subpixel image registration algorithms. *Optics Letters*, 33(2):156–158, 2008.

[17] P. Dwivedi, A. P. Konijnenberg, S. F. Pereira, and H. P. Urbach. New method for probe position correction for ptychography. In 10329, editor, *Proceedings of SPIE - The International Society for Optical Engineering*, 2017.

[18] H. Zhang, J. Xie, J. Liu, and Y. Wang. Elimination of a zero-order beam induced by a pixelated spatial light modulator for holographic projection. *Applied Optics*, 48(30):5834–5841, 2009.

4

Lateral position correction using HIO and cross-correlation

Ptychography is a form of coherent diffractive imaging; it employs far-field intensity patterns of the object to reconstruct the object. In ptychography, an important limiting factor for the reconstructed image quality is the uncertainty in the probe positions. Here, we propose a new approach which uses the hybrid input-output (HIO) algorithm and cross-correlation in a way that can correct our estimates of the probe positions. The performance and limitations of the method in the presence of noise, varying overlap, and maximum recoverable error are studied using simulations. A brief comparison with other existing methods is also discussed here.

Part of this chapter is published in Journal of Optics, **21**, 3 (2019) [1]

4.1. Introduction

Computationally imaging an object—replacing lenses with algorithms—is becoming extremely popular. Over the years, several iterative algorithms have been developed including the error-reduction (ER) algorithm [2], the hybrid input-output (HIO) algorithm [3], the hybrid projection-reflection (HPR) algorithm [4], the relaxed averaged alternating reflectors (RAAR) algorithm [5]. These methods reconstruct an object from a single intensity pattern. An algorithm called ptychographic iterative engine (PIE) [6] was developed, which uses several intensity patterns for reconstruction and was found to be superior to other existing methods.

In ptychography, an object is scanned by a localized probe in a way that the neighbouring probe positions should overlap with each other; corresponding to these probe positions, the diffraction patterns are captured in the far-field. These diffraction patterns are employed to reconstruct the complex object. The crucial aspect for the success of this method is the overlap between neighbouring probe positions. The optimum overlap has been found to be about 60% [7].

Ptychography has given significant results with visible light experiments [8], whereas the reconstructions have suffered with X-rays and e-beams data—the limitations were due to the inaccurately known initial parameters, e.g. probe positions [9, 10]. The illuminating probe function, for instance, should be known accurately. To this end, extended PIE has been introduced to eliminate the requirement of accurately known probe function [11]. Later on, it was found that probe positions for electron ptychography should be known with an accuracy of 50 pm [12], which is difficult to achieve experimentally. Several successful attempts, subsequently, have been made to solve the probe positions correction problem.

For example, one finds in the literature the "annealing approach" based on "trial and error", but this is computationally expensive [13]. In yet another study, nonlinear (NL) optimization with ePIE is used [14]. NL optimization, however, can not correct with sub-pixel accuracy. To achieve this, one is required to use the cross-correlation (CC) method [12], which has been widely used. Recently, we have proposed a new method based on gradient of intensity patterns [15] that can correct the probe positions with sub-pixel accuracy while being less computationally expensive than the CC method.

In this work, we introduce a novel method for the correction of the probe positions in ptychography [16]. This method combines the well-known techniques HIO and cross-correlation in a way that it can also correct probe positions in ptychography. This is possible mainly due to two important properties:

- The reconstructed object using single intensity method is indifferent to wrong / shifted support constraint, except, the reconstructed object is shifted laterally as shown in Fig. 4.1.
- Sufficient overlap between neighbouring probe positions gives information about the relative shift between neighbouring probe positions. If the probe positions were correct, the overlapped part of the object corresponding to neighbouring probe positions will coincide with each other (see Fig. 4.2).

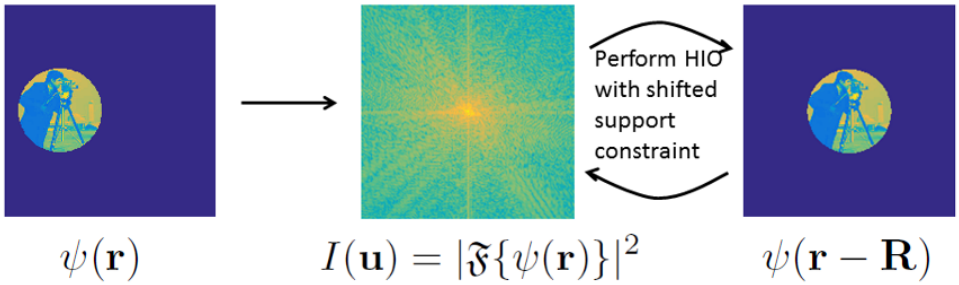

Figure 4.1: Effect of shifted support constraint on HIO. Here, $\mathfrak{F}$ represents the Fourier transform.

The performance of this method with varying parameters and its limitations are presented here. This chapter is organized as follows: in Section 4.2, we elaborate on the new method in detail. Section 4.3 details the simulation results to asses its performance. A brief comparison with intensity gradient method is discussed in Section 4.4. In Section 4.5, we discuss the main findings and its limitations. Finally, we present the conclusions in Section 4.6.

4.2. The method

In ptychography, an object $O(\mathbf{r})$ is scanned by a probe/aperture $P(\mathbf{r}-\mathbf{R}^j)$ and the corresponding intensity patterns $I^j(\mathbf{u})$ are captured in the far-field. Here $\mathbf{r}$ and $\mathbf{u}$ are the coordinate vectors in the real and the reciprocal space respectively. $\mathbf{R}^j$ is the j^{th} probe position vector. If J is the total number of probe positions, $j = 1, 2, 3...J$.

From the property of the Fourier transform, shifting a wave-field along the x or y axis in real space does not affect the intensity pattern in the far-field. Therefore, for a single-intensity phase retrieval method, the reconstruction of the object will be indifferent to the position of the support constraint except the reconstructed object will be updated at a different place in the real space. In Fig. 4.1, the exit wave $\psi(\mathbf{r}) = O(\mathbf{r})P(\mathbf{r})$, the intensity pattern in the far-field, and the reconstruction with shifted support constraint $P(\mathbf{r}-\mathbf{R})$ are shown. Here, the reconstruction was performed using HIO.

Now, let us assume that the probe positions in ptychography are not accurately known. If we reconstruct the exit wave $\psi^j(\mathbf{r})$ defined by the probe $P(\mathbf{r}-\mathbf{R}^j)$ using HIO and find the part of the object $O^j(\mathbf{r})$ corresponding to $\psi^j(\mathbf{r})$, we will have the correct part of the object at a wrong probe position. This will create a miss-match in the overlapped region between parts of the object $O^{j-1}(\mathbf{r})$ and $O^j(\mathbf{r})$ which correspond to neighbouring probe positions. Hence, by finding the maxima of their cross-correlation, one can find the relative shift between neighbouring probe positions. In Fig. 4.2, the overlapped region of $O^{j-1}(\mathbf{r})$ and $O^j(\mathbf{r})$ are shown. In Fig. 4.2(a), the probe positions are known accurately; in Fig. 4.2(b), the estimated probe positions have an error.

The proposed algorithm is a sequential combination of ePIE, HIO and cross-correlation. For the k^{th} iteration, the steps of the algorithm are as follows:

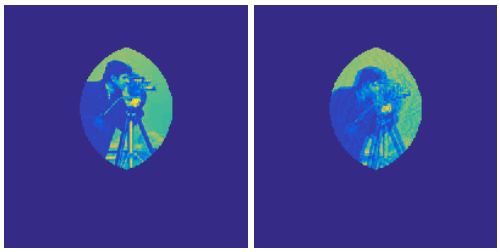

(a) (b)

Figure 4.2: Overlap part of the object, i.e. $O^{j-1}(\mathbf{r})O^{j}(\mathbf{r})$ are shown: (a) probe positions are accurately known, (b) probe positions have some error.

1. Perform a few iterations (say l) of ePIE with the estimated object $O_k(\mathbf{r})$, the probe $P_k(\mathbf{r})$ and the probe positions $\{\mathbf{R}_k^j\}_{j=1}^J$ to obtain a better estimate of the object $O_k'(\mathbf{r})$ and the probe $P_k'(\mathbf{r})$.

2. Calculate the exit wave corresponding to each probe position j as:

$$\psi_k^j(\mathbf{r}) = O_k'(\mathbf{r})P_k'(\mathbf{r} - \mathbf{R}_k^j). \tag{4.1}$$

3. Update each exit wave $\psi_k^j(\mathbf{r})$ separately using HIO (say m iterations) where the support constraint will be defined by the probe function $P_k'(\mathbf{r} - \mathbf{R}_k^j)$.

4. With each improved exit wave $\psi_k^j(\mathbf{r})$, calculate the corresponding part of the object as:

$$O_k^j(\mathbf{r}) = \begin{cases} \frac{\psi_k^j(\mathbf{r})P_k'^*(\mathbf{r}-\mathbf{R}_k^j)}{|P_k'(\mathbf{r}-\mathbf{R}_k^j)|^2} & \text{if } |P_k'(\mathbf{r} - \mathbf{R}_k^j)|^2 \geq \alpha \\ 0 & \text{otherwise,} \end{cases} \tag{4.2}$$

where α is a small number.

5. Calculate the overlapped region $S_k^j(\mathbf{r})$ between neighbouring parts of the object, i.e. $O_k^{j-1}(\mathbf{r})$ and $O_k^j(\mathbf{r})$ as:

$$S_k^j(\mathbf{r}) = \begin{cases} 1 & \text{if } |O_k^{j-1}(\mathbf{r})O_k^j(\mathbf{r})| \geq \beta \\ 0 & \text{otherwise,} \end{cases} \tag{4.3}$$

where β is a threshold parameter. Then, we calculate the cross-correlation C as:

$$C(\boldsymbol{\rho}) = |\sum_{\mathbf{r}} O_k^{j-1}(\mathbf{r})S_k^j(\mathbf{r})O_k^{j*}(\mathbf{r} - \boldsymbol{\rho})S_k^j(\mathbf{r} - \boldsymbol{\rho})|. \tag{4.4}$$

We determine the vector $\boldsymbol{\rho} = \boldsymbol{\rho}_{\text{max}}$ for which $C(\boldsymbol{\rho})$ is maximum, and $\boldsymbol{\rho}_{\text{max}}$ should be equal to the relative shift between neighbouring probe positions

$\Delta\mathbf{R}_k^j \equiv \mathbf{R}_k^j - \mathbf{R}_k^{j-1}$. Then, we update $\mathbf{R}_k^j$ and $O_k^j(\mathbf{r})$ as:

$$\mathbf{R}_{k+1}^j = \mathbf{R}_k^j + \Delta\mathbf{R}_k^j, \tag{4.5}$$

$$O_k^j(\mathbf{r}) = O_k^j(\mathbf{r} - \Delta\mathbf{R}_k^j). \tag{4.6}$$

Step 5 is performed for all the probe positions $j = 1, 2, 3...J$ sequentially to find the updated probe positions $\{\mathbf{R}_{k+1}^j\}_{j=1}^J$. Note that, $j-1$ and j do not always correspond to neighbouring probe positions. Therefore, when probe position $j-1$ is not neighbour of the probe position j, we replace $j-1$ by neighbouring probe position. In Fig. 4.3, the shaded regions show the overlapped part which are used for the probe positions correction.

6. With the updated probe positions $\{\mathbf{R}_{k+1}^j\}_{j=1}^J$, obtain the object estimate as a weighted average of the ψ_k^j given by:

$$O_{k+1}(\mathbf{r}) = \begin{cases} \frac{\sum_j \psi_k^j(\mathbf{r}) P_k^*(\mathbf{r}-\mathbf{R}_{k+1}^j)}{\sum_j |P_k(\mathbf{r}-\mathbf{R}_{k+1}^j)|^2} & \text{if } |P_k(\mathbf{r}-\mathbf{R}_{k+1}^j)|^2 \geq \alpha \\ 0 & \text{otherwise,} \end{cases} \tag{4.7}$$

where α is a small number, and update the probe function by:

$$P_{k+1} = P_k'. \tag{4.8}$$

7. Go back to step 1.

Each iteration of this method contains 5–10 iterations of ePIE and 50–200 iterations of HIO for each probe position. In Section 4.3.2, simulations are shown for varying number of HIO iterations. Since in the step 3, HIO has been used with the $P_k'(\mathbf{r}-\mathbf{R}_k^j)$ as a support constraint, the proposed method has a limitation on the probe function: it should be zero outside the known defined area.

4.3. Simulation results

4.3.1. Simulations

To assess the performance of the algorithm, we performed simulations using parameters that correspond to a visible light experiment. Let us suppose that the wavelength of the light is $\lambda = 400$ nm; the focal length of the lens which was used to create the Fourier transform, is $f = 10$ cm; the detector has 512×512 pixels and the detector pixel size is $\Delta x_d = 10\mu$m. The detector pixel size in x and y directions are same. Thus, the size of the pixel along the x-axis in object plane is $\Delta x_o = \frac{\lambda f}{N \Delta x_d}$. The object used in the simulations has 224×224 pixels. The illuminating probe was created using a pinhole of radius $67.2\Delta x_o$ and placed 1.25 mm upstream of the object. To conform with the limitation on the probe function, the illumination function on the object plane was set to zero outside the pinhole of radius $67.2\Delta x_o$. To define the probe positions, a grid of 4×4 was created with a grid interval of

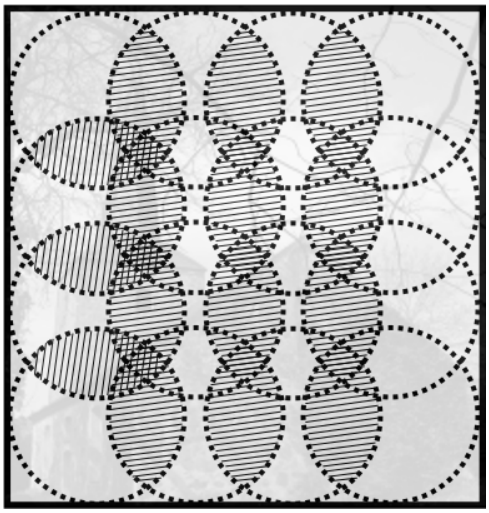

Figure 4.3: The shaded regions show the used overlap between neighbouring probe positions.

$22\Delta x_o$. The overlap between the neighbouring probe positions was 82%. Random integer offset taken from [-5,5] pixels was added to each probe positions; these probe positions were used to generate the intensity patterns.

'Camera Man' was used as the object amplitude varying from [0.23,1]; 'Pirate' was used as the object phase varying from [-0.7π,0.7π]. In the simulations, first l iterations of PIE or ePIE were performed to obtain a better object estimate. Then, m iterations of HIO were performed sequentially as explained in Section 4.2. We call the combination—l iterations of PIE, m iterations of HIO, and position correction—as one iteration of the proposed method. During the first iteration of the proposed method, we used $l = 10$ iterations of PIE and $m = 70$ iterations of HIO. From the second iteration onwards, $l = 5$ iterations of ePIE and $m = 70$ iterations of HIO were used. The feedback parameter for HIO was 0.9. The algorithm ran 5 iterations of the proposed method.

Figs. 4.4 (a-d) show the object and the probe to generate the intensity patterns. Figs. 4.4 (e-h) are the reconstructed object and the probe when ePIE is used with incorrect probe positions. Figs. 4.4 (i-l) show the reconstruction of the object and the probe when the proposed method was used. We calculate the mean error of the estimated probe positions using the following expression:

$$E_k = \sqrt{< \Delta X_k^j - \overline{\Delta X_k^j} >^2 + < \Delta Y_k^j - \overline{\Delta Y_k^j} >^2} \tag{4.9}$$

Here, $\Delta X_k^j = X^j - X_k^j$ and $\Delta Y_k^j = Y^j - Y_k^j$, where $(X^j, Y^j) = \mathbf{R}^j$ is the correct probe position and $(X_k^j, Y_k^j) = \mathbf{R}_k^j$ is the estimated probe position at the k^{th} iteration and the j^{th} probe position.

In Fig. 4.5, the plot for the RMS error of the probe positions versus the iteration number are shown. Ten simulations were performed with random initial probe

position errors varying from [-5,5] pixels. The solid line shows the mean and the semi-transparent patch is the standard deviation. As can be seen, for all ten simulations, the probe positions converge to the correct values in one iteration of the proposed method. This method can correct the probe positions with integer pixel accuracy.

4.3.2. Varying number of ePIE and HIO iterations

The entire point of ptychography is that the neighbouring exit waves should overlap with each other, whereas here, the exit waves are also updated separately using HIO. One can question on the added value of ptychography if the object is already being reconstructed using HIO. Hence, we performed ten simulations when ePIE was not used at all. The parameters for the simulations were the same as in Section 4.3.1 except the number of PIE iterations l was zero. As can be seen from the Fig. 4.6, the algorithm diverges. It can be explained by the inability of HIO to converge to the correct solution. There is an equal probability for HIO to converge to the twin image of the object if the support constraint is centro-symmetric, which is the case for our simulations. Whereas, a few iterations of PIE gives a better initial estimate for HIO to converge to the correct solution.

On the other hand, as we change the number of HIO iterations while keeping the number of PIE iterations constant, the convergence of the proposed method changes. This can be clearly seen from Fig. 4.7 and 4.8. For each plot, ten simulations were performed where the simulations parameters were same as in Section 4.3.1 except the number of HIO iterations were changing. Fig. 4.7 and 4.8 show the simulation results for 4×4 and 8×8 probe positions respectively. The higher the number of HIO iterations, the better the convergence of the algorithm is. For 50, 100, and 200 iterations of HIO, the probe position errors converge after one iteration of the algorithm. On comparing the results for the case 4×4 and 8×8, this method is more robust for the 4×4 case than for the 8×8 case, where the area of the scanned object and the relative overlap were the same. This result may be explained by the fact that the probe is smaller for the 8×8 case, leading to a smaller overlapped area. Since this method tries to match the overlapped part of the object to correct the probe positions, the smaller overlapped area influences the results.

4.3.3. Simulations in the presence of noise

We also performed the simulations using the intensity patterns corrupted with Poisson noise. The number of photons per diffraction pattern was varied from 10^6 to 10^{10} and the RMS probe position errors are shown in Fig. 4.9. For each noise level, ten simulations were performed with random initial offsets taken from [-5,5] pixels for the probe position. Because RAAR is known to outperform HIO in the presence of noise, 100 iterations of RAAR was used instead of HIO. The other parameters for the simulations were the same as mentioned in Section 4.3.1. For the case of 10^8, 10^9 and 10^{10} photons, most of the times the method gives the accurate probe positions. Whereas, for number of photons $\leq 10^7$, the method starts to show deviations.

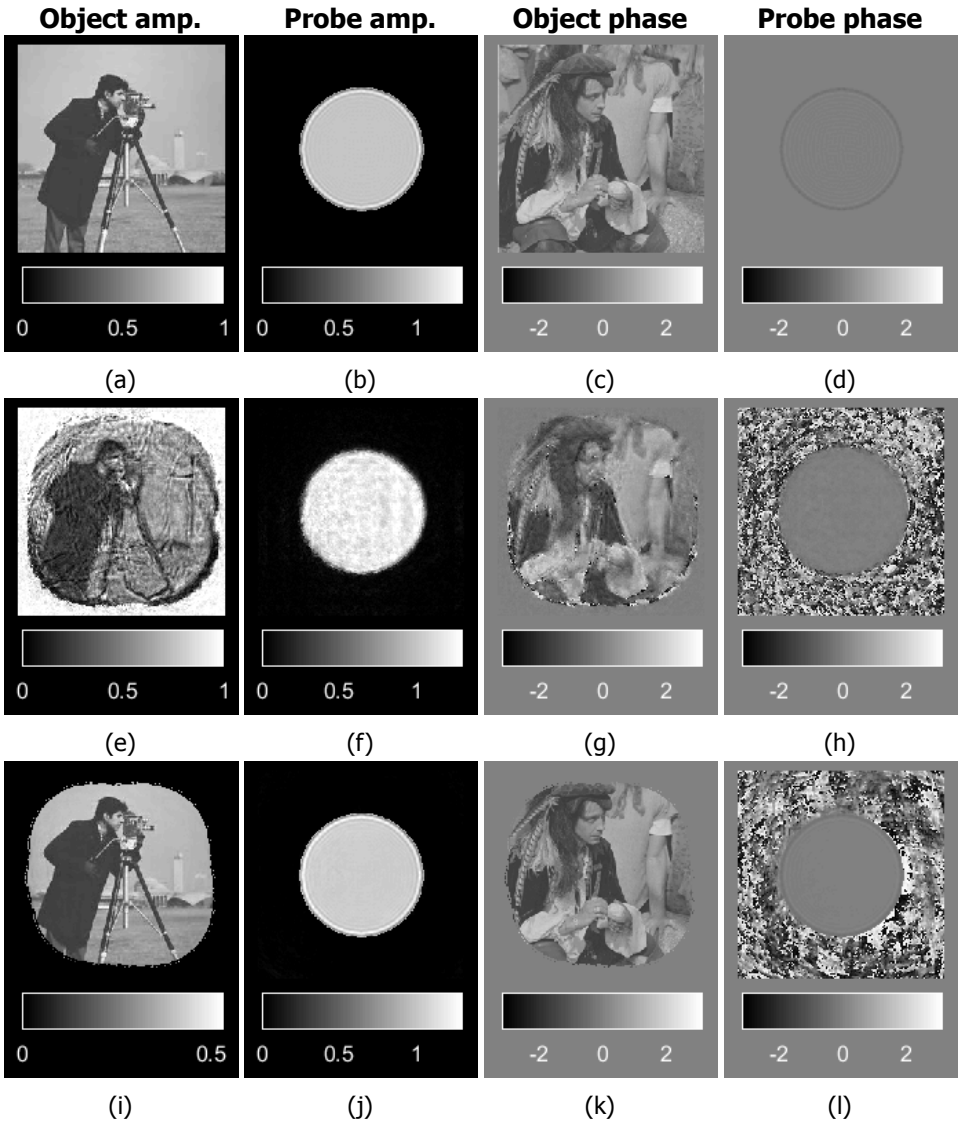

Figure 4.4: The reconstructed object and the probe function with and without probe positions correction are shown here. (a)–(d) are the used object and probe to generate intensity patterns. (e)–(h) are the reconstructions when ePIE without probe positions correction was used. (i)–(l) are the reconstructions when ePIE with probe positions correction was used. For these simulations, 4×4 probe positions were used to scan the object where the overlap between neighbouring probe positions was 82%. The introduced error in the probe position was varying between [-5,5] pixels.

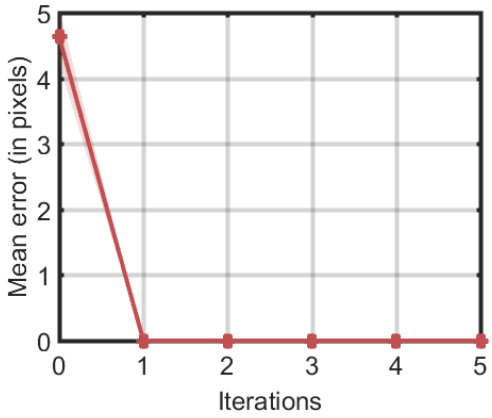

Figure 4.5: Mean probe position error versus iteration. Ten simulations were performed with random initial probe position error varying from [-5,5] pixels. Solid line represents the mean of the ten simulations.

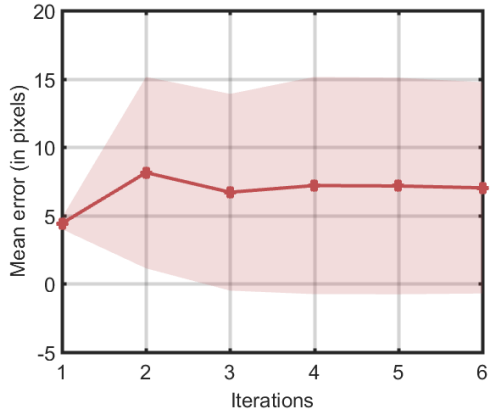

Figure 4.6: Mean error versus iteration. Here the simulations parameters are same as in Section 4.3.1 except the no. of iterations for PIE are zero i.e $l = 0$. Solid line represents the mean and the standard deviation is shown as the semi-transparent patch. Note that, due to wide variation in the reconstructed probe positions, standard deviation is larger than mean. Therefore, some part of the plot falls below zero.

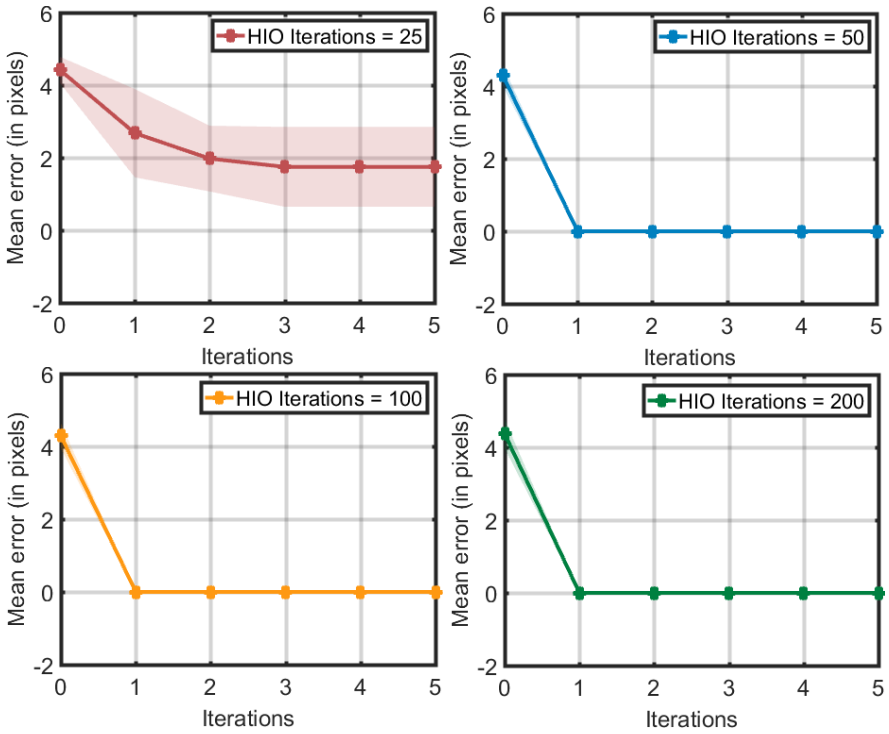

Figure 4.7: Mean error vs iterations for varying number of HIO iterations for the case of 4×4 probe positions. Solid line represents the mean and the standard deviation is shown as the semi-transparent patch.

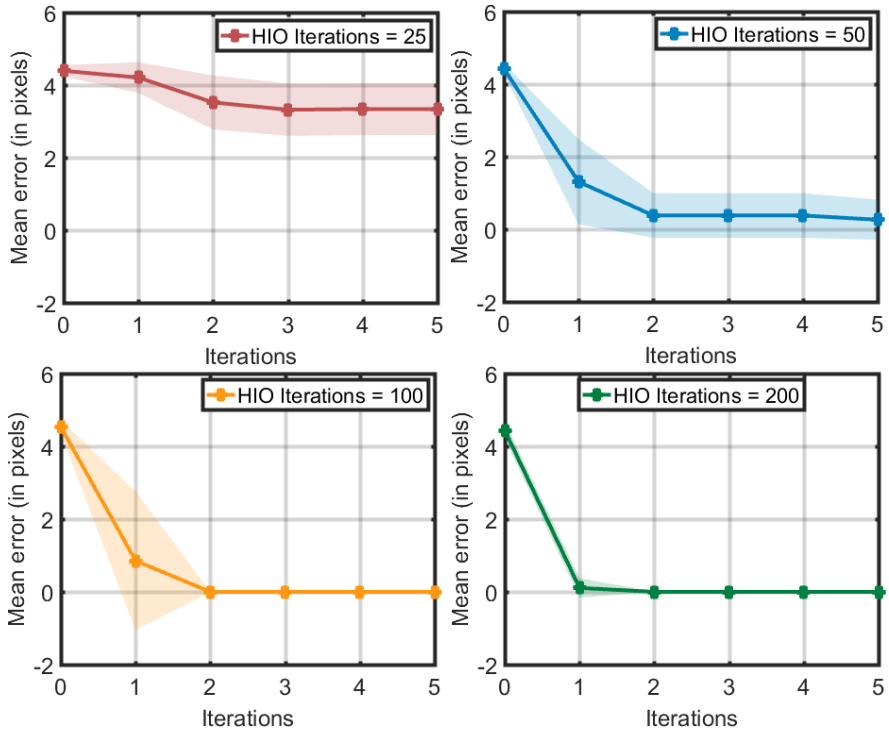

Figure 4.8: Mean error vs iterations for varying number of HIO iterations for the case of 8×8 probe positions. Solid line represents the mean and the standard deviation is shown as the semi-transparent patch.

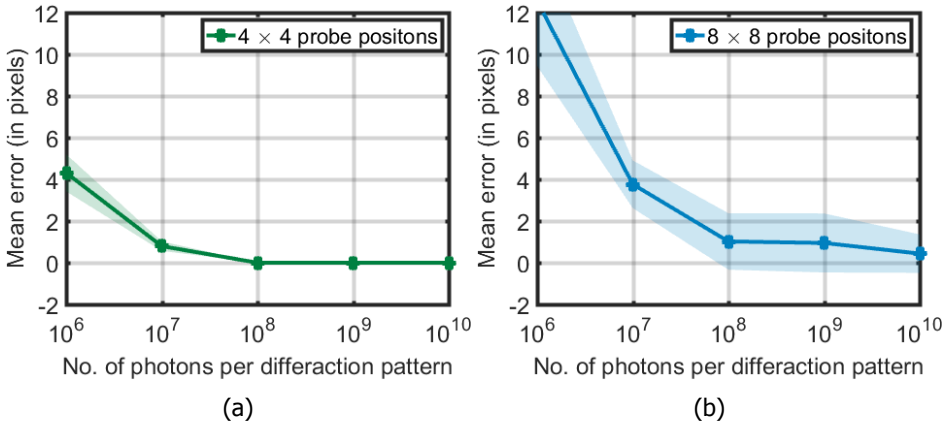

Figure 4.9: Simulations in the presence of Poisson noise. The number of photons per diffraction pattern varies from 10^6 to 10^{10}. For each noise level, ten simulations were performed with random initial error in the probe positions. Solid line represents the mean and the standard deviation is shown as the semi-transparent patch.

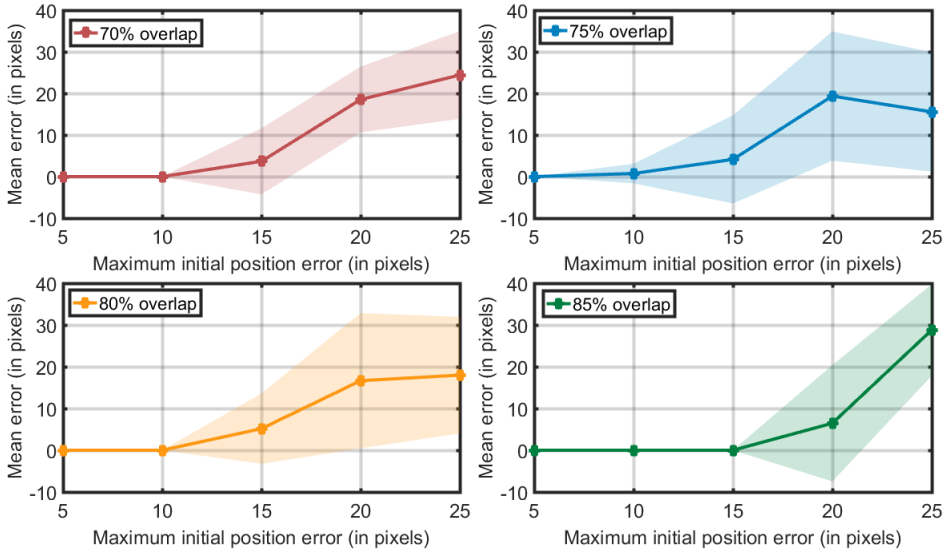

Figure 4.10: Effect of overlap and initial position error. For each overlap and maximum initial position error, ten simulations were performed with random initial probe positions. The solid line represents the mean error of the converged probe positions for ten simulations; the semi-transparent patch is the standard deviation.

4.3.4. Effect of the initial error and the overlap

To evaluate the performance of the algorithm with varying introduced initial maximum offset in the probe positions and overlap, the simulations results are shown in Fig. 4.10. Ten simulations were performed for each overlap and introduced initial maximum offsets in the probe positions. Solid lines show the mean of the final converged probe positions of ten simulations; the semi-transparent patch is the standard deviation of the same. As it can be seen from Fig. 4.10, all probe positions for all ten simulations converged to the correct probe positions when the initial introduced maximum offset was 5 and 10 pixels. As expected, the algorithm is robust for higher overlap between adjacent probes. For 85% overlap, this method corrected probe positions with 100% accuracy for 15 and 10 pixels of error in these ten simulations.

4.4. Comparison with intensity gradient method

For the comparison in terms of convergence, we have shown the simulation results for the intensity gradient method and the proposed method in Fig. 4.11. Ten simulations for each method were performed with randomly varying initial probe positions error. The simulation parameters were same as in Section 4.3.1. Fig 4.11(a) shows the simulation results when the intensity gradient method (IG) [15] was used to correct the probe positions. For IG method, the first 15 iterations were performed with PIE. Probe position correction started from 16th iteration. From 35th iteration onwards, probe update (ePIE) started. Fig. 4.11(b) shows

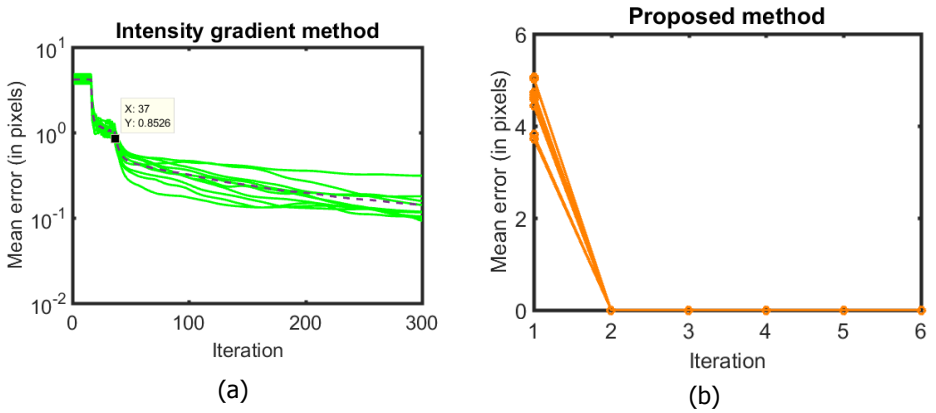

Figure 4.11: Comparison of the proposed method with intensity gradient method. Ten simulations were performed with initial probe positions varying randomly from [-5,5] pixels. (a) The dotted line is the mean of ten simulations. One iteration per probe position of this method consists of 1 ePIE and gradient of intensity (equivalent to 2 Fourier transforms). (b) One iteration per probe position of this method consists of 10 ePIE, 70 HIO, and 1 cross-correlation.

the simulation results when the proposed method was used to correct the probe positions.

The proposed method is correcting probe positions within one iteration. One iteration of the proposed method consists of 10 ePIE, 70 HIO, and 1 cross-correlation. Whereas, for IG method, the probe positions are corrected within 35 iterations with mean error of 0.80. One iteration of IG method has 1 ePIE and gradient of intensity (equivalent to 2 Fourier transforms). The proposed method is correcting probe positions with integer pixel accuracy; intensity gradient method is correcting with sub-pixel accuracy. A possible suggestion for the proposed method to achieve sub-pixel accuracy is to use matrix multiplication method proposed by Guizar-Sicairos et al. [17] as used in CC method to achieve sub-pixel positions correction [12].

4.5. Discussion

In this chapter, we have proposed an alternative method to correct the probe positions in ptychography which is significantly different from the cross-correlation method (CC). The CC method performs cross-correlation between the objects corresponding to consecutive iterations for each probe position. Here, we take the cross-correlation between the objects corresponding to the neighbouring probe positions to match the overlapped region.

In the presence of noise, the proposed method, however, is not as robust as the CC method is. There are a few possible explanations for that. In the presence of noise, some parts of the object have high probability to converge to its twin image or stagnate; thus it leads to wrong probe positions. Furthermore, since we match the overlapped part of the reconstructed objects corresponding to the neighbouring probe positions, the probe position correction depends on the previous probe

position. Therefore, one wrong probe position can propagate this error to the other probe positions as well.

All the simulations presented in this article are based on one assumption: the probe function is zero outside the known area, because the probe function is used as the support constraint while employing HIO. Due to this limitation, it can not be used in every possible application of ptychography. One specific application would be to reconstruct the wavefront, when it is scanned by a mask.

Another important observation is that our method gives better results for a smaller number of probe positions than large number of probe positions, where the scanned area of the object and the relative overlap for the both cases were same. A possible explanation for this is that the size of the probe is smaller for the case of large number of probe positions, which results in even smaller overlapped area. Since this method tries to match the overlapped region, it does not perform well for a small overlapped area.

4.6. Conclusion

We have devised a novel technique which combines HIO and cross-correlation to correct the probe positions in ptychography. This method can correct probe positions with integer pixel accuracy. We have so far not found a case where this method outperforms the intensity gradient (IG) method or cross-correlation (CC) method. The results of the study show that it can be used as an alternative method for probe position correction. It has a limitation on the probe function which must be zero outside the defined area of the probe function. Due to this limitation, it can not be used in every possible application of ptychography. We, however, anticipate that this method, for example, can be used for wavefront reconstruction applications. Furthermore, these findings may help us to understand the probe position problem from a different perspective.

References

[1] P. Dwivedi, A. P. Konijnenberg, S. F. Pereira, J. Meisner, and H. P. Urbach. Position correction in ptychography using hybrid input–output (hio) and cross-correlation. *Journal of Optics*, 23(3), 2019.

[2] R. W. Gerchberg. A practical algorithm for the determination of phase from image and diffraction plane pictures. *Optik*, 35:237–246, 1972.

[3] J. R. Fienup. Reconstruction of an object from the modulus of its fourier transform. *Optics Letters*, 3(1):27–29, 1978.

[4] H. H. Bauschke, P. L. Combettes, and D. R. Luke. Hybrid projection–reflection method for phase retrieval. *Journal of the Optical Society of America A*, 20(6):1025–1034, 2003.

[5] D. R. Luke. Relaxed averaged alternating reflections for diffraction imaging. *Inverse Problems*, 21(1):37–50, 2005.

[6] J. M. Rodenburg and H. M. L. Faulkner. A phase retrieval algorithm for shifting illumination. *Applied Physics Letters*, 85(20):4795–4797, 2004.

[7] O. Bunk, M. Dierolf, S. Kynde, I. Johnson, O. Marti, and F. Pfeiffer. Influence of the overlap parameter on the convergence of the ptychographical iterative engine. *Ultramicroscopy*, 108(5):481–487, 2008.

[8] A. M. Maiden, J. M. Rodenburg, and M. J. Humphry. Optical ptychography: A practical implementation with useful resolution. *Optics Letters*, 35(15):2585–2587, 2010.

[9] M. Dierolf, A. Menzel, P. Thibault, P. Schneider, C. M. Kewish, R. Wepf, O. Bunk, and F. Pfeiffer. Ptychographic x-ray computed tomography at the nanoscale. *Nature*, 467(7314):436–439, 2010.

[10] F. Hue, J. M. Rodenburg, A. M. Maiden, and P. A. Midgley. Extended ptychography in the transmission electron microscope: Possibilities and limitations. *Ultramicroscopy*, 111(8):1117–1123, 2011.

[11] A. M. Maiden and J. M. Rodenburg. An improved ptychographical phase retrieval algorithm for diffractive imaging. *Ultramicroscopy*, 109(10):1256–1262, 2009.

[12] F. Zhang, I. Peterson, J. Vila-Comamala, A. Diaz, F. Berenguer, R. Bean, B. Chen, A. Menzel, I. K. Robinson, and J. M. Rodenburg. Translation position determination in ptychographic coherent diffraction imaging. *Optics Express*, 21(11):13592–13606, 2013.

[13] A. M. Maiden, M. J. Humphry, M. C. Sarahan, B. Kraus, and J. M. Rodenburg. An annealing algorithm to correct positioning errors in ptychography. *Ultramicroscopy*, 120:64–72, 2012.

[14] A. Tripathi, I. McNulty, and O. G. Shpyrko. Ptychographic overlap constraint errors and the limits of their numerical recovery using conjugate gradient descent methods. *Optics Express*, 22(2):1452–1466, 2014.

[15] P. Dwivedi, A. P. Konijnenberg, S. F. Pereira, and H. P. Urbach. Lateral position correction in ptychography using the gradient of intensity patterns. *Ultramicroscopy*, 192:29–36, 2018.

[16] P. Dwivedi, A. P. Konijnenberg, S. F. Pereira, and H. P. Urbach. An alternative method to correct translation positions in ptychography. In *Proceedings of SPIE - The International Society for Optical Engineering*, volume 10677, 2018.

[17] M. Guizar-Sicairos, S. T. Thurman, and J. R. Fienup. Efficient subpixel image registration algorithms. *Optics Letters*, 33(2):156–158, 2008.

5

Application I: ptychography as a wavefront sensor for high-NA EUV lithography

Wavefront aberrations measurements are required to test an EUV (Extreme ultraviolet) imaging system. For a high-NA EUV imaging system, where conventional wavefront sensing techniques show limitations, ptychography can be used for this purpose. However, at the wavelength region of EUV (i.e., 13.5 nm), the position accuracy of the scanning mask that is defined for ptychography is stringent. Therefore, we propose here ptychography combined with mask position correction. The simulated intensity patterns, the one we use, resemble expected EUV experimental data. Finally, we show the results in the presence of Poisson noise and the tolerance of the position correction method for error in mask positions.

Part of this chapter is published in Optical Engineering, **58**(4), 043102 (2019) [1]

5.1. Introduction

Over the past decades, the semiconductor industry uses optical projection for lithography technology. As the technology advances, the number of transistors on a chip increases exponentially—double every 18 months. Shortening the wavelength of light made this possible. Initially, the wavelength of 436 nm and 365 nm has been used for chip manufacturing. With these wavelengths, the node size of half a micron has been achieved [2]. To shrink the node size further, deep ultraviolet (248 nm and 193 nm) wavelengths were used. Afterwards, the combination of immersion technology and 193 nm lithography made 45 nm node size possible, and with higher NA, 32 nm of node size can also be achieved. Currently, with the EUV wavelength (13.5 nm), 13 nm node size is possible, and at high-NA, even smaller features are expected [3].

One of the key challenges in EUV lithography (EUVL) is the inspection of the optical system for its aberrations [4]. The most widespread method to accurately measure the wavefront and aberrations is interferometry, which is based on the interference pattern created by a reference and a test wave. These interferograms are used to retrieve the wavefront, and eventually the aberrations in the test wave. At EUV wavelengths, the accuracy for alignment of an optical set-up is much more challenging than for optical wavelengths. Therefore, several techniques were devised that are based on common path interferometry.

For instance, point-diffraction interferometry (PDI) method was suggested [5, 6] and had been applied to EUVL [7]. In this method, a semi-transparent membrane with a pinhole, which is placed at the image plane, generate an interference pattern. To create a clear interference pattern, the intensity at the pinhole should be low, which can be achieved by moving the semi-transparent membrane from focus to defocus. Consequently, the semi-transparent membrane should be almost opaque to transmit similar intensity of light. This criterion makes the PDI method inefficient for EUV lithography. Subsequently, phase-shifting point-diffraction interferometer (PS/PDI) [8, 9] was introduced, which was found to be 10 to 100 times more robust than PDI for EUV applications [10]. Unlike PDI, this method does not require the pinhole to be placed at the low intensity of light. However, this method is limited to imaging systems with low aberrations. Therefore, it is applied to imaging systems which are close to the diffraction-limited quality.

Another successful technique, called shear interferometry, was devised [11]. It is based on the interference of the test wave with its displaced copy. This technique is more robust than PDI and PS/PDI as it has a higher dynamic range in terms of aberrations. The limitation of this method is that it can not be used to measure the wavefront accurately near the edge of the pupil. Later on, Hartmann sensor was introduced to measure the aberrations of the test optics [12, 13]. It is a non-interferometric technique with high efficiency and a lower requirement for the coherence of light. This method uses a grid of small holes in an opaque screen placed in the path of the beam with a CCD camera behind it. Based on the geometrical parameters of the hole size, distance between the mask and camera, one can reconstruct the wavefront. This method has been applied for EUV application [14] but not for high-NA EUV.

Lately, one sees a push in the EUV technology to higher NAs (~0.55). In this case, traditional wavefront sensor techniques fail to address the aberrations, especially when they are large. Therefore, ptychography was proposed to be used as a wavefront sensor technique [15]. Ptychography is already intensively being used with visible light [16, 17], X-rays [18, 19], and e-beams [20, 21]. Now, it is also gaining attention for EUV wavelength [22]. Ptychography reconstruction depends upon the type of the used object and accurately known initial parameters. For short wavelengths, the requirements for accurately known parameters are stringent.

In this chapter, we use ptychography to reconstruct the aberrated EUV wavefront with inaccurately known initial parameters, for example, the position of the scanning mask. In Section 5.2, the ptychography and mask position correction algorithm is discussed. The simulations results with mask positions error as well as with Poisson noise are shown in Section 5.3. Finally, we present possible implications and conclusions in Section 5.4.

5.2. Ptychography and position correction method

As suggested in the previous section, ptychography iterative engine (PIE) [23] is used to reconstruct the aberrated EUV wavefront. In ptychography, an object is scanned by a mask and the corresponding far-field diffraction patterns are captured by the camera. These diffraction patterns are used to reconstruct the object. For short wavelengths such as X-rays and e-beams, the accuracy of the mask positions should be as high as 50 pm [24]. Hence, to mitigate the requirement for highly accurate mask positions, we used PIE with position correction method [25]. In Fig. 5.1, the flow chart for ptychography with positions correction are shown. In step 1, the exit field just after the object and mask is calculated. In step 2, the exit field is propagated to the far-field. In step 3, amplitude constraint is applied to the far-field. By amplitude constraint, we mean the replacement of the amplitude of the calculated far-field by the square root of the captured image intensity while keeping the phase of the far-field as it is. In step 4, the updated far-field is back-propagated to the object plane and the part of the object is updated corresponding to the current mask position. In step 5, the current mask position is corrected using the intensity gradient method as explained in Ref [25]. Finally, the mask is moved to the next position and the same steps from 1 – 5 are repeated.

5.3. Simulation results

5.3.1. Simulations

In Fig. 5.2, we show the experimental scheme used to calculate aberrations in the optical system (test optics). The pinhole is placed in the object plane; a check board mask is placed at the image plane. This mask scans the wavefront in the image plane and the corresponding intensity patterns at the far-field are recorded in the camera. With ptychography, we reconstruct the wavefront and eventually the present aberrations in the optical system.

To assess how accurately ptychography with position correction can reconstruct an EUV wavefront, we used the wavefront amplitude and phase as shown in Fig.

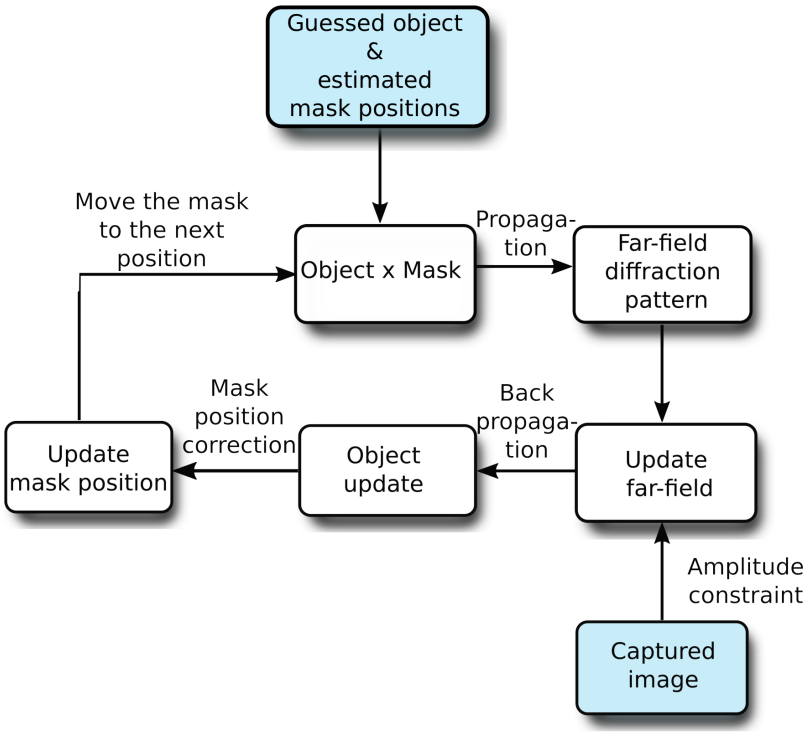

Figure 5.1: Flow chart for ptychography iterative engine (PIE) with mask position correction.

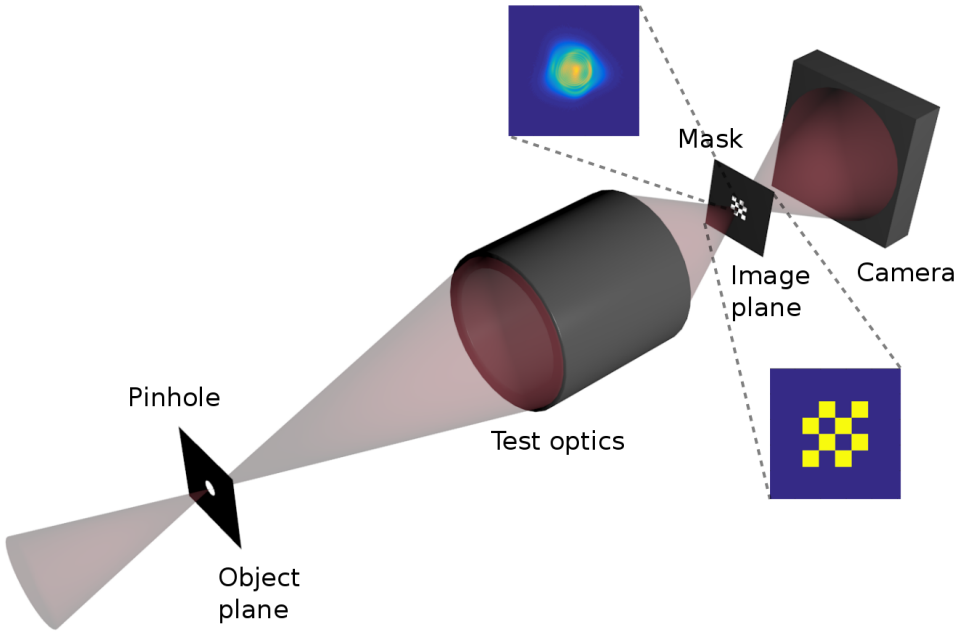

Figure 5.2: Set up for reconstructing the wavefront at the image plane and eventually to calculate the present aberrations in the optical system. Illumination is from left.

5.3(a) and (b). This wavefront amplitude and phase resemble to the expected EUV experimental data and the used wavelength of the light was 13.5 nm. It has approximately a size of $2\ \mu$m$\times 2\ \mu$m; here, the wavefront amplitude varies between [0, 0.0096] and the wavefront phase between $[-\pi, \pi]$. The wavefront was scanned by a $2\ \mu$m$\times 2\ \mu$m check board mask as shown in Fig. 5.4. The features in the mask gives a diverse diffraction pattern than with a mask without any features. Consequently, the reconstruction of the object is better. The mask was moved on a rectangular grid of 7×7 where the grid interval was 142.8 nm; these mask positions were used to create the intensity patterns in the far-field. A random initial error taken from [-5, 5] pixels were added to each mask positions; these positions were used as the estimated mask positions. Here, one pixel is equivalent to 7.81 nm.

Fig. 5.3(a) and (b) show the wavefront amplitude and phase which were used to create intensity patterns. Fig. 5.3(c) and (d) show the reconstruction when PIE was used, and Fig. 5.3(e) and (f) when PIE with position correction was used. The mean error of the positions of the mask is shown in Fig. 5.5(a); it can be clearly seen that the mask positions converge as accurately as 10^{-6} pixels (~ 7.81 fm). Fig. 5.5(b) shows the diffraction error versus iterations. Here, the diffraction error is the sum of squares error between the measured amplitude and the simulated amlitude in the far-field.

The simulated wavefront was generated from an imaging system which had aberrations. These present aberrations are shown in Fig. 5.6(a) as Zernike plots

(gray bars). To see how accurately these aberrations can be reconstructed, in Fig. 5.6(a), we have shown Zernike coefficient versus Zernike index for the reconstruct wavefront with and without positions correction. The errors in the reconstructed Zernike coefficients are also plotted in Fig. 5.6(b) and (c) for the cases when wavefront reconstruction was performed using PIE and PIE with positions correction. It can be clearly seen that PIE with position correction has retrieved the Zernike coefficients with an accuracy of 20 pm.

5.3.2. Effect of noise in the presence of position errors

Since noise is an inevitable part of experimental data, we performed simulations in presence of Poisson noise when mask position errors were also present. The simulation parameters were same as in the Section 5.3.1 including the mask position errors. We show the results for the case of $10^5, 10^6, 10^7$ number of photons per diffraction pattern. In Fig. 5.7(a), the diffraction error for varying Poisson noise are plotted. To give an idea of what it means to have an error of 0.45 in diffraction pattern, we have also shown the measured amplitude, the estimated amplitude, and the difference of the same for one mask positions in Fig. 5.7(b). The corresponding reconstructed wavefront amplitude and phase are shown in Fig. 5.8. It can be clearly seen that ptychography with position correction can reconstruct the wavefront with 10^6 photons per diffraction pattern while also correcting the mask position errors.

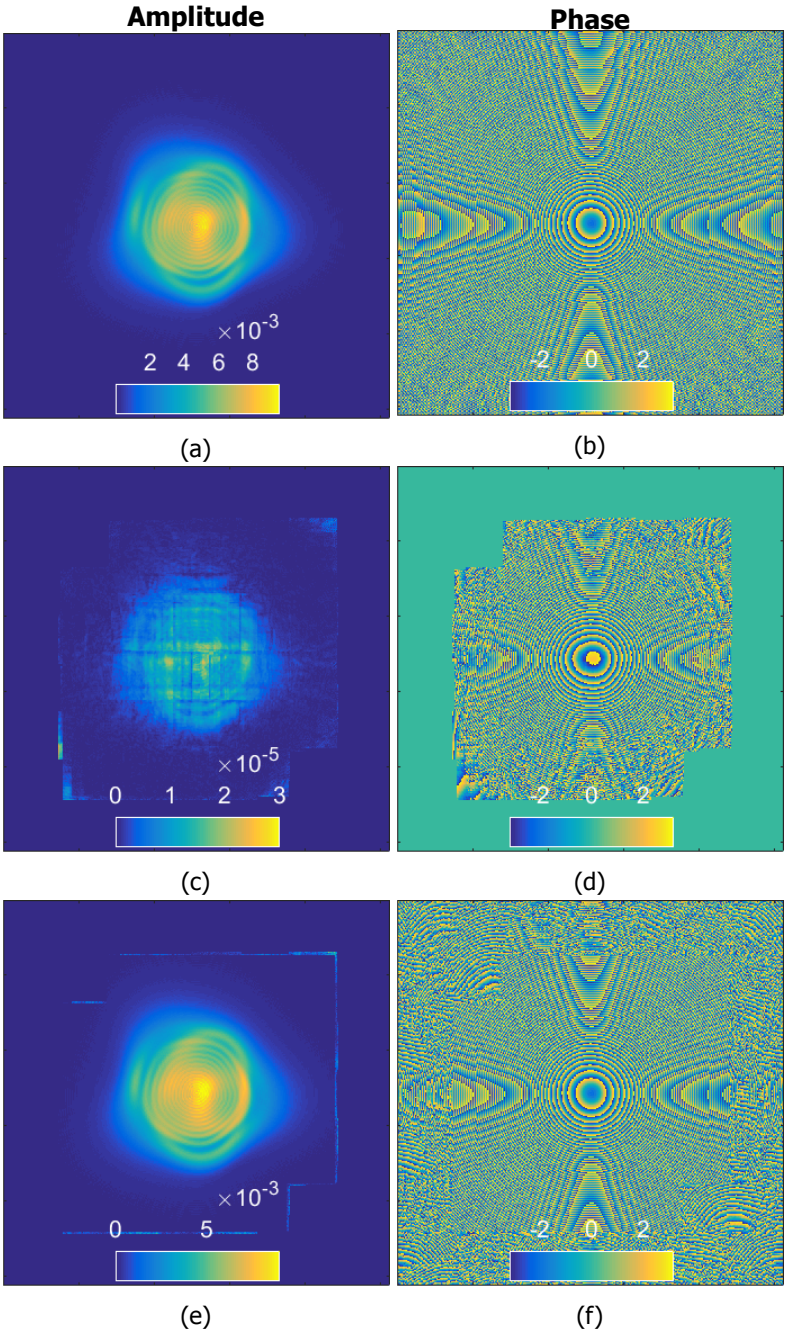

Figure 5.3: The reconstructed wavefront amplitude and phase with and without mask position correction. 7×7 mask positions were used to scan the wavefront where the overlap between neighbouring mask positions was 71.4%. The introduced error in the mask positions was varying between [-5,5] pixels (~[-39.05,39.05] nm). (a) and (b) The used wavefront amplitude (varying from 0 to 0.0096) and phase (varying from $-\pi$ to π). (c) and (d) Reconstructed wavefront amplitude and phase without position correction. (e) and (f) Reconstructed wavefront amplitude and phase with position correction.

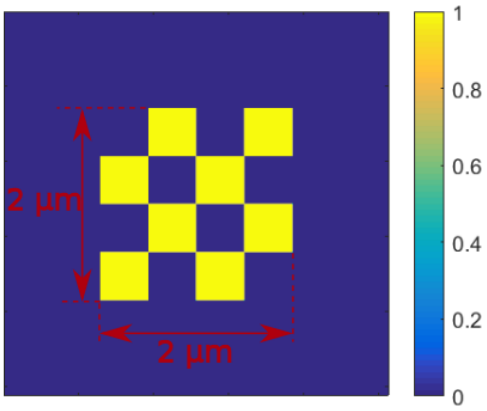

Figure 5.4: This mask was used to scan the wavefront and to create the intensity patterns in the far-field. The scan was performed in 7×7 rectangular grid with a grid interval of 142.8 nm.

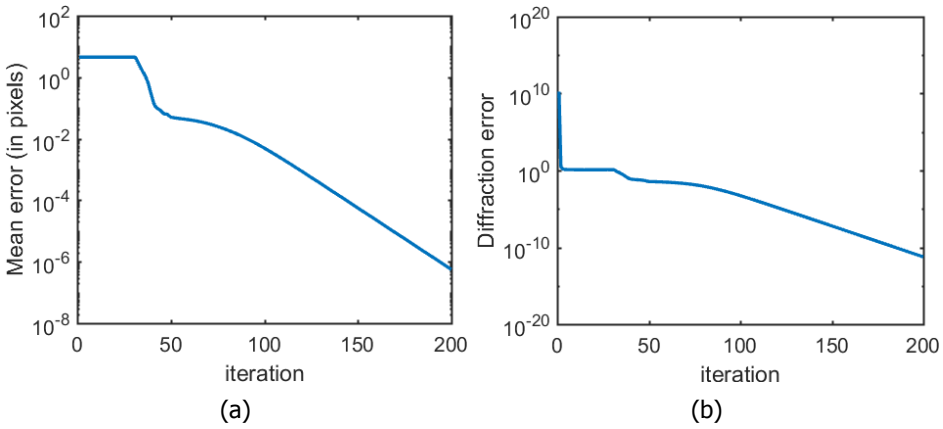

Figure 5.5: (a) Mean error in mask positions versus number of iterations. Here, one pixel is equivalent to 7.81 nm. (b) Diffraction error versus number of iterations.

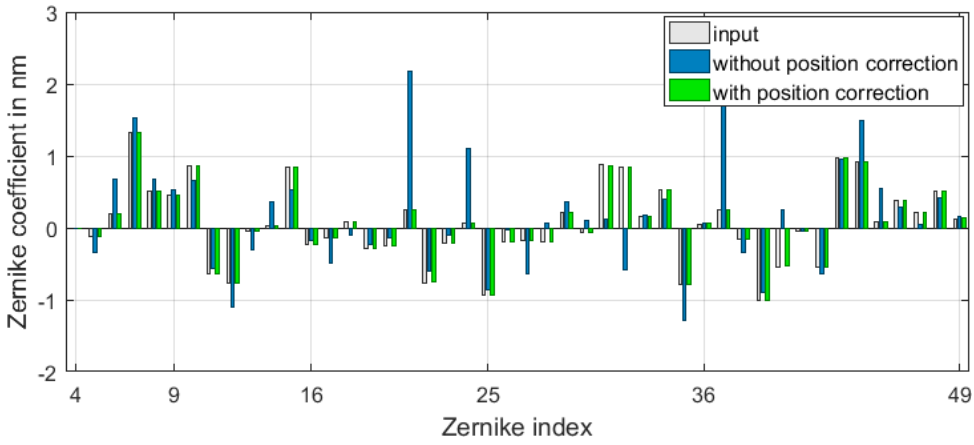

(a)

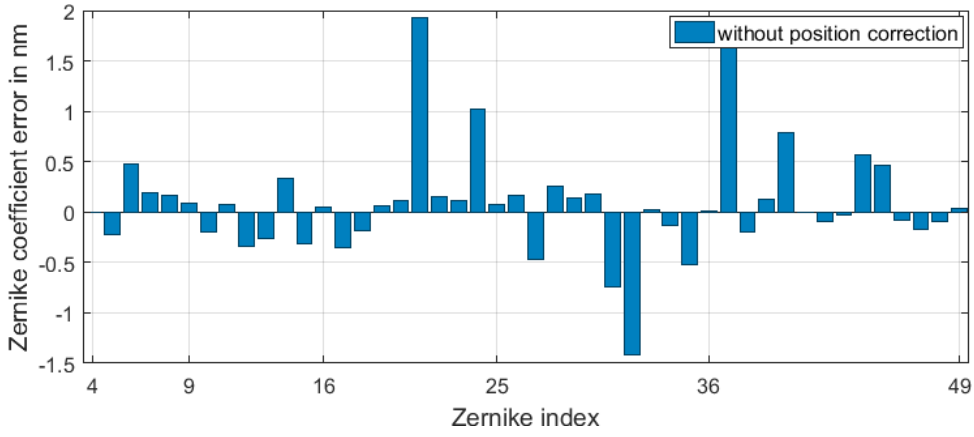

(b)

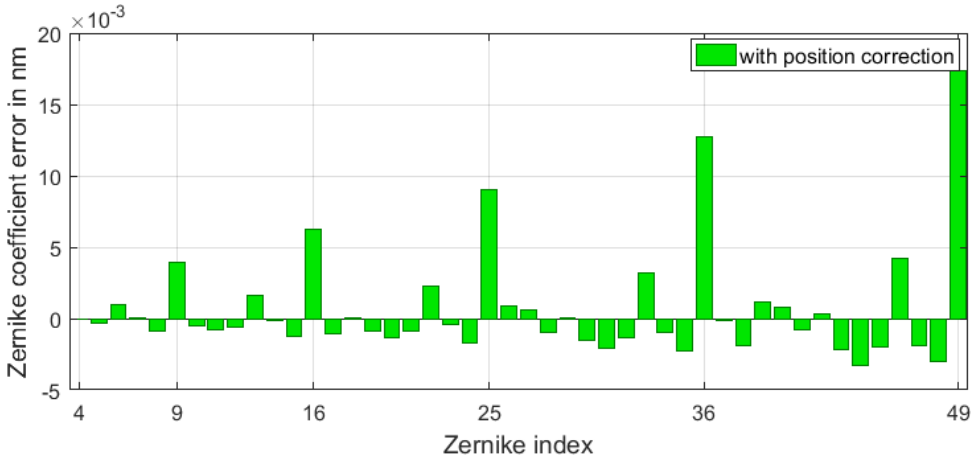

(c)

Figure 5.6: (a) Zernike coefficient versus Zernike index for the input and for the reconstructed wavefronts. Here, the wavefront is reconstructed with and without position correction. (b) Zernike coefficient error versus Zernike index for the reconstructed wavefront without position correction. (c) Zernike coefficient error versus Zernike index for the reconstructed wavefront with position correction.

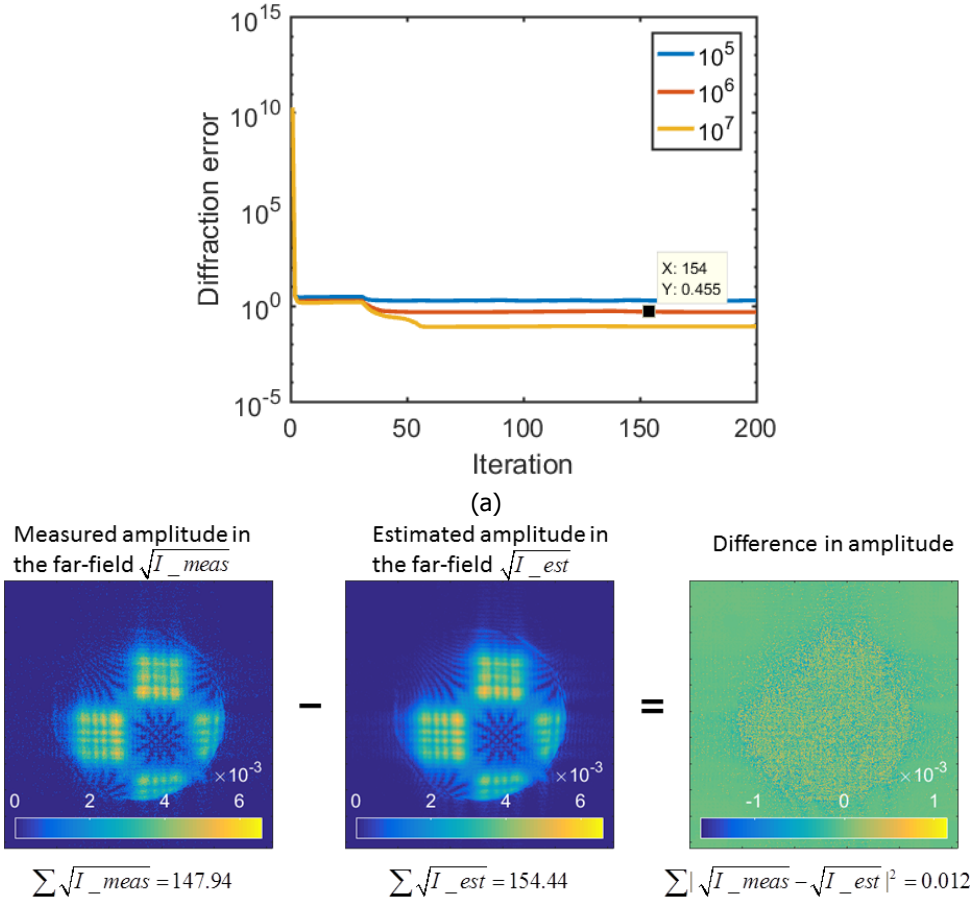

Figure 5.7: Reconstruction in presence of noise. (a) Diffraction error for varying number of photons per diffraction pattern in the presence of mask positions error. (b) To show what it means to have an error of 0.45 in diffraction pattern, we have shown here the measured amplitude, the estimated amplitude and the difference between the two for one mask positions when number of photons per diffraction pattern were 10^6.

5.3.3. Tolerance for maximum mask positions error

To find out how much this method can tolerate the error in the mask positions, we performed the simulations for different varying initial error in the mask positions. All other simulation parameters were the same as in the Section 5.3.1. Ten simulations were performed for each introduced initial error. In Fig. 5.9, the solid line represents the mean of the final mask positions error for all ten simulations; whereas semi-transparent patch shows the standard deviation of the same. As can be seen from the plot, the error increases with increasing introduced initial maximum error. When maximum introduced initial error was 5 pixels i.e., 39 nm, all the simulations

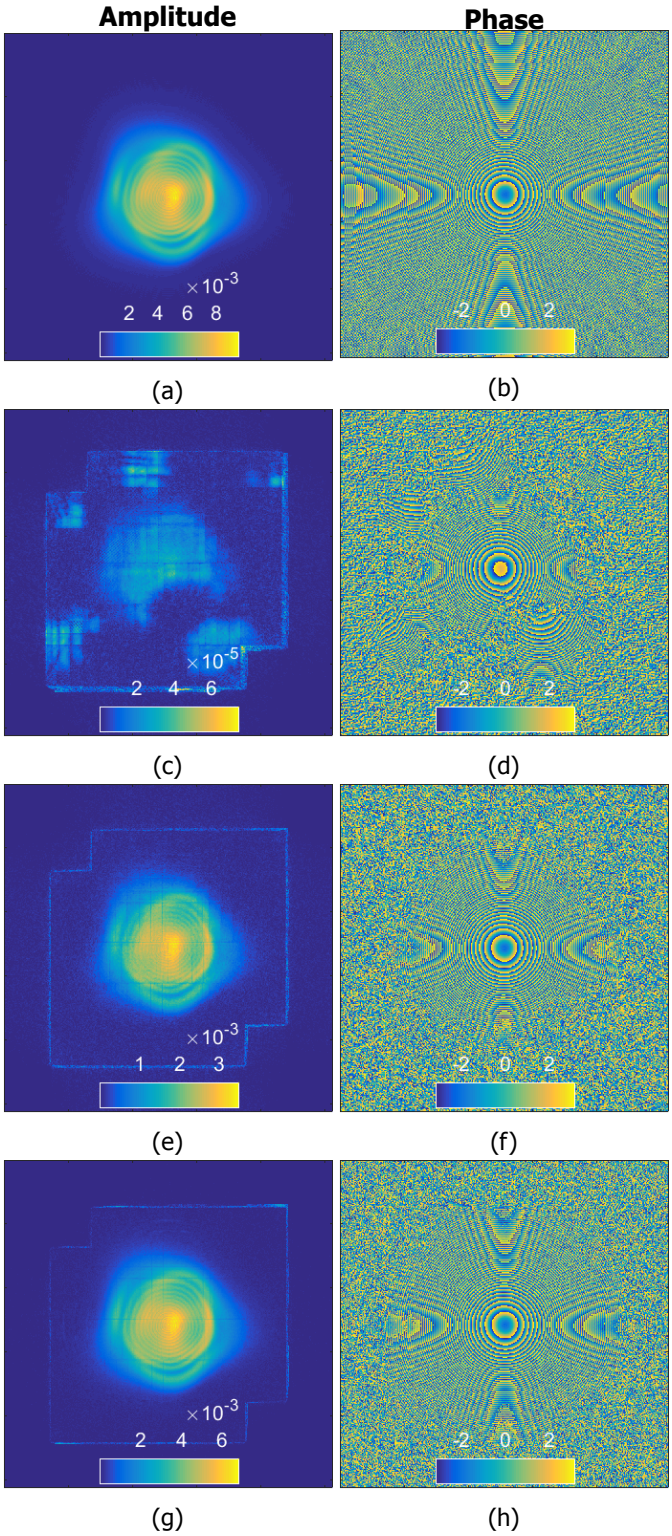

Figure 5.8: Reconstructed wavefront with varying number of photons per diffraction pattern in the presence of mask positions error. (a)–(b) are the used wavefront amplitude and phase. (c)–(d), (e)–(f), and (g)–(h) are the reconstructed amplitude and phase with 10^5, 10^6, and 10^7 number of photons per diffraction pattern respectively.

converge to the correct solutions. Hence, from these results, one can conclude that the position correction method can tolerate mask positions error as large as 3 times of the wavelength.

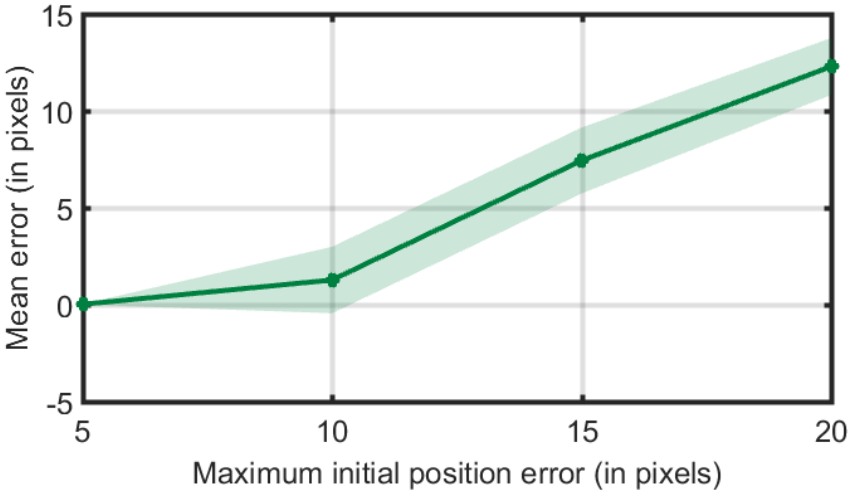

Figure 5.9: Mean error versus introduced maximum initial position error. Ten simulations were performed for each introduced maximum initial position error. Solid line represents the mean of the converged error of ten simulations; whereas the semi-transparent patch shows the standard deviation of the same.

5.4. Discussion and conclusion

We have implemented ptychography for the application of high-NA EUV wavefront sensor and shown its robustness and limitations. Ptychography was already suggested for EUV wavefront sensing in Ref. [15]. In the present work, we have shown the results with simulated EUV wavefront and have analyzed the reconstructions in presence of mask positions error as well as Poisson noise.

Using simulated data, we have shown that even a mask position error of 39 nm can be corrected with an accuracy of 10^{-6} pixels (~7.81 fm). The error in the reconstructed wavefront has been shown in term of Zernike coefficients. 20 pm ($\sim 0.0015\lambda$) of error in Zernike coefficient has been achieved for wavefront reconstruction. Furthermore, on performing the simulations in presence of noise as well as mask positions error, we have found that it can bear Poisson noise of 10^6 number of photons per diffraction pattern in the presence of the mask positions error from [-5,5] pixels (~[-39.05,39.05] nm). Additionally, we have also shown the results for the tolerance of initial mask positions error. These results can stand as a first step for the implementation of ptychography to EUV wavefront sensing applications.

References

[1] P. Dwivedi, S. F. Pereira, and H. P. Urbach. Ptychography as a wavefront sensor for high-numerical aperture extreme ultraviolet lithography: analysis and limitations. *Optical Engineering*, 58(4), 2019.

[2] B. Wu and A. Kumar. Extreme ultraviolet lithography: A review. *Journal of Vacuum Science and Technology B: Microelectronics and Nanometer Structures*, 2007.

[3] V. Bakshi, editor. *EUV Lithography*. SPIE Press, second edition, 2018.

[4] V. Bakshi, editor. *EUV Lithography*. SPIE Press, 2009.

[5] W. P. Linnik. A simple interferometer for the investigation of optical systems. *Proceedings of the Academy of Sciences of the USSR*, 1(208), 1933.

[6] R. N. Smartt and W. H. Steel. Theory and application of point-diffraction interferometers (telescope testing). *Japanese Journal of Applied Physics*, 14:351–356, 1975.

[7] K. A. Goldberg, H. R. Beguiristain, J. Bokor, H. Medecki, K. H. Jackson, D. T. Attwood, G. E. Sommargren, J. P. Spallas, and R. E. Hostetler. At-wavelength testing of optics for EUV. *SPIE Proceeding*, 2437:347–354, 1995.

[8] H. Medecki, E. Tejnil, K. A. Goldberg, and J. Bokor. Phase-shifting point diffraction interferometer. *Optics Letters*, 21(19):1526–1528, 1996.

[9] E. Tejnil, K. A. Goldberg, S. H. Lee, H. Medecki, P. J. Batson, and P. E. Denham. At-wavelength interferometry for extreme ultraviolet lithography. *Journal of Vacuum Science & Technology*, 15(9):2455, 1997.

[10] K. A. Goldberg. *Extreme ultraviolet interferometry*. PhD thesis, University of California, Berkeley, 1997.

[11] H. H. Hopkins. Interferometric methods for the study of diffraction images. *Optica Acta: International Journal of Optics*, 2(1):23–29, 1955.

[12] I. Ghozeil. *Optical Shop Testing*. Wiley, 1992.

[13] A. Polo, V. Kutchoukov, F. Bociort, S. F. Pereira, and H. P. Urbach. Determination of wavefront structure for a Hartmann wavefront sensor using a phase-retrieval method. *Opt. Express*, 20:7822–7832, 2012.

[14] P. Mercère, P. Zeitoun, M. Idir, S. Le Pape, D. Douillet, X. Levecq, G. Dovillaire, S. Bucourt, K. A. Goldberg, P. P. Naulleau, and S. Rekawa. Hartmann wave-front measurement at 13.4 nm with $\frac{\lambda_{euv}}{120}$ accuracy. *Optics Letters*, 28(17):1534–1536, 2003.

[15] A. Wojdyla, R. Miyakawa, and P. Naulleau. Ptychographic wavefront sensor for high-NA EUV inspection and exposure tools. *Proceeding of SPIE*, 9048, 2014.

[16] J. M. Rodenburg, A. C. Hurst, and A. G. Cullis. Transmission microscopy without lenses for objects of unlimited size. *Ultramicroscopy*, 107(2-3):227–231, 2007.

[17] A. M. Maiden, J. M. Rodenburg, and M. J. Humphry. Optical ptychography: A practical implementation with useful resolution. *Optics Letters*, 35(15):2585–2587, 2010.

[18] J. M. Rodenburg, A. C. Hurst, A. G. Cullis, B. R. Dobson, F. Pfeiffer, O. Bunk, C. David, K. Jefimovs, and I. Johnson. Hard-x-ray lensless imaging of extended objects. *Physical Review Letters*, 98(3), 2007.

[19] P. Thibault, M. Dierolf, A. Menzel, O. Bunk, C. David, and F. Pfeiffer. High-resolution scanning x-ray diffraction microscopy. *Science*, 321(5887):379–382, 2008.

[20] F. Hüe, J. M. Rodenburg, A. M. Maiden, F. Sweeney, and P. A. Midgley. Wavefront phase retrieval in transmission electron microscopy via ptychography. *Physical Review B - Condensed Matter and Materials Physics*, 82(12), 2010.

[21] J. M. Humphry, B. Kraus, A. C. Hurst, A. M. Maiden, and J. M. Rodenburg. Ptychographic electron microscopy using high-angle dark-field scattering for sub-nanometre resolution imaging. *Nature Communications*, 3, 2012.

[22] P. Helfenstein, I. Mochi, R. Rajeev, S. Fernandez, and Y. Ekinci. Coherent diffractive imaging methods for semiconductor manufacturing. *Advanced Optical Technologies*, 6(6):439–448, 2017.

[23] H. M. L. Faulkner and J. M. Rodenburg. Movable aperture lensless transmission microscopy: A novel phase retrieval algorithm. *Physical Review Letters*, 93(2):023903–1, 2004.

[24] F. Zhang, I. Peterson, J. Vila-Comamala, A. Diaz, F. Berenguer, R. Bean, B. Chen, A. Menzel, I. K. Robinson, and J. M. Rodenburg. Translation position determination in ptychographic coherent diffraction imaging. *Opt. Express*, 21:13592–13606, 2013.

[25] P. Dwivedi, A. P. Konijnenberg, S. F. Pereira, and H. P. Urbach. Lateral position correction in ptychography using the gradient of intensity patterns. *Ultramicroscopy*, 192:29–36, 2018.

6

Application II: ptychography applied to coherent Fourier scatterometry

We have demonstrated that the extended ptychographical iterative engine (ePIE) algorithm can be applied to retrieve the phase information of the vectorial scattered field of a subwavelength object, with as input the amplitude of the scattered field. We applied this technique combined with coherent Fourier scatterometry to determine the phase of the scattered field of a subwavelength grating, illuminated by a focused field.

Part of this chapter is published in OSA Continuum, **2**(5), 1590–1599 (2019) [1]

Conventional imaging methods are usually able to measure the intensity of the image, and the phase information is lost. However, at the same time, it is well known that phase information is useful to reveal certain features of the object and improve the contrast of the images. Means of solving this problem have been proposed and applied such as interferometry, quantitative phase contrast, holography. However, with the fast development of computing power, computational imaging methods have emerged. The combination of computational algorithms with a not-so-sophisticated optical system can retrieve the object information, e.g. phase of the object, 3D information, which is not possible with conventional imaging methods. Lensless imaging—a type of computational imaging—replaces lenses with algorithms. Several lensless imaging techniques were explored in the last five decades, showing that it is possible to retrieve the complex-valued field using only amplitude information [2–4]. Among these algorithms, ptychography is successful in terms of robustness to noise and convergence to correct solution. It has been widely used for visible wavelengths, x-rays as well as e-beams [5–10].

In this chapter, we apply ptychography to determine the amplitude and phase of the scattered field by a subwavelength object. The scattered field has been obtained using a relatively new technique called Coherent Fourier Scatterometry (CFS).[11] In this technique, the object is illuminated by a focused field, and the intensity of the scattered field at all angles within the numerical aperture of the collection lens is acquired in one shot using a CCD camera. With the information on the scattered field combined with a priori information about the object, it is possible to recover certain features of the object with subwavelength accuracy. CFS has been applied to reconstruct several parameters of gratings printed on wafers such as period, critical dimension, height and sidewall angles.[12] It has also been shown in Ref. [13] that with the knowledge of not only the amplitude but also the phase of the scattered field, a gain in sensitivity in the grating parameter retrieval can be achieved. The latter becomes essential in specific applications such as in the semiconductor industry where the determination of accurate gratings parameters with small error margin is wished.

The chapter is organized as follows: In Section 6.1 we explain about the used techniques to obtain ptychographic data and the used parameters to perform the experiment.In Section 6.2, we discuss the reconstructed scattered field and the mask. Finally, we present in the last Section 6.3 our conclusions and outlook.

6.1. Method

The scattered field that we will be reconstructing using ePIE [14] is shown in Fig. 6.1. Here, the red square is the part of the object which is scanned by the mask. The mask function is a check-board type amplitude mask with five square titles: one in the center and four around it (see Fig. 6.2). The reason for this choice relies on obtaining a diversified intensity pattern in the Fourier plane. The mask was fabricated using a 3D printer, and each title is a square with a dimension of 400× 400 μm^2.

The wavelength of the used light was $\lambda = 632.8$ nm, and the focal length of the Fourier lens was $f = 20$ cm. In ptychography, the object is scanned by a mask, and

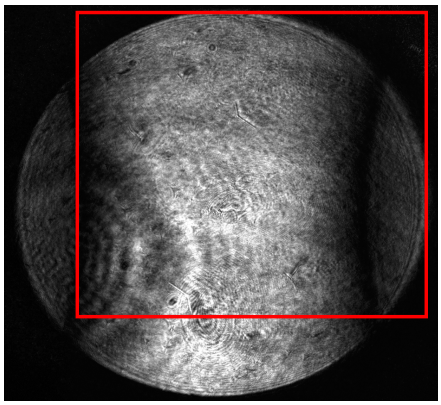

Figure 6.1: Experimental scattered field intensity of the grating. Red square is the part scanned by the mask.

corresponding intensity patterns are measured in the far-field. Here, we shifted our mask to 12×12 mask positions in a way that the overlap between the neighboring mask positions was 79%.

To obtain clean ptychographic data, we performed a few important steps on the captured intensities. Note that, these steps are performed for each mask positions.

- First, we measured 30 intensity patterns and averaged it. This gave us the correct estimation of the noise. Let us call this intensity pattern as I_{meas}.
- To measure the background noise, we took 30 intensity measurements in complete dark and average it. Let us call this intensity patterns as I_{dark}.
- Perform $I_{\text{meas}} - I_{\text{dark}}$.
- To increase the dynamic range, we measured five intensity patterns for five gradually increasing exposure times and increased the dynamic range.

In the end, we had clean ptychographic data with higher dynamic range that was used to reconstruct the object using ePIE.

6.2. Results

We present here the results in two parts: the first result shows the reconstruction of the mask. The second result is the reconstruction of the scattered field of the grating with the optimal parameters. The convergence of the reconstruction was achieved within 15 iterations of the simulation; therefore, we have performed the analysis with 30 iterations.

6.2.1. Probe reconstruction

We also present here, briefly, that the extended Ptychographic Iterative Engine (ePIE) works as it is also able to reconstruct the mask that we used in the ex-

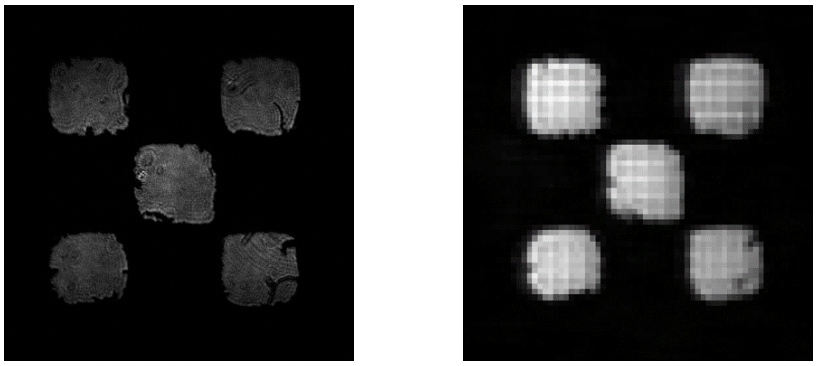

(a) (b)

Figure 6.2: (a) The 5 tiles mask that we used experimentally. (b) The reconstructed probe by using the ePIE algorithm with 30 iterations and 79% overlap.

perimental setup. It can be seen from Figure 6.2a that the mask had some imperfections because the edges were not sharp and it had some scratches. As the reconstructions were performed, we observed that those imperfections and the shape of each tile were also retrieved accurately. Thus, it perfectly served for the calibration of the ePIE algorithm.

6.2.2. Reconstruction of the scattered field of a diffraction grating

In this subsection, we show the reconstruction of the scattered field of a subwavelength diffraction grating illuminated in a TM mode. The results are shown in Fig. 6.3. The reconstruction of the scattered field amplitude has been successful, as it is close to the expected amplitude as shown in Fig. 6.1. Note that, even the detailed features such as the diffraction rings due to dust in the grating were also reconstructed. Furthermore, the reconstructed phase agrees with the expected theoretical results (see bottom figures of Figs. 4 and 5 in Ref. [15]). The artifacts outside the pupil area (at the upper right and lower right corners of the Fig. 6.3) occurs because the intensity outside the pupil is zero; therefore the phase is random in this area. The mean square error (MSE) is shown in Fig. 6.4. The MSE is computed for the complete scanned area of the scattered field which also includes the area outside the pupil area. Consequently, the MSE is higher than if the MSE was computed only for the pupil area. We also would like to point out that there is a clear discontinuity in the phase at the right side of the reconstructed scattered field as expected, showing that the method works even for large phase discontinuities.

6.3. Conclusions

In this work, we have shown the successful implementation of ePIE—a phase retrieval technique—to reconstruct the scattered field of a sub-wavelength grating. As expected, within ten iterations of this method, we found the correct solution. This

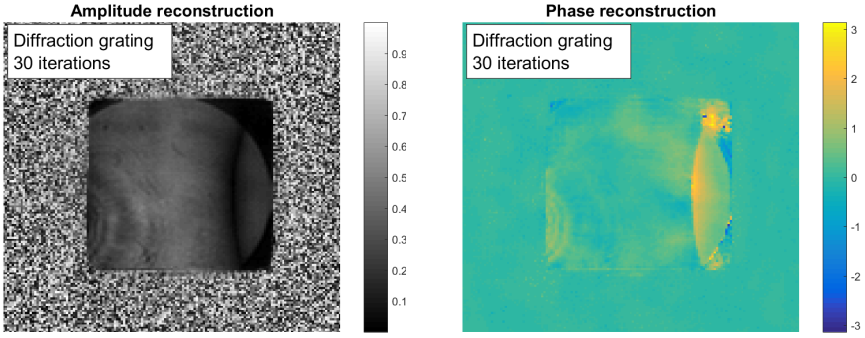

(a) (b)

Figure 6.3: Phase and amplitude retrieval of the scattered field of a grating illuminated in a TM mode by a focused laser beam.

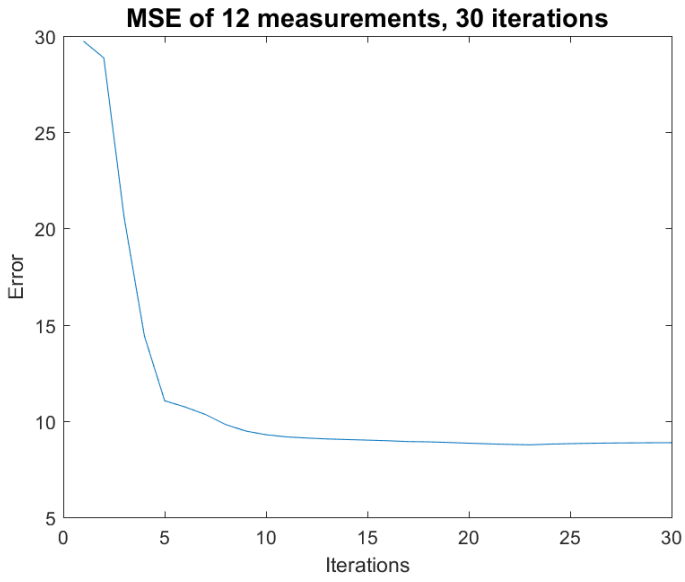

Figure 6.4: MSE of the retrieval of the grating.

iterative method can replace the interferometer which is a cumbersome method to use, whereas the iterative method can be easily adapted to a scatterometry setup. Although the intended application for this work is an optical inspection in lithography, we foresee that it can also be used for characterization of nanostructures with high accuracy, inspection of surfaces and printed structures for defects.

Acknowledgments

We thank Matthias Strauch for his help, which was crucial for the accomplishment of this work. We also thank Thim Zuidwijk and Mauricio Larodé Díaz for designing, fabricating and testing the mask and R.C. Horsten for technical assistance. We also thank Europhotonics coordinators Dr. H. Giovannini, Dr. J. Natoli and Ms. N. Guillem.

References

[1] P. Dwivedi, J. E. H. Cardoso Sakamoto, and S. F. Pereira. Phase retrieval applied to coherent fourier scatterometry using the extended ptychographic iterative engine. *OSA Continuum*, 2(5):1590–1599, 2019.

[2] R. W. Gerchberg. A practical algorithm for the determination of phase from image and diffraction plane pictures. *Optik*, 35:237–246, 1972.

[3] J. R. Fienup. Reconstruction of an object from the modulus of its fourier transform. *Opt. Lett.*, 3:27–29, 1978.

[4] H. M. L. Faulkner and J. M. Rodenburg. Movable aperture lensless transmission microscopy: a novel phase retrieval algorithm. *Physical review letters*, 93(2):023903, 2004.

[5] A. M. Maiden, J. M. Rodenburg, and M. J. Humphry. Optical ptychography: a practical implementation with useful resolution. *Opt. Lett.*, 35:2585–2587, 2010.

[6] G. R. Brady, M. Guizar-Sicairos, and J. R. Fienup. Optical wavefront measurement using phase retrieval with transverse translation diversity. *Optics Express*, 17(2):624–639, 2009.

[7] J. M. Rodenburg, A. C. Hurst, A. G. Cullis, B. R. Dobson, F. Pfeiffer, O. Bunk, C. David, K. Jefimovs, and I. Johnson. Hard-x-ray lensless imaging of extended objects. *Phys. Rev. Lett.*, 98:034801, 2007.

[8] M. Dierolf, A. T. P. Menzel, P. Schneider, C. M. Kewish, R. Wepf, O. Bunk, and F. Pfeiffer. Ptychographic x-ray computed tomography at the nanoscale. *Nature*, 467:436–439, 2010.

[9] F. Hüe, J. M. Rodenburg, A. M. Maiden, F. Sweeney, and P. A. Midgley. Wavefront phase retrieval in transmission electron microscopy via ptychography. *Phys. Rev. B*, 82:12–15, 2010.

[10] P. Wang, F. Zhang, S. Gao, M. Zhang, and A. I. Kirkland. Electron ptychographic diffractive imaging of boron atoms in LaB_6 crystals. *Scientific Reports*, 7(2857), 2017.

[11] O. El Gawhary, N. Kumar, S. F. Pereira, W. M. J. Coene, and H. P. Urbach. Performance analysis of coherent fourier scatterometry. *Aplied Physics B*, 105:775–781, 2011.

[12] N. Kumar, P. Petrik, G. K. P. Ramanandan, O. El Gwhary, S. F. Pereira, W. M. J. Coene, and H. P. Urbaach. Reconstruction of sub-wavelength features and nano-positioning of gratings using coherent fourier scatterometry. *Optics Express*, 22:24678–24688, 2014.

[13] S. Roy, N. Kumar, S. F. Pereira, and H. P. Urbach. Interferometric coherent fourier scatterometry: a method for obtaining high sensitivity in the optical inverse-grating problem. *Journal of Optics*, 15:705707, 2013.

[14] A. M. Maiden and J. M. Rodenburg. An improved ptychographical phase retrieval algorithm for diffractive imaging. *Ultramicroscopy*, 109(10):1256 – 1262, 2009.

[15] N. Kumar, L. Cisotto, S. Roy, G. K. P. Ramanandan, S. F. Pereira, and H. P. Urbaach. Determination of the full scattering matrix using coherent fourier scatterometry. *Applied Optics*, 55:4408–4413, 2016.

7

Conclusion and outlook

7.1. Conclusion

We recall the research question posed at the beginning of the thesis: how to correct probe positions in ptychography efficiently? In order to solve this problem, we have proposed two novel methods in this thesis: probe position correction using the gradient of intensity pattern and probe position correction using HIO and cross-correlation.

The intensity gradient method, as the name suggests, is based on the gradient of the simulated intensity pattern. We have found some advantages over the existing methods. To begin with, it is a straightforward extension of ePIE. It is less computationally expensive than the cross-correlation method while achieving comparable accuracy. This method can correct probe positions with sub-pixel accuracy whereas, in the cross-correlation method, an additional matrix multiplication method is used to achieve this high accuracy. A comparison between the intensity gradient method and the cross-correlation method has been shown in this thesis. We have implemented this method with simulations and experimental data using visible light. The method can be used for e-beam or x-ray ptychography where an error of 50 pm can lead to a degraded reconstruction of the object. For visible light, it can relax some requirements of the stability of the experimental setup.

The second proposed method is based on hybrid input-output (HIO) and cross-correlation methods. HIO and cross-correlation are well-known methods to retrieve an object and find the shift between two identical images, respectively. Here, we have implemented these methods in a way that it can correct the probe positions in ptychography. However, this method has a limitation on the used probe function that it should be strictly zero outside the defined area. Therefore, it can not be used for all applications where ptychography can be used. We anticipate that this method can be applied for the case when a hard mask scans a wavefront. This method can correct probe positions with integer pixel accuracy. To achieve sub-pixel accuracy, we suggest to use matrix multiplication method [1] as used in the

cross-correlation method. Another important observation is that the results with less number of probe positions are better than for a large number of probe positions. Furthermore, a comparison between this method and the intensity gradient method is also carried out.

Later on, we have implemented ptychography in two applications where ptychography is hardly explored: ptychography for coherent Fourier scatterometry and ptychography as a wavefront sensor for high-NA EUV Lithography.

In Chapter 5, we have successfully demonstrated an efficient application of ptychography to characterize high-NA EUV lithography imaging systems. This work is an essential step in the development of next-generation EUV exposure systems for the continuous marching of Moore's law. The reconstructions are shown using simulated data which resembles the expected EUV lithography experiment. Furthermore, we have shown the reconstruction even in the presence of inaccurate mask position errors. These results can be used as a first step towards the implementation of this method in real experimental data.

In Chapter 6, ptychography is applied for Coherent Fourier scatterometry. Coherent Fourier scatterometry is a new technique to retrieve grating parameters. Previously, it has been found out that the phase information of the scattered field enhances the retrieved parameter [2]. Therefore, here we showed the successful implementation of ePIE to retrieve the phase of the scattered field and proposed ptychography an alternative method to interferometry.

7.2. Outlook

Fourier ptychography (FP) is a technique to retrieve high-resolution image using several low-resolution images which correspond to different Fourier space. The Fourier ptychography setup is similar to a microscope setup except that an array of LEDs replaces the light source. In this way, LEDs are switched on sequentially, and corresponding low-resolution images are captured in the camera. As the position of the switched on LED changes, the Fourier transform of the captured image translates in the Fourier space.

Unlike conventional ptychography, FP does not have any moving or scanning parts in the setup. Therefore, one would assume that this technique would not suffer from positioning accuracy as is the case with conventional ptychography. However, FP suffers from an incorrect position of LEDs as well as the global shift of LEDs, i.e. the shift of the entire LED array. In Fig. 7.1, green circle corresponds to the Fourier space of a correctly positioned LED and purple circle corresponds to the Fourier space of an incorrectly positioned LED which can be caused by a global shift as well. This small shift, in this case, has led to exclude zero frequency from Fourier space. Therefore, an expected bright field image becomes a dark field image.

Hence, few attempts have been made to solve this problem. Some of the proposed methods are inspired by positions correction in conventional ptychography. For example, the state-of-the-art method proposed in Ref. [3] uses simulated annealing method as used in conventional ptychography [4]. This technique is computationally exhaustive. Therefore, instead of correcting all LED positions independently, A. Zhou et. al assume that all LEDs positions are dependent on each other

[5]. Therefore, instead of performing optimization for each LED position, optimization was performed for each iteration when all LEDs were used. This approach has substantially reduced the computational cost. Furthermore, Ref. [6] uses cross-correlation between consecutive updates in Fourier space.

Since the intensity gradient method has been proved to have substantial advantages over other existing methods in real space ptycohgraphy, we propose to exploit its advantage for Fourier ptychography as well. Moreover, an analysis for its applicability, accuracy and computational expensiveness should be studied.

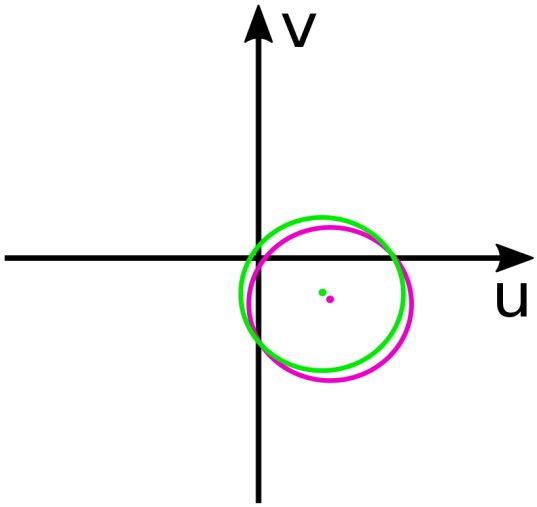

Figure 7.1: Fourier space corresponding to correct (green) and shifted (purple) LED positions are shown. Note that, the Fourier space corresponding to correct LED position has zero frequency while the one corresponding to the shifted LED position does not. This small shift can cause a degraded object reconstruction.

References

[1] S. T. Thurman M. Guizar-Sicairos and J. R. Fienup. Efficient subpixel image registration algorithms. *Optics Letter*, 33:156–158, 2008.

[2] S. Roy, N. Kumar, S. F. Pereira, and H. P. Urbach. Interferometric coherent fourier scatterometry: a method for obtaining high sensitivity in the optical inverse-grating problem. *Journal of Optics*, 15:705707, 2013.

[3] J. Sun, Q. Chen, Y. Zhang, and C. Zuo. Efficient positional misalignment correction method for fourier ptychograhic microscopy correction method for fourier ptychographic microscopy. *Biomedical optics express*, 2016.

[4] A. M. Maiden, M. J. Humphry, M. C. Sarahan, B. Kraus, and J. M. Rodenburg. An annealing algorithm to correct positioning errors in ptychography. *Ultramicroscopy*, 120:64–72, 2012.

[5] A. Zhou, W. Wang, N. Chen, E. Y. Lam, B. Lee, and G. Situ. Fast and robust misalignment correction of fourier ptychographic microscopy for full field of view reconstruction. *Optics Express*, 2018.

[6] S. Chen, T. Xu, J. Zhang, X. Wang, and Y. Zhang. Random positional deviations correction for each led via epie in fourier ptychographic microscopy led via epie in fourier ptychographic microscopy. *IEEE*, 2018.

Acknowledgements

The myth of finishing PhD starts with writing thesis. That has also come to an end with this chapter. Even though, the name on the title page is mine, many people have contributed to this work in one or another way. Here, I would like to express my gratitude to those.

First of all, I thank the promotor prof.dr. Paul Urbach for his critical inputs and reviews on my work. I express my heartiest gratitude to the promotor dr.ir. Silvania Pereira for her trust and continuous support during my PhD. Your constant encouragement and co-operation in different projects helped me become an independent researcher. I thank Peter Somers and Sander Konijnenberg for their open-door attitude and translating the summary and propositions to Dutch respectively. I also thank Wouter Erades for making the first draft Dutch translation of the summary.

Moreover, I thank all committee members for their crucial and thoughtful comments on my thesis.

I am deeply grateful to dr. Jeff Meisner for his input in time when I almost gave up on the new technique. It is my immense pleasure to work in the group with Joseph Braat. Thank you for sharing the invaluable stories during the coffee breaks. I thank Roland for being a partial office mate. I am grateful to Yvonne van Aalst for making my life easier when it comes to dealing with administrative things and practical issues. I also extend my thanks to Nandini Bhattacharya, Thim Zuidwijk, Gleb Vdovin, Rob Pols, Aurele Adam, and Florian Bociort.

I thank all my PhD comrades! To begin with, Sander Konijnenberg, I sincerely thank you for the fruitful discussions and collaborations in the initial phase of my PhD. Fellipe, you gave us cheerful moments, especially, when you talked to the coffee machine. Unfortunately, it was difficult to overhear your conversation but we enjoyed it anyway. I thank Matthias for helping me in every possible manner and sharing many moments together: sailing, baking, biking, digging holes at the beach (yes, now I know why Germans do this) and many more. I thank dr. Sarathi Roy for being a jolly officemate. By the way, you would not get your 10 Euros back! *Wait a minute*, I am talking about you Dmytro. You gave me the much needed distraction by entertaining us from your dark humor and jokes. I am fortunate enough to be part of ADOPSYS group. Exploring different cities in the different parts of the world was an enriching and adventurous experience with all of you. Special thanks to Marco Mout for helping me socialize during my secondment at the most happening place of Germany—Aalen. During my secondment, I met several people and two are worth mentioning here: Deepa and Vera. I hope to continue our get together every year.

The list does not stop here. Thanks to Hamed Ahmadpanahi, Zheng Xi, Andreas Hänsel, Nishant Kumar, Ying Tang, Zhe Hou, Xiujie Dou, Yifeng Shao, Luca Cisotto and others that I have spent time during coffee breaks, lunch, optica social events,

and dinners. Thank you guys for making the environment lively. In the end, everyone contributed in some or other ways. Here is my attempt to thank all: Masha Nemati, Po-Ju, Peiwen Meng, Xukang Wei, Lauryna Šiaudinyte, Ruben Biesheuvel, Zhongwen Deng, Yuxin Wang, Paolo Ansuinelli, Anna Ezerskaia, Min Jiang, Zheng Zhu, Kafei Hei, Iman Esmaeil Zadeh, etc. I also extend my thanks to Tope, Franklin, and Alex who were involved at the end phase of my PhD.

Mauricio and Hiroki, you did a good job and helped me writing the last chapter of my thesis. Good luck with everything.

Outside of university, I have met many people; some of them have left footprints on my PhD life. To begin with, my sincere thanks to Jessica Alecci for bearing me at home. My free time was defined by you, Geetha. You are my crime partner in every other party and activity. Asha Downes, you introduced me with Soca music and dance. Lucy, you introduced me to the wild nightlife of Rotterdam. Shubhangi, Tanya for making the apartment a home. Poonam Singhal and Komal Pandey, we have kept in touch with each other since college and shared cheerful moments together. Let us keep it the way it is.

I thank my parents for their unconditional love. You have always inspired and gave me strength. This thesis is affectionately dedicated to my parents. Once again thank you very much for giving me the wings to fly. I extend my deep gratitude and love to my siblings and naughty cousins: Aparna, Dushyant, Divya, and Kaustubh. Special thanks to Dushyant for taking the time out and designing the thesis cover. I welcome my adorable niece and nephew to the world. Lots of love and kisses from my side. Avinash, your immense contribution and support is ineffable. I always look for you to find myself. Anamika, you were always there for me without any exception. My humbled thanks to you for being there when I most needed you.

Last but not least, I thank the coffee-guy who made sure to have enough green teas in the coffee-room. He even went a step beyond by keeping the green tea packs on my desk. I also thank the NS trains as a part of my thesis is written in the train. Many thanks to the self-sacrifice of trees for the printing of this thesis.

I rest my case here.

Curriculum Vitæ

15-10-1990 Born in Kanpur, India.

Education

2008–2013 Integrated Master in Applied Physics
Indian Institute of Technology (ISM), Dhanbad, India

2013–2014 Research assistant
Max Planck institute for the Physics of complex systems, Dresden, Germany

2014– PhD student
Optics group, Delft University of Technology, The Netherlands
Thesis: Position Correction in Ptychography and Its Application
Promotors: Prof.dr. H.P. Urbach and dr.ir. S.F. Pereira

2019–Present Design Engineer, ASML, Veldhoven, The Netherlands.

Scholarship and awards

2008–2013 Kishore Vaigyanik Protsahan Yojana (KVPY) scholarship

2010 ISM-merit free ship scholarship

2014–2017 Marie Curie fellowship

2017 Delft Health Initiative

List of Publications

Journal papers:

6. **P. Dwivedi**, J. E. H. Cardoso Sakamoto, and S. F. Pereira, *Phase retrieval applied to coherent Fourier scatterometry using the extended ptychographic iterative engine*, OSA Continuum, **2**(5), 1590–1599 (2019).

5. **P. Dwivedi**, S. F. Pereira, and H. P. Urbach, *Ptychography as a wavefront sensor for high-NA EUV lithography: analysis and limitations*, Optical Engineering, **58**(4), 043102 (2019).

4. **P. Dwivedi**, A. P. Konijnenberg, S. F. Pereira, J. Meisner, and H. P. Urbach, *Position correction in ptychography using hybrid input-output (HIO) and cross-correlation*, Journal of optics **21**, 035604 (2019).

3. **P. Dwivedi**, A. P. Konijnenberg, S. F. Pereira, and H. P. Urbach, *Lateral position correction in ptychography using the gradient of intensity patterns*, Ultramicroscopy **192**, 29-36 (2018).

2. **P. Dwivedi**, A. P. Konijnenberg, S. F. Pereira, and H. P. Urbach, *An alternative method to correct translation positions in ptychography*, Proceedings of SPIE **10677**, (2018).

1. **P. Dwivedi**, A. P. Konijnenberg, S. F. Pereira, and H. P. Urbach, *New method for probe position correction for Ptychography*, Proceedings of SPIE **10329**, (2017).